Studies of Multi-Functional Printed and Dielectric Resonator Antennas using Split Ring Resonators and Metallic Structures

A thesis submitted
in partial fulfillment for the degree of

Doctor of Philosophy

by

SHAIK LATHEEF AHMED

Department of Avionics
INDIAN INSTITUTE OF SPACE SCIENCE AND TECHNOLOGY
Thiruvananthapuram - 695547

May 2018

CERTIFICATE

This is to certify that the thesis titled **Studies of Multi-Functional Printed and Dielectric Resonator Antennas using Split Ring Resonators and Metallic Structures**, submitted by **Shaik Latheef Ahmed**, to the Indian Institute of Space Science and Technology, Thiruvananthapuram, for the award of the degree of **Doctor of Philosophy**, is a bonafide record of the research work done by him under my supervision. The contents of this thesis, in full or in parts, have not been submitted to any other Institute or University for the award of any degree or diploma.

Dr. Chinmoy Saha
Assoc. Professor
Department of Avionics

Prof. B.S. Manoj
Head of the Department
Department of Avionics

Place: Thiruvananthapuram
May 2018

DECLARATION

I declare that this thesis titled **Studies of Multi-Functional Printed and Dielectric Resonator Antennas using Split Ring Resonators and Metallic Structures** submitted in fulfilment of the Degree of Doctor of Philosophy is a record of original work carried out by me under the supervision of **Dr. Chinmoy Saha**, and has not formed the basis for the award of any degree, diploma, associateship, fellowship or other titles in this or any other Institution or University of higher learning. In keeping with the ethical practice in reporting scientific information, due acknowledgements have been made wherever the findings of others have been cited.

Shaik Latheef Ahmed
Research Scholar
Department of Avionics
Roll No.: SC14D014

Place: Thiruvananthapuram
May 2018

ACKNOWLEDGEMENTS

An adequate acknowledgement is difficult to write at this point. There are many persons, without whom the present would not have been possible.

Firstly, I express my sincere gratitude towards my research supervisor Dr. Chinmoy Saha for his guidance, continuous support and encouragements during entire PhD work. I am eternally indebted to Dr. Jawad Y. Siddiqui, Assoc. Prof., University of Calcutta for fruitful advice and discussions concerning my work and for proof-reading the manuscripts.

I take this opportunity to thank my doctoral committee members - Prof. Animesh Biswas, Dr. T.J. Apren, Dr. Deepak Mishra and Dr. S. Murugesh for their regular and valuable comments and suggestions, and for steering the PhD thesis along the proper path. I would like to express my gratitude towards Prof. Yahia M.M. Antar, Royal Military College of Canada, Canada and Dr. Ashwin K. Iyer, Assoc. Prof., University of Alberta, Canada for making their labs available for measurements and characterization of few of my antenna prototypes. I express my gratitude towards Shri. Rajesh Muntha, and Shri. Shivam Arora for the great collaborations and fruitful discussions.

I am highly grateful to Dr. Rahul Waghmare, Dr. C. K. Muthukumaran, Dr. Mathiazhagan, Shri. Sabu M, Shri. Suresh Kumar, Shri. Sachin PC, Shri. Sujith Kanapala, and Shri. Vinod Kumar who in their own way made my PhD experience joyful and easy going.

I would like to thank my parents for their support.

Shaik Latheef Ahmed

ABSTRACT

Designing compact antennas and microwave circuit components has always been an important issue because of the tremendous growth in electronic communication systems. This growing demand of wireless communications and introduction of new communication protocols stipulate the re-design of wireless systems to cater different recent needs. Allocation of ultra-wideband (UWB) spectrum by FCC in 2002 attracted the antenna community to design compatible antenna systems covering the UWB band ranging from 3.1-10.6 GHz. Numerous radiating structures have been investigated utilizing radiating elements of different shapes, including circles, ellipses and squares. Complexity of designing such UWB antennas has increased many folds in recent years due to co-existence of various narrowband services within the UWB spectrum, like, WiMAX (3.3 3.7 GHz), WLAN (5.15 5.85 GHz) and X-band satellite downlink (7.25 7.75 GHz) which demand the mitigation of these interfering narrow bands for efficient communication using the UWB spectrum. Such antennas, requires in-built frequency notching feature and are known as frequency-notched UWB antenna. Introduction of recent communication protocols like software defined radio (SDR) and cognitive radio (CR) for an efficient spectrum allocation has escalated the antenna design challenges further. Antennas for this system requires special attention as it necessities an UWB and narrow band antennas in common platform. The first antenna performs spectrum sensing of unused carrier frequencies and is called sensing antenna. On the other hand, the second antenna needs to be reconfigurable one, operating over a limited bandwidth and is known as communicating antenna or "transmit/receive antenna". Present PhD thesis deals with the design, development and practical realization of multi-functional planar compact antennas for modern wireless applications. The work is systematically planned and realized as follows:

1. Metamaterial based structures (SRR and/or shunt wires) have been successfully designed and developed for realization of notched filter. Multiple rotational SRR loaded coplanar waveguide (CPW) line based frequency notched

filter is realized with an aim of using them for printed antennas for modern wireless applications.

2. The recent requirement of frequency-notched antenna design is demonstrated using planar antennas of various shapes and configuration, like, monopoles, tapered slot antennas. Seamless applications of the planar filters realized in previous section, is very efficiently used in design of such frequency notched antennas.

3. A significant contribution of the present thesis is successful realization of multi-functional antennas aimed for CR and SDR applications. This new multi-functional antenna uses a single radiating element coupled with meta-material based structures (SRRs) and/or switches around its ground plane. Combinatorial loading of the SRRs and/or the switches in this antenna provides multiple antenna functionalities. The notch frequency and narrowband frequency in this antenna can be controlled by changing the physical dimensions of Split Ring Resonator (SRR) and are independent of the antenna configuration. Various experimental aspects involving challenges and concerns in characterizing these types of antennas have also been thoroughly considered in this work.

4. A practical realization of the proposed multi-functional antennas using commercial RF switches (PIN diodes) is another significant contribution in this thesis. The realized antenna is characterized for impedance and radiation pattern measurements and provides good correspondence with theoretical estimations and simulation results. Moreover, frequency tunablity of the antenna is demonstrated using a stepper motor based rotational mechanism using rack-pinion structures.

5. A bandwidth controllable cylindrical ring dielectric resonator (CRDR) antenna is proposed. The bandwidth controllability is achieved by structurally loading the CRDR antenna with metallic cap and sleeve loading. Bandwidth controllability is demonstrated without perturbing the antenna radiation characteristics.

TABLE OF CONTENTS

LIST OF TABLES

LIST OF FIGURES

ABBREVIATIONS

ARMA	Annular Ring Monopole Antenna
CMPA	Circular Monopole Antenna
CPW	Coplanar Waveguide
CR	Cognitive Radio
CRDR	Cylindrical Ring Dielectric Resonator
DR	Dielectric Resonator
MIMO	Multiple-Input-Multiple-Output
MSR	Multi-Standard Radio
SDR	Software-Defined Radio
SRR	Split Ring Resonator
TSA	Tapered Slot Antenna
UWB	Ultra-Wideband

CHAPTER 1

Introduction

1.1 Reconfigurable and Multi-Functional Antenna: An Overview

Introduction of new technologies like UWB (Ultra-Wideband) radios, MIMO (Multiple Input Multiple Output) and MSR (Multi-Standard Radio) in modern wireless communications in the recent past have demanded design and realization of compatible antenna systems for each of these services and enhanced the antenna design challenges to a great extent[Force (2002); Alexiou and Haardt (2004); Hall et al. (2012); Christodoulou et al. (2012); Tawk et al. (2016); Christodoulou (2009); Tawk et al. (2014a)]. As antennas are necessary and critical components of these systems, they need to adjust to new operating scenarios to meet the system performance. The design challenges posed by these communication systems can be catered with the help of reconfigurable antennas. Reconfigurability in antennas imply change of antenna impedance and radiation characteristics either by means of electrical, mechanical or other means [Bernhard (2007)]. The reconfigurable antennas can be classified broadly in four categories depending on the characteristic altered, they are:

1. frequency reconfigurable antennas
2. pattern reconfigurable antennas
3. polarization reconfigurable antennas
4. combination of (1), (2) and (3)

Reconfigurability is achieved by altering the surface currents or the aperture fields of the radiator. In the case of frequency reconfigurable antennas, the operating frequency of the antenna is modified by changing the electrical length or the surface current distribution. For the radiation pattern reconfigurable antennas, the radiation properties like shape of the pattern, directivity and direction of radiation are altered by changing the radiating edges, feed network of the radiator. In case of polarization reconfigurable antennas, the polarization of the antenna is modified by altering the feed network or the radiator geometry. In the last category, the antenna is configured to attain multiple reconfigurability by combination of above stated properties. Proper selection of a reconfiguration technique based on a desired type of reconfiguration, with minimal impact on the other characteristics of the antenna is the most important criteria in designing a reconfigurable antenna.

Several reconfiguration techniques has been proposed to attain the reconfigurability. Various techniques of designing the reconfigurable antenna can be mainly classified as shown in figure 1.1.

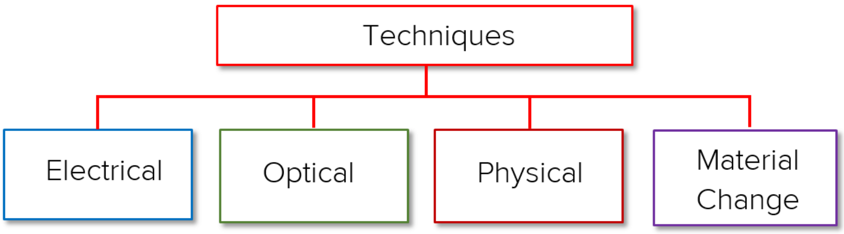

Figure 1.1: Various techniques to attain reconfigurable antennas

Electrically reconfigurable antenna achieves the reconfigurable operation by employing switches on the antenna's radiating aperture and/or feeding line. The popular choice of electrical switches are PIN diodes, varactors, RF MEMS, whose selection choice depends on various factors like cost, ease of design, switching speed, topology and so on. PIN diodes offer low loss at low cost, but are limited by their forward bias dc current in ON state which degrades the overall power efficiency and device battery life. Varactor diodes are utilized where continuous reactive tuning is required, but suffer from poor linearity. To improve the varactor linearity, ferroelectric variable capacitors are used instead, they suffer from limited tuning range and higher loss than varactors. MEMS devices offer the advantages like very low loss, wide bandwidth and low power consumption, but are often opted due to high operating voltage, low reliability and higher cost than semiconductor devices. Recently RF MEMS [Erdil et al. (2007); Huff and Bernhard (2006); won

Jung et al. (2006)], PIN diodes [Peroulis et al. (2005); Han et al. (2014); Row et al. (2012)] and varactors, [Behdad and Sarabandi (2006); White and Rebeiz (2009)] are being used as switches for achieving reconfigurable antenna functionality. While properly biased PIN diodes and RF MEMS based switches provides different antenna aperture based on ON/OFF mechanism and hence the desired antenna reconfiguration, varactor based reconfiguration utilizes variable capacitance of the varactor due to the change in the bias voltage providing a vast tuning range. Frequency tunable antenna based on CPW stub loaded MEMS capacitor is demonstrated in [Erdil et al. (2007)], where the electrical length of the stub is controlled by MEMS capacitor. In [Huff and Bernhard (2006); won Jung et al. (2006)], the MEMS switches are embedded in the arms of square spiral antenna, thereby enabling the pattern reconfigurable antenna depending on the actuation of the switches. A single-fed resonant slot loaded with a series of PIN diode switches is utilized in [Peroulis et al. (2005)] to change effective electrical length, resulting reconfigurability. By incorporating three PIN diode switches along the meandered tuning stub loaded on top of the half circular patch located within the circular slot multi-frequency operation is realised in [Han et al. (2014)]. Two PIN diodes are incorporated in the V-shaped feed of annular slot antenna to implement three different polarizations, including one linear polarization and dual orthogonal circular polarizations. Dual-band reconfigurable slot antennas is realized in [Behdad and Sarabandi (2006)] by loading a slot antenna with a varactor at a certain location along the slot. [White and Rebeiz (2009)], utilized varactors in the slot antenna to attain single-and dual-polarized slot-ring antennas.

Optical reconfigurable antenna utilizes photoconductive switches wherein the state of the switch is manipulated by laser beam. Two silicon photo switches are placed in both dipole arms to attain frequency reconfigurable antenna in [Panagamuwa et al. (2006)]. Light from two infrared laser diodes is applied to the switches to alter the functionality. Mechanical reconfigurable antennas utilizes a physical movement of antenna structure to obtain the desired functionality. The physical alteration of the structure can be realized using motors where a part of the antenna is changed. Popular mechanical reconfigurable antenna systems are parabolic reflector antennas where a single rotating reflector is used to cater multiple sources placed at vertex. In [Costantine et al. (2014)], the response of the antenna is altered by changing the position and spacing of the ground plane with respect to the antenna. Other category explored for reconfigurability is by utilizing smart materials like liquid crystals, ferrites and BST where the material properties like conductivity, permittivity and permeability are altered. [Sathi et al. (2012)], utilized organic semiconductor polymer to attain frequency sweeping capability. The resonance frequency is changed by changing the optical illusion intensity on the substrate. Liquid crystal are used in [Liu and Langley (2008)] to attain the reconfigurability. Radiation characteristics of microstrip planar array of circular patch antenna printed on Ni-Al ferrite substrate are altered by biasing the ferrite as demonstrated in [Pourush et al. (2006)].

The advantages of using reconfigurable antenna compared to multiband/wideband antennas or multiple antennas can be summarized as [Christodoulou et al. (2012)]:

- Flexible utilization of resources

    minimizes cost

    minimizes space requirement

    allows easier integration

    good isolation between different wireless standards

- Lower front-end complexity

    no need for front-end filtering

    good out-of-band rejection

- Multi-functional capabilities

    change functionality as per the requirement

    provide wideband or narrowband operation

- Suitable candidate for software defined radio (SDR) and cognitive radio (CR) applications

The antennas discussed in this thesis are termed as ‘multi-functional’ antennas as they are new class of antennas where the impedance characteristics are altered as

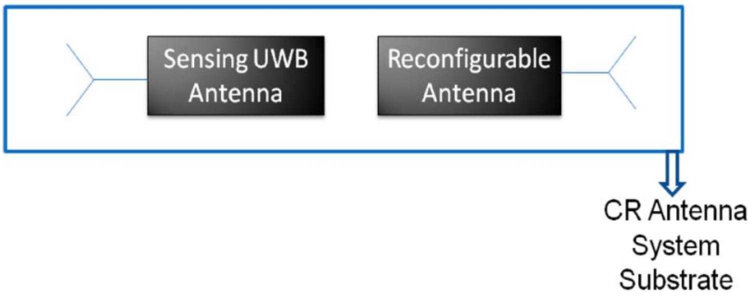

Figure 1.2: Cognitive radio antenna system [Christodoulou et al. (2012)]

opposed to the antennas discussed above where the antenna properties like frequency, polarization and pattern are altered. These antennas find their application in CR systems, as they require the antenna whose functionalities are wideband, reconfigurable narrowband and wideband with reconfigurable notch as discussed in detail in the following section.

1.2 State-of-the-art Cognitive Radio System

The advancements in wireless communication and the use of new protocols have led to imbalance in spectrum allocation. The scarcity in spectrum allocations is caused of different spectrum allocation policies and lack of available frequencies. To alleviate this problem, the spectrum has to be utilized effectively leading to new protocols like CR. Here the unused spectrum referred as ‘white spaces’ is identified dynamically and allocated to users to communicate over those white spaces. The CR process needs to monitor the spectrum, process information and utilize the white spaces and adapt for future use, commonly referring it as sense, act and learn process. The CR technology requires two set of complementary antennas, i) UWB antenna and ii) narrowband antenna, for efficient spectrum utilization. The UWB antenna, called sensing antenna, continuously scans over the ultra-wideband to search the idle spectrum not currently in use by the ‘primary user’ and allocates it to the ‘secondary user’ which immediately starts communicating at this frequency, using the narrowband antenna (communicating antenna). Thus efficient utilization of the idle spectrum dedicated to the primary user and distributing it dynamically to the secondary user, is the key in CR technology in achieving higher spectrum utilization. The CR antenna system is shown in figure 1.2.

Since the available idle spectrum can be dynamic, the communicating antenna in the CR antenna system needs to be reconfigurable in nature so that its operating frequency can be synchronously tuned with the command obtained from the sensing antenna. CR system operates in two modes i.e., 'interweave' and 'underlay'. In the interweave mode of operation, as shown in figure 1.3(a), the device searches for white spaces, and decides which white space to allocate for secondary users. The secondary users can transmit without any power constraint in this case. The spectrum-sensing techniques can be wideband or narrowband thereby by leading to wideband or narrowband sensing antenna. As the secondary user transmits in the white spaces, the communicating antenna should be a reconfigurable narrowband. In the underlay mode of operation, as shown in figure 1.3(b), the device searches for white spaces. For this case, there is a constraint on the transmitted power by the secondary users, since both primary and secondary users can occupy the same frequency bands. However, if under certain circumstances, primary users can't tolerate any level of secondary user's interference, the secondary users are forced to transmit over the whole frequency band except at the restricted channels occupied by the primary users. The spectrum-sensing techniques is wideband thereby leading to wideband sensing antenna. As the secondary user can transmit over the entire spectrum with specified interference levels or entire spectrum excluding certain portions, the communicating antenna should be a wideband or wideband with notched narrowband. Figure 1.4 summarizes the different antenna required for CR system.

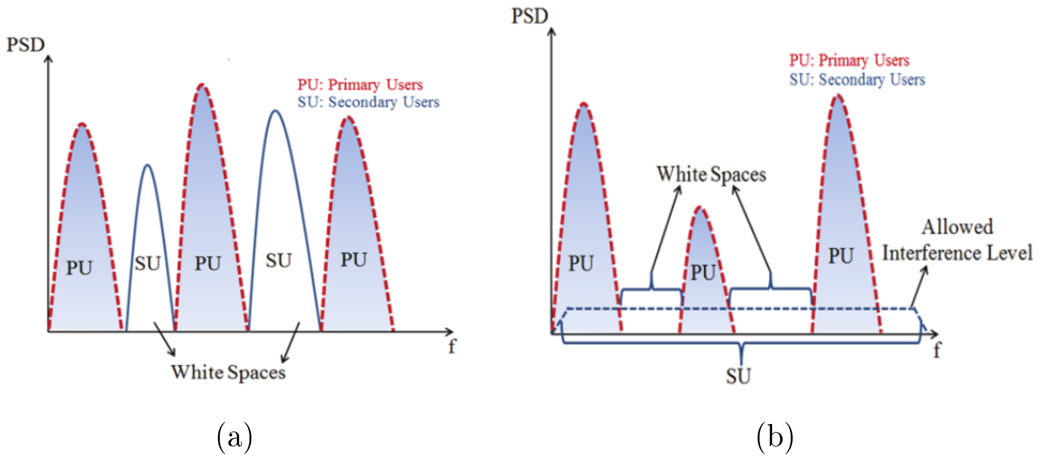

(a) (b)

Figure 1.3: Power spectral density of channel as function of frequency in (a) inter-weave mode (b) underlay mode [Tawk et al. (2014a)]

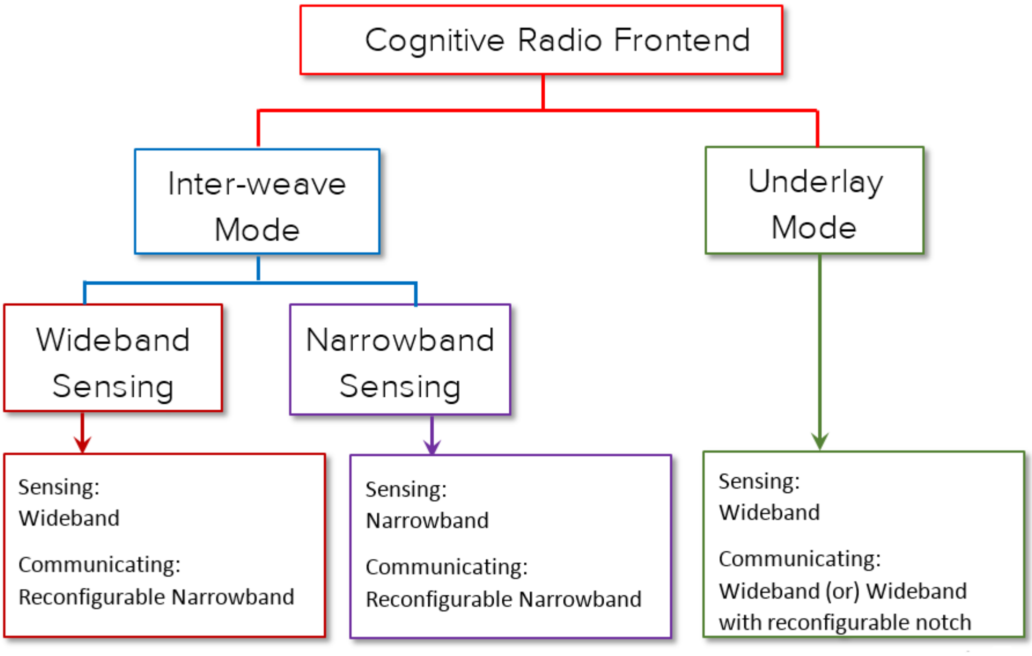

Figure 1.4: Antenna requirements for CR system

The wideband antennas required for sensing can be realized as frequency-independent antenna, travelling wave antenna or multi-resonance antenna [Constantine et al. (2005)]. Frequency-independent antennas electrical characteristics are independent of frequency and shape is expressed in terms of angle. The popular candidates of frequency- independent antennas are spiral, logarithmic antennas. Travelling wave antennas offer smooth transition of fields from antenna to free space. Horn antennas, tapered slot antenna known as vivaldi and antipodal antennas are examples of travelling wave antennas. In multi-resonance antennas, multiple resonances or the higher order modes are combined to make the antenna wideband. The planar log-periodic, planar monopole antennas falls in this category. The planar monopole antenna printed on a dielectric substrate emerged as one of the popular candidates for UWB band due to low profile, wide impedance bandwidth, good radiation characteristics and ease of fabrication [Schantz (2005); Kumar and Ray (2003); Valderas (2011)]. Numerous monopole designs have been investigated utilizing radiating elements of different shapes, including circles, ellipses and squares [Liu et al. (2011, 2010); Liang et al. (2005)].

The requirement of frequency notched UWB antennas arises due to spectrum overlapping of various narrowband services within the UWB spectrum, like, WiMAX (3.3 3.7 GHz), WLAN (5.15 5.85 GHz) and X-band satellite downlink

(7.25 7.75 GHz) etc. This demands the mitigation of these interfering narrow bands for efficient communication utilizing the UWB spectrum leading to the design of ultra-wideband notched antennas. This has been addressed by various groups by introducing intrinsic filtering properties at the desired notch frequencies of the UWB antenna. Majority of these narrow band interference mitigation techniques, aimed to achieve single/dual/triple notches, use various slots [Ojaroudi et al. (2013); Zhang et al. (2008); Abbas et al. (2014); Nguyen et al. (2012); Zhang et al. (2010); Luo et al. (2008)], parasitic resonators and complimentary split ring resonator [Jiang et al. (2012); Chu and Yang (2008)] on the radiator or feed section. However, placing slots on the antenna structures can lead to deterioration on the radiation performance of the antenna to some extent. In addition, the design methodology is highly specific to antenna shape and geometry, not easily adaptable in the radiator of other geometries and neither the notches are easily scalable. Another method commonly employed is to introduce intrinsic filtering properties at the feedline of the UWB antenna. To minimize the footprint of such frequency notched antenna, it is highly desirable to embed the frequency notching elements within the structure with minimum perturbation of its radiation and impedance characteristics in the desired band. This alternative approach to design frequency notched UWB antennas was proposed in [Lin et al. (2012); Sung (2013)], where diverse parasitic resonators were loaded near the radiator or feedline of the antenna for multi-notch application. A new frequency notching technique with minimum impact on the radiating aperture of the UWB antenna by inductive coupling a single pair of split ring resonator (SRR) in the feed region is demonstrated in [Siddiqui et al. (2014)]. The frequency notch can be reconfigured as discussed in earlier section. Narrowband antennas can be realized using microstrip antennas or quarter-wavelength monopoles etc. The reconfigurability in these narrowband antennas can be attained using the design methodology as discussed in previous section.

The existing antennas topologies in CR system are discussed below: Combination of a slotted polygon shaped UWB antenna and accommodating two rotatable triangular shaped patches was proposed by Tawk et. al. [Tawk and Christodoulou (2009)] as a potential CR antenna. A stepper motor based physical rotation of various antenna patches and their sequential contact with the feeding microstrip line has been used in [Tawk et al. (2011)] to design reconfigurable communicating antenna. Recently, a varactor loaded filter integrated antenna, filtenna is demonstrated in [Tawk et al. (2012a)], where excellent frequency reconfigurability is achieved due to tunable bandpass filter element in the feed section of the antenna. This antenna can be utilized as reconfigurable communicating antenna. An IR sensor based motion detector is used in [Costantine et al. (2013)] to realize frequency reconfigurable antenna based on mechanical movement, where the actuation of IR sensor is based on surrounding environment. In [Tawk et al. (2012b)], narrowband reconfigurability antenna achieved by a integrating laser diodes within the antenna structure is placed in close proximity of wideband antenna to demonstrate a CR antenna. The antenna system required for both inter-weave and underlay topologies is demonstrated in [Tawk et al. (2014b)]. In inter-weave scenario, the reconfigurable communicating antenna is realised by integrating a reconfigurable pass band filter in the feed section of the antenna and wideband sensing antenna using a monopole. For underlay scenario, the communicating antenna is realised by integrating a tunable band reject filter in the feed section of the antenna. The communicating antenna in [Costantine et al. (2014)] utilises the physical motion of ground plane realised by Arduino board to attain the reconfigurability. [Ebrahimi et al. (2011)], utilized wideband antenna on top plane and narrowband antenna on the bottom layer to demonstrate the multi-standard radio antenna system. FPGA controlled PIN diodes loaded between four sections of a patch and a main patch has been used in [Shelley et al. (2010)] to achieve reconfigurable characteristics. An autonomous frequency reconfigurable antenna is proposed in [Hinsz and Braaten (2014)], in which a power splitter and bandpass filter is used. However, isolation between the ports of several antennas housed in a circuit remains a challenge. Multi-layered CR antenna system is presented in [Hussain and Sharawi (2015)], where sensing antenna and communicating antenna are placed in different layers. In [Augustin and Denidni (2012); Tang et al. (2016)], a configuration of wideband and reconfigurable narrowband antenna for CR system is demonstrated where the reconfigurable narrowband is achieved by loading the switches in slot of narrowband. A planar UWB/reconfigurable-slot antenna is proposed in [Erfani et al. (2012)], where a varactor diode is placed in slot antenna to provide a reconfigurable narrowband frequency operation. Inter-weave topology of CR antenna system is demonstrated in [Tang et al. (2017)], where communicating antenna is realized by implementing a reconfigurable bandpass filter in the feed section of the antenna. Designing compatible antenna systems for CR applications is more complicated as it requires co-housing of multiple antennas to achieve desired antenna functionality. Technology, challenges and key design parameters of such CR system and CR based antennas has been highlighted in [Christodoulou et al. (2012)] and [Hall et al. (2012)].

1.3 Thesis Contributions

Current dissertation presents design of multi-functional reconfigurable printed antennas and bandwidth controllable dielectric resonator antenna. The multi-functional printed antennas are designed by utilising the combinational loading of SRR and shunt strip in the feed section of the antenna. The bandwidth controllability of cylindrical ring dielectric resonator (CRDR) antenna is realized by parasitic loading of metallic structures on the dielectric resonator. The major contributions of this work can be summarized as:

- Implementation of rotational SRRs in designing compact narrow/wideband notch filters. These filter designs are based on theoretical computation, electromagnetic simulation, circuit simulation followed by fabrication and experimental validation.

- Design of 'multi-functional' antenna having frequency characteristics of wideband, notched wideband and narrowband antenna, which evolves from a single antenna configuration. This is a completely new kind of antenna reconfigurability. The proposed technique utilizes split ring resonators and/or shunt strips loaded in the feed region of the antenna.

- These antennas are referred as 'filtenna'- combination of filter and antenna as the filtering action performed by the combinational loading of SRR and shunt strip before the antenna.

- The multi-functional antenna is implemented in single layer for two type of antennas: circular monopole antenna(CMPA) and tapered slot antenna(TSA), as well as in multi- layer configuration utilizing circular monopole antenna.

- The switching of the antenna functionality is realized using electrical mechanism (PIN diode). Moreover, a mechanical technique to tune the notch/narrow band frequency of the antenna is successfully realized with the help of motor controlled with Arduino Uno Microcontroller.
- Technique for bandwidth controllability in CRDR antenna is proposed which utilizes structural modification (loading the antenna). Two different topologies (metallic cap and metallic sleeve loading) are employed to control the bandwidth. The design equations employing curve-fitting technique is proposed which can precisely predict the bandwidth of the monopole fed CRDR.

1.4 Thesis Outline

Chapter 2 deals with SRR loaded CPW transmission line structures to realize narrowband and wideband band stop filters. This chapter is further classified into two sections. The first section deals with the basics of SRR, its theoretical design and their loading and placement strategy. The second section deals with a multiband and wideband bandstop filter realized by loading the CPW based transmission line with an array of the SRRs, with small modifications in the SRR geometry. The last section deals with the validation of the results through lumped equivalent circuit.

Chapter 3 deals with wideband antenna loaded with SRR and/or shunt strips to attain multi-functional characteristics. Loading the antenna with SRR results a notch in its wideband; further loading the antenna with the shunt strip results in narrowband characteristics. In the first section, two different antennas are loaded with SRR and/or shunt strips to ascertain that this technique is unique and can be applied to various radiators. The limitation of this topology is enhanced feed length of the antenna when number of notches or SRRs to be loaded for achieving these notches is large in number. To alleviate this, multi- layered multi-functional antenna is proposed to reduce the lateral dimension of the antenna when multiple notches are desired in the second section. Here SRRs are placed in two different layers, beneath the substrate and on top of the superstrate thereby significantly reducing the over-all length of the antenna. The functionality of these antennas is validated through simulation and measurements for both impedance and radiation characteristics.

Chapter 4 deals with reconfigurable multi-functional antennas. Here the reconfigurability is attained by two methods, i.e., electrical (by loading PIN diode) and physical (by moving the superstrate). In first section, the shunt strip used in the previous chapter is replaced with PIN diode thereby the different states (OFF/ON) of PIN diode leading to different antenna characteristics. When the PIN diode is in OFF state the antenna has frequency-notched characteristics and in ON state it behaves as narrowband antenna. In second section, the superstrate used in previous chapter is moved physically with the help of motor controlled by Arduino Uno microcontroller to attain reconfigurability. In addition to mechanical reconfigurability, the electronic configurability is also attained with PIN diode. The results are validated with the help of simulation, impedance and radiation pattern measurements along with lumped element equivalent circuit validation.

Chapter 5 deals with the bandwidth controllability in CRDR antenna by structural loading the antenna with metallic structures. The bandwidth is controlled by two different methods of loading i.e., metallic-cap loading on its top and metallic-sleeve loading on the outer surface of the cylindrical ring. The measured return loss exhibits the desired bandwidth control without affecting the peak gain and radiation pattern of the antenna, which is also confirmed by the measured radiation patterns.

The thesis is concluded with **chapter 6** which embodies the concluding remarks on the studies presented in this thesis.

CHAPTER 2

SRR Loaded Transmission Line for Band Reject Filter Applications

2.1 Introduction

This chapter explains about SRR and their application to design narrowband and wideband bandstop filters. The SRRs need to be strategically placed on the desired transmission line for their excitation and thereby inhibition of the signal propagation around its resonance frequency. A new class of SRR known as rotational SRR is utilized, which consist of rotated inner ring compared to conventional SRR. Here the CPW transmission line loaded with rotational SRRs is utilized to demonstrate the design of bandstop filters. The theoretical calculation to predict the SRR's resonance frequency is proposed. The design are validated using electromagnetic simulations, measurements and by lumped element equivalent circuit model.

2.2 Split Ring Resonator: Operation and Applications

Late in 1892, William Weber formulated the theory on diamagnetism. He assumed the existence of closed circuits at molecular scale and utilized Faraday's law to prove that electric currents are induced due to applied time-varying magnetic field. As a result a secondary magnetic flux is created by such currents which oppose the external field, leading to the phenomena of diamagnetism [Lim et al. (2004)]. However, diamagnetic effect associated with the closed metallic rings is not strong enough to produce negative values of permeability. Schelkunoff [Schelkunoff and Friis (1952)] enhanced the magnetic polarizability of the closed metallic loop by loading the loop with a capacitor, and thus forming LC circuit with loop and capacitor. The polarizability of such structures become negative just above the resonance frequency. Pendry [Pendry et al. (1999)] modified the Schelkunoff's proposal, by utilizing two concentric metallic rings with splits on diametrically opposite sides printed on a dielectric substrate known as SRR. Pendry and his group proposed the structure as the first non-magnetic resonator capable of exhibiting negative values of magnetic permeability around its resonant frequency. The SRR has found applications in designing narrow and wideband planar microwave filters [Bonache et al. (2006); Gil et al. (2007); Martin et al. (2003)], novel phase shifter [Saadoun and Engheta (1992)], microwave power divider [Antoniades and Eleftheriades (2005)] etc. SRR has also been considered as a potential candidate for designing compact high gain antennas [Chacko et al. (2013)] and leaky wave antennas [Arnedo et al. (2007); Liu et al. (2002)].

Pendry proposed the SRR of circular geometry. However, lot of other geometrical shapes of SRR namely square, hexagonal, triangular has been proposed by various groups [Saha and Siddiqui (2011)]. The SRR of circular configuration is popularly studied and analyzed by researchers. The structure of circular SRR is shown in figure 2.1. It is formed by utilizing two concentric rings of width, c, and the external ring radius, r_{ext}, and having the inter-ring spacing, d. The splits on the inner and outer rings have identical gap dimensions, g which lie on diametrically opposite sides of the same axis. When an external magnetic field

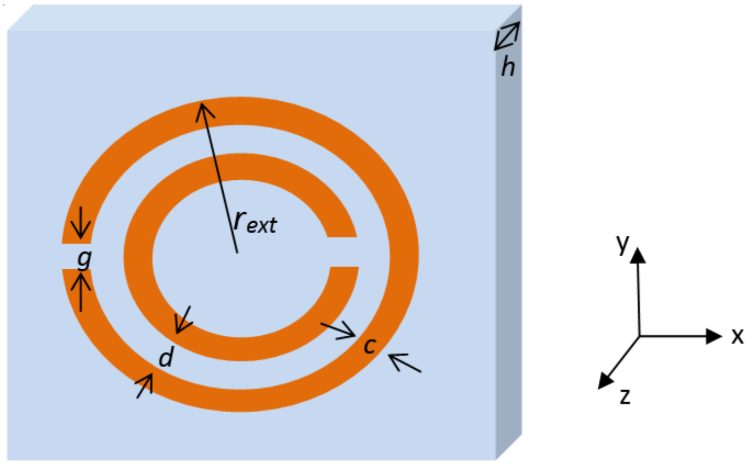

Figure 2.1: Schematic view of a circular SRR formed with metallic rings of width, c, having radii, r_0 and r_{ext}, with inter ring spacing, d and split gap dimensions, $g_1 = g_2$, printed on a dielectric substrate having height, h and dielectric constant, ϵ_r

is applied along the z-axis, an electromotive force appears around the SRR and couples the two metallic rings with the induced current passing from one ring to the other ring through a distributed capacitance formed due to the inter ring spacing. The gap within the rings formed by the splits help to obtain a resonant structure with a much smaller dimension compared to a quarter of a wavelength for a closed, continuous ring. Thus the electrical size of the SRR can be considered small compared to the free space wavelength and a quasi-static model is plausible.

The analysis and characterization of the SRRs is well discussed in [Marqués et al. (2011)]. On excitation with axial magnetic field SRR behaves as a resonant LC tank circuit. The calculation of the capacitance and inductance is required for predicting the resonance frequency of the structure. To calculate the capacitance the magnetic wall condition is imposed at the centre along x-axis, thereby making the structure an edge coupled line with curvature. The geometrical parameters of the SRR affecting its resonance frequency are radius of the rings, r_{ext}, metallization width, c, inter-ring spacing, d, and split gap, g. It was also shown that the resonance frequency can be altered by rotating the rings [Saha and Siddiqui (2012)]. The configuration of the SRR with rotated inner ring and the modified equivalent circuit are shown in figure 2.2.

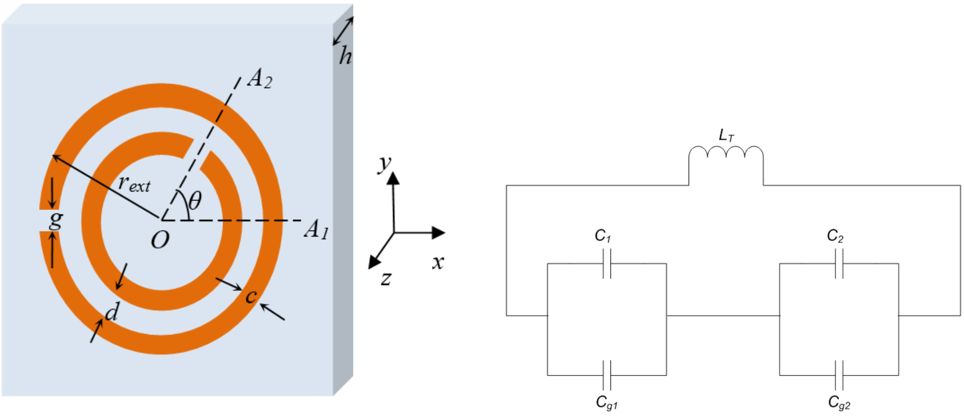

(a) (b)

Figure 2.2: (a) Schematic view of a rotational circular SRR (b) Equivalent Circuit model of a circular SRR shown in (a).

2.3 Theoretical Calculation of Resonance Frequency

The resonant frequency, f_0, of the circular SRR is given by

$$f_0 = \frac{1}{2\pi}\sqrt{\frac{1}{L_T C_{eq}}} \tag{2.1}$$

where, C_{eq} is the total equivalent capacitance of the structure. Again, from the equivalent circuit of figure 2.2(b), the total equivalent capacitance, C_{eq} can be evaluated as

$$C_{eq} = \frac{(C_1 + C_{g1})(C_2 + C_{g2})}{(C_1 + C_{g1}) + (C_2 + C_{g2})} \tag{2.2}$$

Since the split gaps are of identical dimensions $g_1 = g_2 = g$, the gap capacitances $C_{g1} = C_{g2} = C_g$ and the distributed capacitances C_1 and C_2 are also a function of the split gap dimensions, angular orientation of inner ring with conventional ring and the average ring radius r_{avg} and is given as

$$C_1 = (\pi - \theta) r_{avg} C_{pul} \tag{2.3}$$

$$C_2 = (\pi + \theta) r_{avg} C_{pul} \tag{2.4}$$

Considering a metal thickness, t, of the strip conductors, the gap capacitances C_{g1} and C_{g2} can be represented as

$$C_{g1} = C_{g2} = C_0 = \frac{\epsilon_0 ct}{g} \tag{2.5}$$

where, c and t are the width and thickness of the metallic rings, respectively and ϵ_0 is the free space permittivity. and

$$r_{avg} = r_{ext} - c - \frac{d}{2} \tag{2.6}$$

and

$$C_{pul} = \frac{\sqrt{\epsilon_0}}{c_0 Z_0} \tag{2.7}$$

where, c_0 is the velocity of light in free space, ϵ_e is the effective permittivity of the medium and Z_0 is the characteristic impedance of the line. The effective permittivity ϵ_e can be calculated as [(Bahl and Bhartia, 2003)]

$$\epsilon_e = 1 + \frac{\epsilon_r - 1}{2}\frac{K(k')K(k_1)}{K(k)K(k_1')} \tag{2.8}$$

where

$$\begin{align} k &= \frac{c/2}{(c/2)+d} \tag{2.9}\\ k_1 &= \frac{\sinh(\frac{\pi a}{2h})}{\sinh(\frac{\pi b}{2h})} \tag{2.10}\\ a &= c/2 \tag{2.11}\\ b &= (c/2)+d \tag{2.12}\\ k' &= \sqrt{1-k^2} \tag{2.13} \end{align}$$

$K(k)$ is a complete elliptic function of the first kind and $K(k')$ is its complimentary function. An approximate expression for $K(k)/K(k')$ is given as

$$\frac{K(k)}{K(k')} = \begin{cases} \left[\frac{1}{\pi}\ln\left(2\frac{1+\sqrt{k'}}{1-\sqrt{k'}}\right)\right]^{-1} & 0 \leq k \leq 0.7 \\ \frac{1}{\pi}\ln\left(\frac{1+\sqrt{k}}{1-\sqrt{k}}\right) & 0.7 < k \leq 1 \end{cases} \tag{2.14}$$

The characteristic impedance Z_0 is given as

$$Z_0 = \frac{120\pi}{\sqrt{\epsilon_e}}\frac{K(k)}{K(k')} \tag{2.15}$$

Substituting the values of C_0 and C_g in equation (2.2) we get,

$$C_{eq} = \left[\frac{(\pi+q)^2-\theta^2}{2(\pi+q)} r_{avg}C_{pul}\right] q = \frac{c_g}{r_{avg}c_{pul}} \tag{2.16}$$

Hence, the resonant frequency is computed as

$$f_0 = \frac{1}{2\pi}\sqrt{\frac{1}{L_T C_{eq}}} = \frac{1}{2\pi\sqrt{L_T\left[\frac{(\pi+q)^2-\theta^2}{2(\pi+q)} r_{avg}c_{pul}\right]}} \tag{2.17}$$

A simplified formulation for the evaluation for the total equivalent inductance L_T for a wire of rectangular cross section having finite length, l, and thickness, c, is proposed as [Terman (1943)],

$$L_T = 0.0002l\left(2.303\log\frac{4l}{c} - \gamma\right)\mu H \tag{2.18}$$

where, the constant $\gamma = 2.451$ for a wire loop of circular geometry. The length l and thickness c are in mm. This inductance is a function of the winding geometry due to the varying current vectors as described in [Terman (1943)]. The evaluation of the wire length, l, is straight forward as

$$l = 2\pi r_{ext} - g \tag{2.19}$$

For close proximity wires at high frequencies, the current is confined to the wire surfaces and effectively reduces the spacing between them [Grover (2004)]. The finite length l is calculated considering a single loop with r_{ext} as the radius. The resonance frequency of the SRR of square geometry can be calculated by similar procedure and given as,

$$f_0 = \frac{1}{2\pi}\sqrt{\frac{1}{L_T C_{eq}}} = \frac{1}{2\pi\sqrt{L_T\left[\left(2a_{avg} - \frac{g}{2}\right)c_{pul} + \frac{\epsilon_0 ct}{2g_1}\right]}} \tag{2.20}$$

and the equivalent inductance calculated using equation (2.18) with

$$l = 8r_{ext} - g \tag{2.21}$$

and $\gamma = 2.853$ for square geometry.

2.4 SRR Loaded Transmission Lines Based Band Stop Filter

Bandstop filters are key components in the radio frequency, microwave circuit applications in general and wireless communication systems in particular. This filter is required to isolate frequency band located within a wide passband. In active circuit design such as oscillators and mixers, bandstop filters are applied to remove higher order harmonics and other spurious signal. Microwave passive components and devices with multiband and wideband operations is becoming more and more important in modern communication systems of late and have attracted greater attention for their miniaturized and multi-functional operation in portable equipments [Chiu et al. (2004); Xue et al. (2001); Yum et al. (2004)]. The discrete lumped element circuit based band-stop filters uses several types of open-circuited stubs or shunt stubs of quarter wavelengths and suffers from a number of technical limitations which are associated with the use of discrete components and their losses. Most of the designs available in open literature neither maintain the structural compactness nor produce very low insertion loss and moreover suffers from high pass band ripple and slow transition from pass to stop band and vice versa. SRR being a sub-wavelength high-Q resonator offers the advantage of compactness and offers a sharp transition from pass to stop band. SRR when suitably loaded along a transmission line absorbs the signal in and around its resonance frequency. This particular potential has been exploited to design notch filters as detailed in this section. Judicious selection of SRR geometry and dimension enables them for multi-notched as well as wide band-notched application. Here, array of circular SRRs loaded CPW is designed demonstrating two different applications. First one with two pairs SRR of different geometrical parameters along the CPW is designed for dual notch applications. Second one with eight pair of SRRs with gradually varying angular orientation of the inner rings with all other SRR-pair parameters unaltered, exhibits wide-band notched application. Prototypes are designed using commercial electromagnetic simulators Ansys HFSS [ANSYS (2015)] and validated with theoretical calculations, and measurements.

2.4.1 Circular SRR Array Loaded CPW Based Dual-band Frequency Rejection Filter

Figure 2.3 represents the CPW transmission line structure loaded with the rotational circular SRR array along with the detailed geometrical parameters of the SRR. Figure 2.3(a) represents the bottom view of the CPW loaded with the rotational circular SRR array beneath the substrate. Figure 2.3(b) depicts the side view of the structure of figure 2.3(a) where positioning of the SRR is clearly depicted.

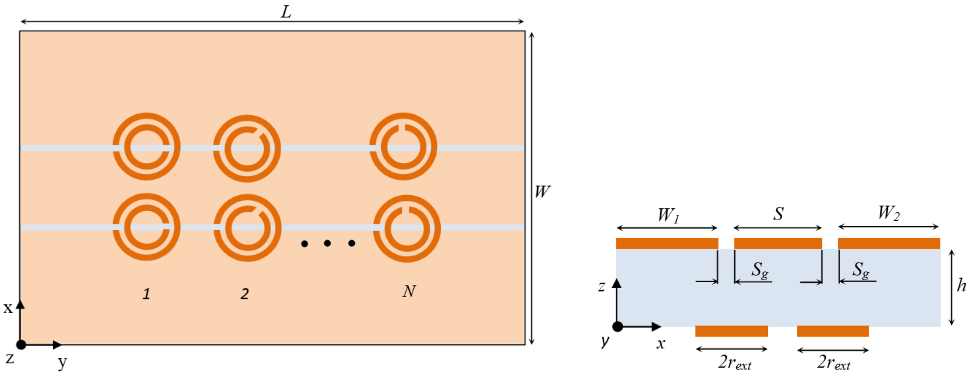

(a) (b)

Figure 2.3: (a) CPW transmission line loaded with an array of circular SRRs with the inner ring angularly oriented. (b) side view of the rotational circular SRR loaded CPW transmission line.

To create multi-band frequency rejection filter, configuration as shown in figure 2.3 is used with the number of SRR pairs to be incorporated depending on the number of rejection bands required. Here a dual notch band is implemented, so the number of SRR pairs utilized is two with similar geometrical dimension and varying angular orientation of the inner ring. Here to demonstrate dual-band rejection filter, two prototypes were fabricated having identical geometrical parameters except prototype-1 having angular orientation of the inner rings as 0^o for SRR pair-1 and 60^o for SRR pair-2 in prototype-1 and for prototype-2 they are chosen as 0^o and 90^o respectively. Figures 2.4(a) and (b) shows the bottom view of two different fabricated prototypes (prototype-1 and prototype-2) of dual SRR

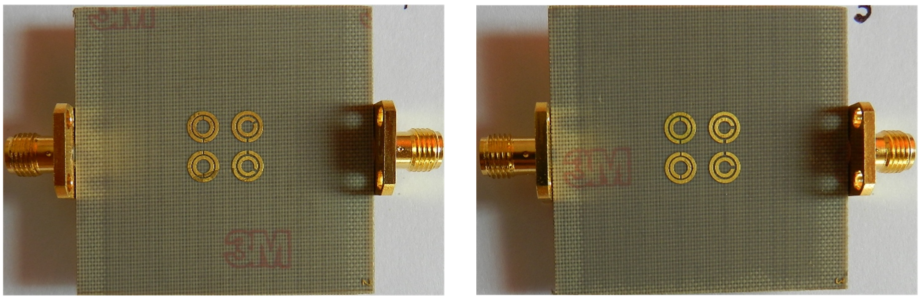

(a) (b)

Figure 2.4: Fabricated prototypes of proposed circular SRR loaded CPW with angularly oriented inner ring (a) Bottom view of prototype-1 (b) Bottom view of prototype-2.

pair loaded CPW medium designed for dual notch function. To ensure a 50 Ω line, the width of the central strip and the slots have been set to $s = 6$ mm and $s_g = 0.3$ mm, respectively, for PTFE laminate with dielectric constant $\epsilon_r = 2.33$, height $h = 1.575$ mm, and loss tangent $\tan\,\delta = 0.0009$. The geometrical parameters of both SRR pairs for both fabricated prototypes are $r_{ext} = 2.2$ mm, $c = 0.5$ mm, $d = 0.2$ mm, $g_1 = g_2 = 0.2$ mm. The angular orientation of the inner rings is 0^o for SRR pair-1 and 60^o for SRR pair-2 in prototype-1. Angular orientations for prototype-2 are chosen as 0^o and 90^o, respectively, to exhibit a wider separation between the two notches.

The above model has been modeled in the EM solver HFSS and the results are plotted in figure 2.5 where we can observe two distinct notches corresponding to two different SRR pairs for prototype-1 and 2. The notch positions can be altered by changing the corresponding SRR geometrical dimensions without disturbing the transmission line structure. For prototype-1, the first resonance measured at 7.62 GHz corresponds to the conventional/un-rotated SRR of $\theta = 0^o$ while the second one measured at 8.28 GHz is due to the rotational SRR of $\theta = 60^o$. The corresponding simulated resonance frequencies are 7.71 and 8.25 GHz, respectively. For prototype-2, as revealed from the plot, the first notch corresponding to un-rotated SRR's resonance is unchanged (compared with figure 2.5(a)), while the second notch is shifted to the higher side of the frequency due to the increased angular rotation of 90^o. The second resonance is measured at 8.55 GHz and the corresponding simulated resonance frequency is 8.64 GHz.

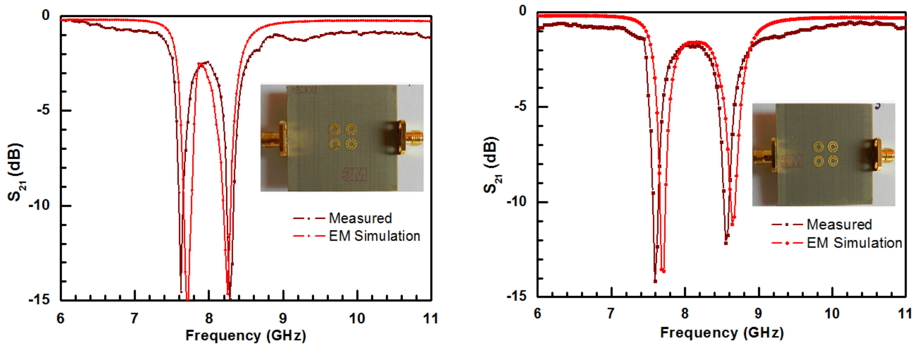

(a) (b)

Figure 2.5: Simulated and measured insertion loss for the dual-notched SRR loaded CPW filter of (a) Prototype-1 (b) Prototype-2.

2.4.2 Wideband Frequency Rejection Filter

To create a wideband rejection filter, the optimum method is to merge narrow notch-frequency bands that are closely separated and make a wideband. To realize this, we utilize the concept of rotating the inner ring of the SRR to achieve gradual frequency shift of the individual pair of SRRs. Hence an array of SRR with identical dimensions with changing angular orientation of the inner rings of the SRRs is designed. For wideband rejection, we utilized eight pair of SRR elements, placed on backside of the substrate below the slots for maximum coupling. Another point to be considered for multiple SRR loading on the CPW host line is the possible unwanted mutual coupling between the two adjacent elements which can perturb the resonance profile required for the present application. This can happen if the SRR pairs of two successive elements are very close enough such that their flux lines interlinks mutually. To avoid such unwanted mutual coupling effect current design considers an optimum edge-to-edge inter element distance of 2 mm. The dimensions of the structure are presented in Table 2.1 and the angular orientation of the SRR are presented in Table 2.2.

The proposed model has been fabricated in RT duriod 5870 laminate with $\epsilon_r = 2.33$ and tan $\delta = 0.0012$. Figure 2.6 shows the fabricated prototype of the

Table 2.1: Dimensions of the host CPW line loaded with rotational SRR of circular geometry $\epsilon_r = 2.33$, tan $\delta = 0.0012$, $h = 0.787$ mm and $t = 0.035$ mm

Structure	Parameter	Dimension (mm)
SRR	r_{ext}	2.2
	c	0.5
	d	0.3
	$g_1 = g_2 = g$	0.2
CPW	W	40
	L	73.2
	S	6
	k	0.3

Table 2.2: Angular orientations of the inner rings of the SRR to obtain the wideband band stop filter characteristics

Ring	Angular Rotation, θ (deg)
SRR Pair 1	0(Reference)
SRR Pair 2	15
SRR Pair 3	30
SRR Pair 4	45
SRR Pair 5	60
SRR Pair 6	70
SRR Pair 7	80
SRR Pair 8	90

proposed model. The measurement results are compared and plotted in figure 2.7 along with the lumped element equivalent method and one of the simulator results. Here it is observed that the measured results shows good correspondence with that of EM simulated.

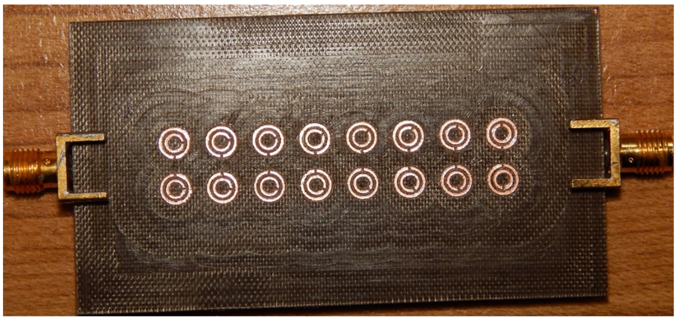

(a)

(b)

Figure 2.6: Fabricated prototype of SRR array loaded CPW for wideband rejection filter (a) top view (b) bottom view

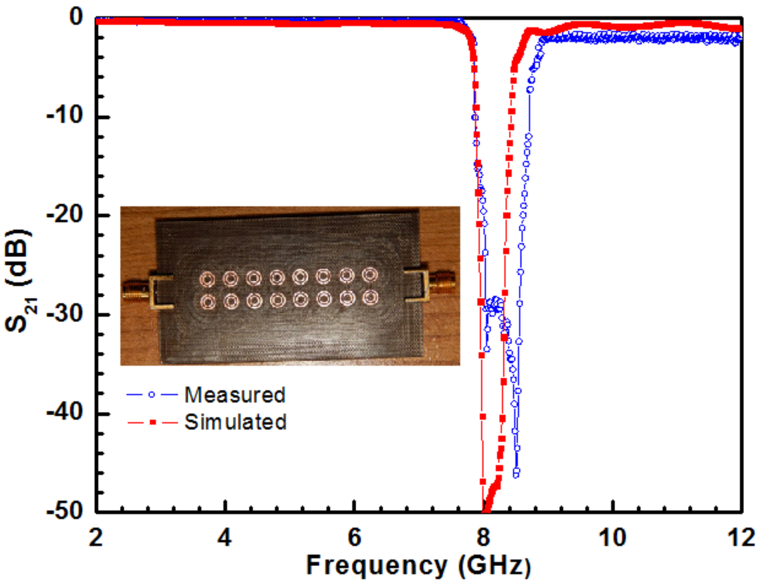

Figure 2.7: Simulated and measured insertion loss for the wide stop-band SRR loaded CPW filter with gradually changing angular orientation inner rings.

From the measured data, it is evident that, we are able to band reject upto 810 MHz by maintaining the compactness, the overall dimension of the proposed structure being 73.2×40×0.787 mm^3 and with rejection levels of -30dB. Both pre and post resonance pass band performance is also satisfactory with insertion loss less than 2 dB. The post resonance insertion loss is bit more when compared to pre-resonance due to the fact that negative permeability-frequency curve of SRR shows sharp pre-resonance and gradually flattened post-resonance profile resulting in asymmetrical resonance characteristics.

2.5 Lumped Element Based Equivalent Circuit Validation

Resonance in the SRRs is contributed by time-varying magnetic field components of the propagating electromagnetic signal along its axis and hence, they can be modelled as the LC resonant tank circuit [Smith et al. (2000)]. As SRRs are electrically small at their resonance, the host CPW medium can also be represented by lumped element equivalent circuit. Using the lumped equivalent circuit of SRR and host CPW medium, we obtain the resultant lumped equivalent circuit of the dual-notched filter with varying angular orientation of the SRR pairs as shown in figure 2.8.

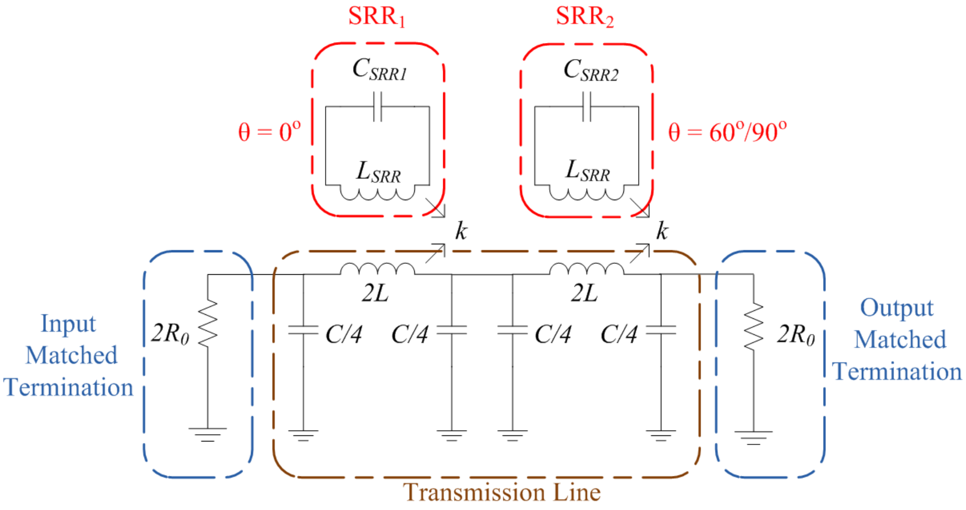

Figure 2.8: Lumped element equivalent model of the proposed dual notch SRR loaded CPW filter for the fabricated prototype-1 and prototype-2. Due to symmetry, the magnetic wall concept has been used and the circuit corresponds to one half of the structure.

Applying symmetry along the CPW longitudinal axis, the CPW is modelled as a series inductor, L and parallel capacitor, C. The CPW inductance and capacitance are obtained as $L = p*L_{pul}$ and $C = p*C_{pul}$ where L_{pul} and C_{pul} are per unit length inductance and capacitance of the CPW and p is the unit cell size, obtained from the SRR size and distance of separation between two successive SRR pair. Due to symmetry, the inductor has value $2 * L$ and capacitor has $C/4$. Finally, it should be ensured that the equivalent circuit must be excited with a termination port. The characteristic port impedance should be equal to $2 * Z_0$, because the complete coplanar line has been designed with a characteristic impedance of Z_0.The SRR is modelled as LC circuit with L_{SRR} and C_{SRR} as the self-inductance and capacitance of the SRR and the coupling between the SRRs and the CPW is represented by a coupling coefficient, $k = 2 * s_g/h$. Two different SRR pairs with varying angular orientations of 0^o and 60^o (for prototype-1) and 0^o and 90^o (for prototype-2) are modelled as two tank circuits with same self-inductance L_{SRR} but with different equivalent capacitance C_{SRR1} and C_{SRR2}, respectively. The change in capacitance is caused by the changing angular orientations between the inner and outer rings, respectively, and is calculate as discussed in section 2.3.

The equivalent circuit parameters for SRR pairs loaded in prototype-1 are $L_{SRR} = 6.11$ nH, $C_{SRR1} = 74.51$ pF (SRR pair-1 of $\theta = 0^o$), $C_{SRR2} = 74.51$ fF (for SRR pair-2 of $\theta = 60^o$), respectively. For prototype-2, C_{SRR2} reduces to 66.32 fF due to the increased value of $\theta = 90^o$ with all other parameters remaining same. Circuit parameters for a unit cell size of $p = 6.4$ mm is obtained as $L = p * L_{pul} = 1.43$ nH and $C = p * C_{pul} = 0.443$ pF. The magnetic coupling between the host CPW line and the SRR is $k = 0.38$. Figure 2.9 shows the comparison of the lumped equivalent circuit simulated in Agilent ADS [Agilent (2015)] with the measured and EM simulated results for both prototypes. The corresponding lumped element equivalent model resonance frequencies are 7.61 and 8.07 GHz, respectively, for prototype-1 showing close correspondence between measured, simulated, and lumped model data as shown in figure 2.9(a). As revealed from the plot, the first notch corresponding to unrotated SRR's resonance is unchanged (compared with figure 2.9(a)), while the second notch is shifted to the higher side of the frequency due to the increased angular rotation of 90^o.

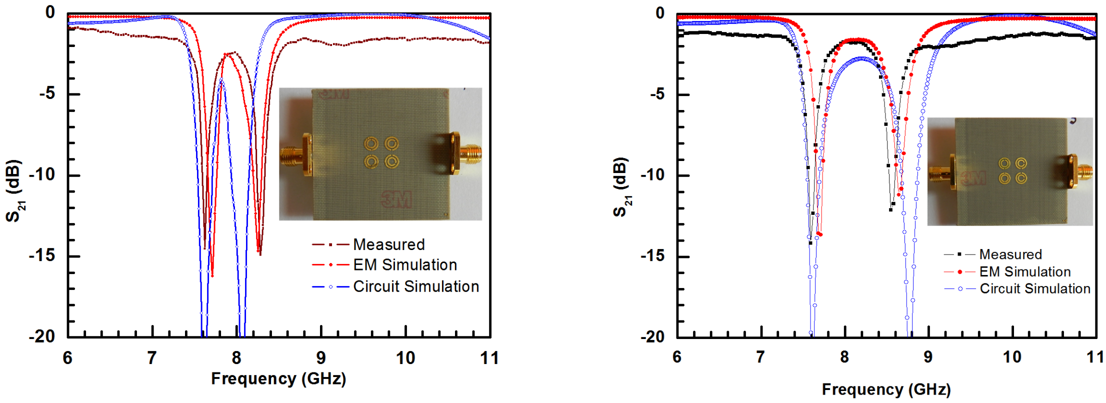

(a) (b)

Figure 2.9: Simulated (HFSS), lumped element equivalent model, and measured insertion loss for the dual-notched SRR loaded CPW filter (a) prototype-1 with $\theta = 0^o$ and $\theta = 60^o$ (b) prototype-2 with $\theta = 0^o$ and $\theta = 90^o$

2.6 Conclusion

A new technique of rotational SRR loaded CPW-based multinotch and wideband bandstop filter has been proposed in this chapter. The design strategy is based on the angular orientation between the two rings without changing the SRR dimension. The proposed structure is very compact, frequency scalable and can be configured for more number of notches/broader stop band by utilizing more number of SRR with proper dimension and orientation of the inner ring without significant overall size increment as the size of the SRR are very small. The designed filter exhibits very low insertion loss in the pass band and quite high rejection level in the stopband due to strong magnetic coupling between host CPW and loaded SRR making it a potential candidate for various frequency rejection applications.

CHAPTER 3

Multi-Functional Antennas with SRR and/or Shunt Strip Loading

3.1 Introduction

The cognitive radio systems as discussed in preceding chapter requires antennas which are multi-functional having various antenna functionalities. To be more specific, here we need radiators with wideband, wideband with frequency-notch, narrowband impedance characteristics and consistent radiation pattern. Though such responses can be achieved by placing multiple radiators in a common platform, it is more desirable to invoke all the characteristics using minimum number of radiators, if possible with a single radiator. Advantage of replacing multiple antennas for different functionalities with a single multi-functional antenna are manifold:

1. reduces the real estate or foot print required
2. eliminates the design challenges associated with providing isolation between multiple antenna elements
3. reduces the cost and
4. eliminates the need of additional filtering elements required.

In this chapter, a new reconfigurable multi-functional antenna both in single and multi-layered configuration are introduced. The multi-functional characteristics are obtained by loading the antenna with SRR and/or shunt strip in the feed section of the antennas. The combinational loading of SRR and shunt strips in the feed section provides the filtering prior to the antenna and hence these antenna can be viewed as combination of filter and antenna or referred as ‘filtenna’. The novelty of the proposed multi-functional antenna are many folds:

1. it achieves multiple antenna functionality from the same antenna without altering the radiator

2. complementary narrow band response is evolved from the same UWB antenna without using additional radiator/radiating elements which results in increased antenna dimensions and requires additional electromagnetic isolation means

3. scaling for any other combination of notches by tailoring the SRR dimensions alone without changing the radiator or the ground plane

4. radiation pattern of the narrowband configurations is almost identical to that of UWB monopole antenna and frequency notched UWB monopole antenna and

5. the proposed concept is applicable to any other CPW/microstrip fed UWB antenna.

3.2 Single Layered Multi-Functional Antenna

To demonstrate that the multi-functional characteristics achieved are independent of the radiator, two different antenna configurations are used. Initially, the multi-functional characteristics are demonstrated for CMPA and later on a CPW fed TSA. The radiation mechanism of both the antennas are different, one being multiple resonance antenna and other being travelling wave antenna.

3.2.1 Circular Monopole Based Multi-Functional Antenna

The proposed antenna is designed to yield multiple notches in the UWB spectrum and can also be configured to yield narrow band responses. A single CPW fed printed CMPA is loaded with multiple SRRs with different angular orientations of the inner and outer rings. This varying angular orientation changes the effective capacitance between the SRR rings printed in the feed section of the antenna. This in turn changes the resonance frequency of the SRR and contributes to multiple frequency notches in the UWB radiation. To excite strong magnetic resonance, the

SRRs are placed just beneath the slots of the CPW with their centers aligned with the centers of the slot lines. Such positioning of the SRRs also ensure minimum impact of the SRR on the antenna's radiation field. This in turn guarantees unperturbed radiation characteristics of the SRR loaded antenna in the entire UWB band excepting at the desired notch frequency. The SRR loaded printed monopole is further loaded with copper switches aligned with the SRRs on the feed section to provide multiple narrowband functionality. Thus, a single antenna effectively yields UWB operation, frequency notched UWB operation and narrowband operations centered at three different frequency bands, depending on different loading of SRRs and/or copper strips on the feedline. Frequency notching of the UWB antenna is caused by the SRRs which are magnetically coupled with feeding CPW line and inhibit signal propagation around its magnetic resonance frequency effectively acting as a high Q notch filter. The narrowband operations are due to the formation of a narrow bandpass filter (BPF) around SRRs resonance frequency contributed by SRR and the copper strip.

The proposed antenna is composed of printed circular monopole antenna fed by a CPW based transmission line loaded with SRRs beneath the CPW as shown in

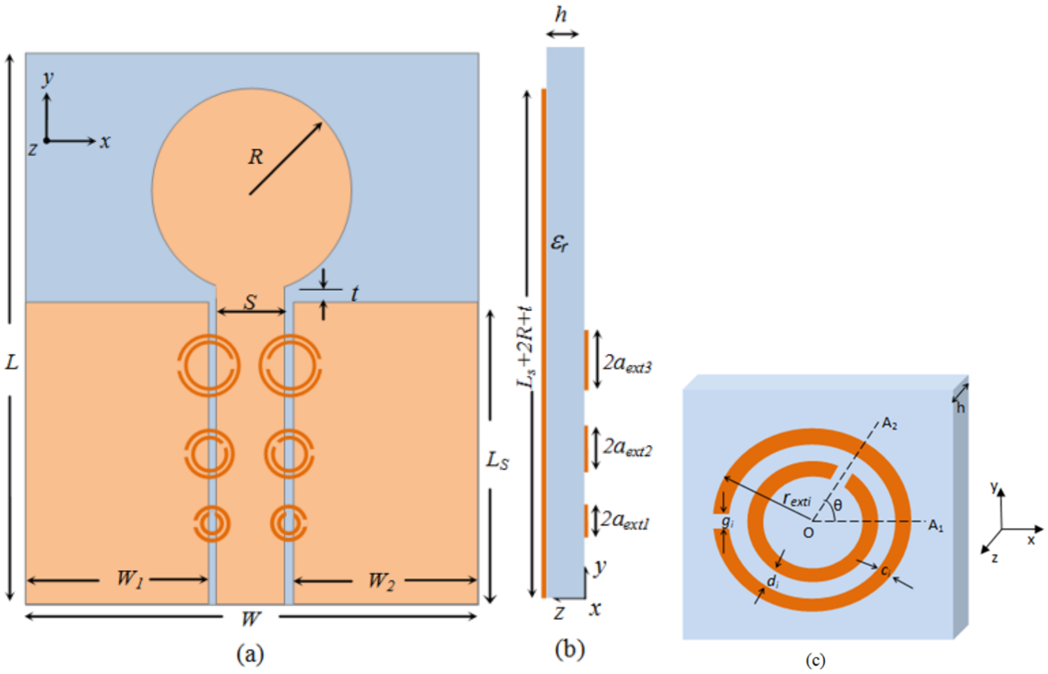

(a) (b) (c)

Figure 3.1: Schematic of a CPW fed CMPA loaded with circular SRR having rotated inner rings (a) Top view (b) Side view (c) Enlarged view of the circular SRR.

figure 3.1(a) & 3.1(b), providing frequency notched UWB response where size and orientation of the SRR is tailored to achieve three notch frequencies. The circular monopole of radius $R = 12.9$ mm is fed by a CPW consisting of ground planes having with $W_1 = W_2 = 21.15$ mm, length $L_s = 40$ mm and signal line having width $S = 7$ mm and length, $L_s + t = 40.2$ mm and act as the basic building block (Configuration A) for all other configurations (Configurations B, C, D and E). The widths of the slots between the ground planes and signal line, $s_g = 0.35$ mm, is chosen to ensure impedance (50 Ω) matching with the commercial connector.

Frequency Notched UWB Antenna (Configuration B)

For achieving triple notches, three pairs of circular SRRs with varying physical dimension and orientation of the inner ring of the SRR are chosen, each providing notch at their respective resonance frequency. Figure 3.1(c) shows the schematic diagram of the circular SRR, having external radius r_{exti}, conductor thickness c_i, separation between rings d_i, split gap g_i and orientation of inner ring, θ_i. These parameters are used to control the SRR's resonance, contributing to the notch frequency of the antenna. The resonance frequency of a rotational SRR being substantially greater than that of conventional SRR ($\theta = 0^o$) of same physical dimensions [Saha and Siddiqui (2012); Saha et al. (2015)], angular orientation of the SRR helps in using a relatively big size-SRR (larger r_{ext}) to achieve same resonance frequency. It becomes difficult to get a notch at higher frequency using a conventional SRR of reduced r_{ext} which yields in a weak resonance phenomenon. This issue of weak resonance which is due to reduced excitation of SRR for smaller r_{ext} can be mitigated by optimally using rotational orientation of SRR. The fabricated prototype of this configuration is shown in Figure 3.2(a) and 3.2(b). The magnified view of figure 3.2(b) clearly indicates the gradually changing orientation of the inner rings of the SRR.

The prototypes having an over-all size of $50 \times 70 \times 1.575$ mm^3 are designed on RT duroid (ϵ_r=2.33, tan $\delta = 0.0012$, $h = 1.575$ mm) and simulated using a commercial electromagnetic simulator [ANSYS (2015)]. Table 3.1 summarizes the design parameters of the SRRs used to achieve triple notch functionality. It is to be noted that the over-all envelope of the SRR (r_{ext}) and rotational orientation of the inner ring of the SRRs are chosen as the controlling parameter of SRR's resonance frequency. The prototypes are validated with reflection coefficient and radiation pattern measurement using Agilent PNA-X N5224A network analyzer and a fully calibrated near field anechoic chamber. The radiation pattern measurements were performed using a broadband pre-amplifier (Agilent 83051 A) coupled broadband horn as the transmitting antenna while the SRR loaded CMPA was in receive mode for various configurations.

The measured and simulated plots for the S_{11} versus frequency of the proposed rotational circular SRRs loaded CMPA are shown in figure 3.3 and compared with

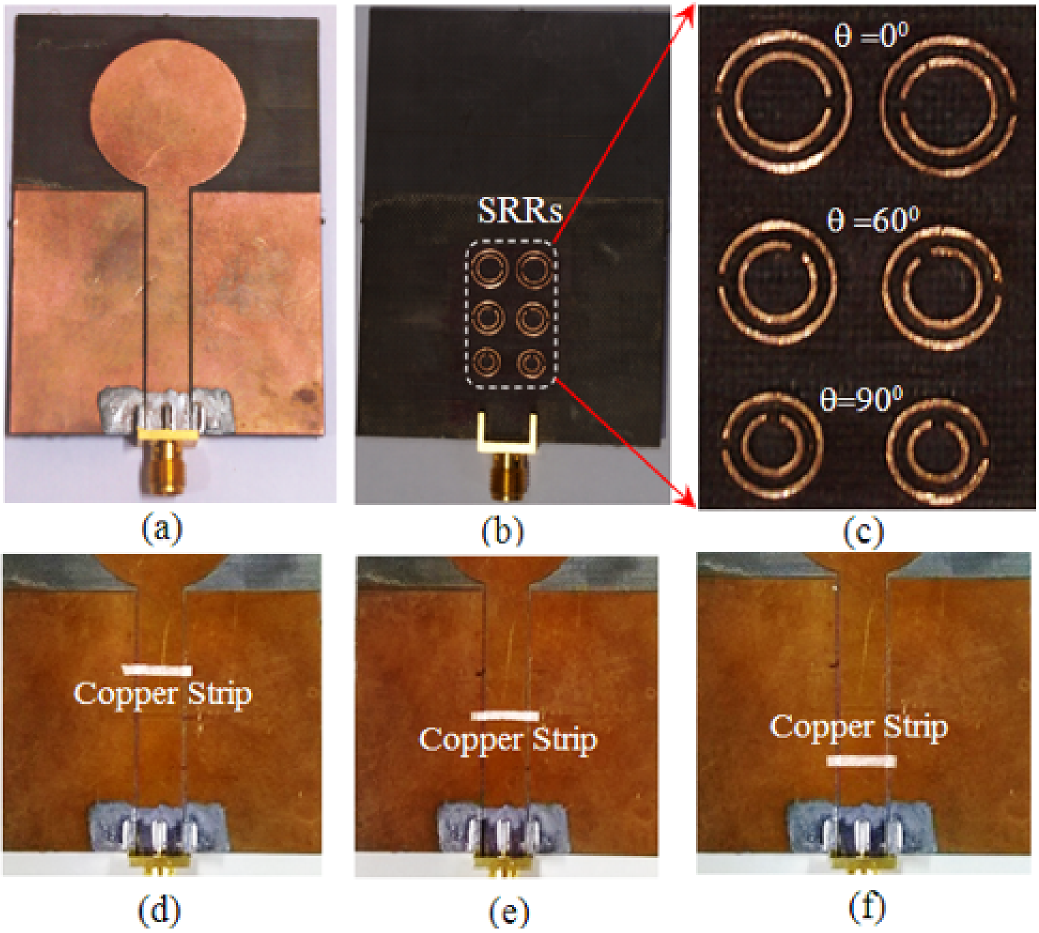

Figure 3.2: Fabricated prototype of the CPW fed CMPA loaded with circular SRRs with rotated inner rings (a) Top View (Configurations A and B) (b) Bottom View with loaded SRRs (Expanded view showing rotational orientation of inner rings) (c) Top view (Configuration C to E) obtained by loading copper strip, on the CPW line, aligned with different SRR pairs.

Table 3.1: Design parameters of the rotated circular SRRs loaded with the CMPA printed on a dielectric substrate having $\epsilon_r = 2.33$, tan $\delta = 0.0012$. (Parametric variables as in figure 3.1)

Design Parameter	Dimensions (mm)		
	Pair 1 ($i = 1$)	Pair 2 ($i = 2$)	Pair 3 ($i = 3$)
r_{exti}	3.2	2.8	2.4
c_i	0.5	0.5	0.5
d_i	0.4	0.4	0.4
g_i	0.3	0.3	0.3
Theta, θ_i	0^o	60^o	90^o

unloaded case (configuration A) of [Siddiqui et al. (2014)]. As revealed from the figure, the simple CPW fed CMPA without any SRR loading operates from 2.6 GHz to 10.8 GHz with resonance dip around 3 GHz (corresponding to the quarter wavelength resonance of the disc diameter) while, the same antenna when loaded with rotational SRRs, provides three distinct notches at 5.09 GHz, 6.34 GHz and 8.04 GHz contributed by corresponding SRR pair for measured results against

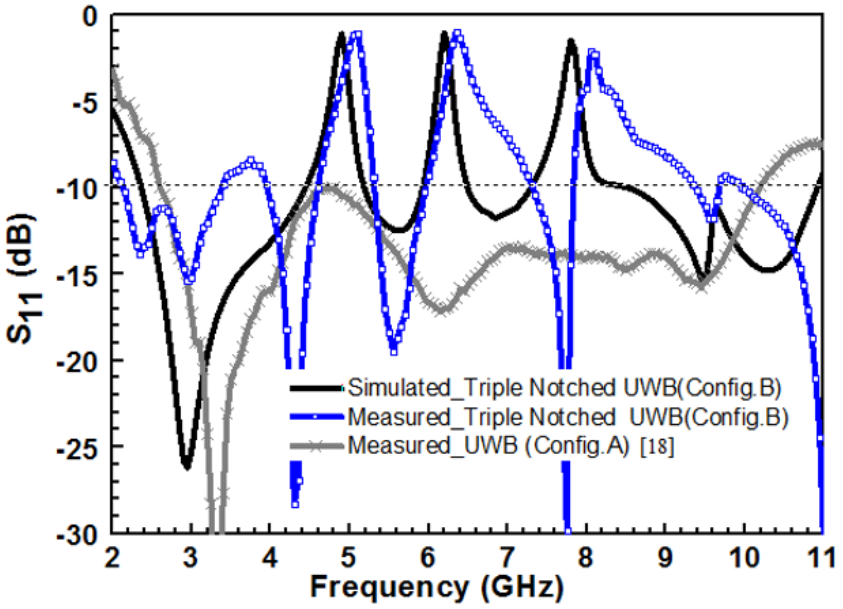

Figure 3.3: Simulated and measured S_{11} characteristics of the proposed CPW fed CMPA with three pair of SRRs printed beneath the feedline for triple notched UWB response (Configuration B)

4.81 GHz, 6.19 GHz and 7.8 GHz for simulation. The uniqueness of the notching technique lies in its generality and versatility in i) scaling for any other combination of notches by tailoring the SRR dimension without any change on the radiator and ground plane and ii) applying the proposed concept for any other CPW/microstrip fed UWB antenna. Figure 3.4 shows the E and H-planes measured normalized radiation patterns of the proposed antenna configuration at 4.2 GHz, 6 GHz, 7.2 GHz and 9.4 GHz exhibiting monopole type radiation pattern with axial null for E-plane and near omni-directional pattern for H-planes. The frequencies are selected at different points over the entire UWB spectrum, excluding the notch frequencies where there is no effective radiation from the antenna. The measured and simulated maximum realized gain values versus frequency of the proposed multiple SRR loaded antenna, plotted in figure 3.5, exhibits drastically reduced gain of the SRR loaded antenna (- 9.6 dBi at 5.08 GHz, -12.7 dBi at 6.35 GHz and -4.27 dBi at 8.1 GHz) reconfirming the presence of strong notches contributed by the SRRs resonance. The maximum realized gain at other frequencies is within 0-4 dBi, and is almost similar to simple CPW fed UWB antenna (configuration A) of [Siddiqui et al. (2014)].

Figure 3.6 shows the simulated surface current distribution of the proposed antenna (configuration B) at three notch frequencies which clearly indicates non-

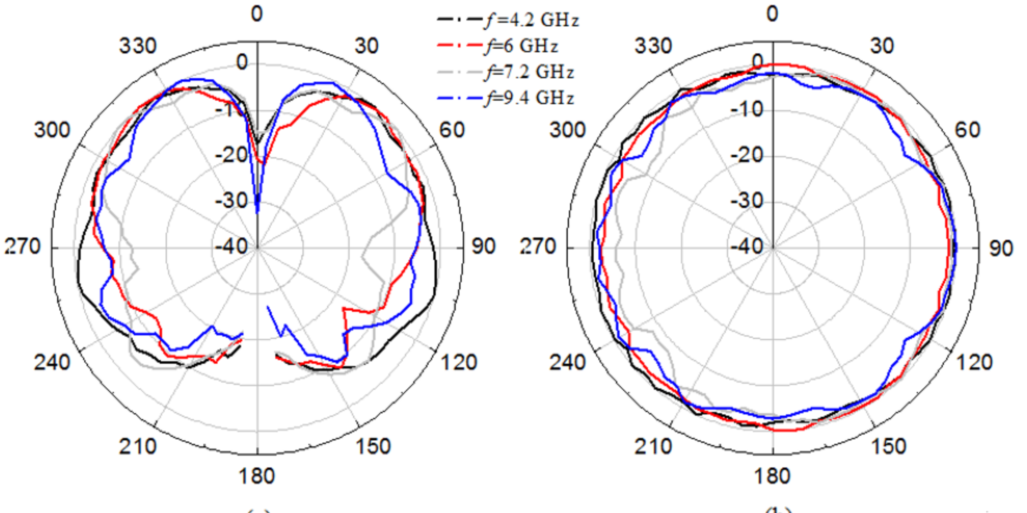

(a) (b)

Figure 3.4: Measured normalized (a) E (x-y) and (b) H (x-z) plane co-pole radiation pattern of the triple notched CPW fed CMPA (Configuration B) at various frequencies

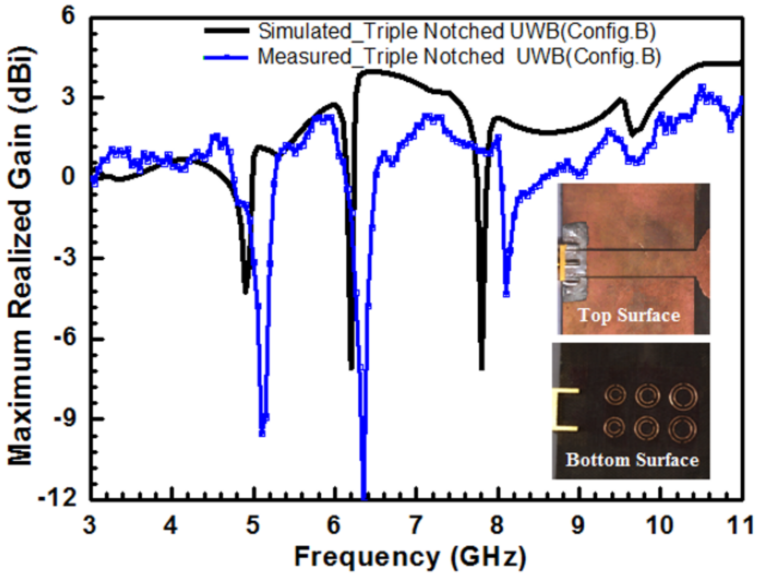

Figure 3.5: Simulated and measured maximum realized gain (x-y plane) characteristics of the proposed CPW fed CMPA with three pairs of SRR printed beneath the feedline for triple notched UWB response (Configuration B)

excitation of the antenna due to strong magnetic resonance of corresponding SRR pair which in turn inhibit the signal to excite the antenna.

Another unique and more insightful way to exhibit the antenna excitation/notching is to plot the magnitude of the Poynting vector along the feedline of the antenna as a function of distance from the feed port to the radiator and frequency in a rectangular contour plot as shown in figure 3.7. Figure 3.7 clearly demonstrates existence of triple notches contributed by each SRR pair indicated by the three lighter shade (greenish in colour) lines. It is interesting to note that the first notch (at 4.81 GHz) starts at a longer distance as this is contributed by largest SRR which is farthest from the feed port of the antenna; similarly second (at 6.19 GHz) and third notch (at 7.8 GHz) starts at a relatively lesser distance from the preceding notch due to their closer proximity to the feed-port of the antenna.

The proposed multiple notched configuration can be converted to achieve a single wideband notched antenna by selecting SRR size and angular orientation in a way so that, individual resonance are slightly shifted from preceding SRR pair, resulting in wider rejection band. The wider rejection band has been achieved for same geometrical parameters of each SRR pair (r_{ext} = 2.8 mm, c = 0.5 mm,

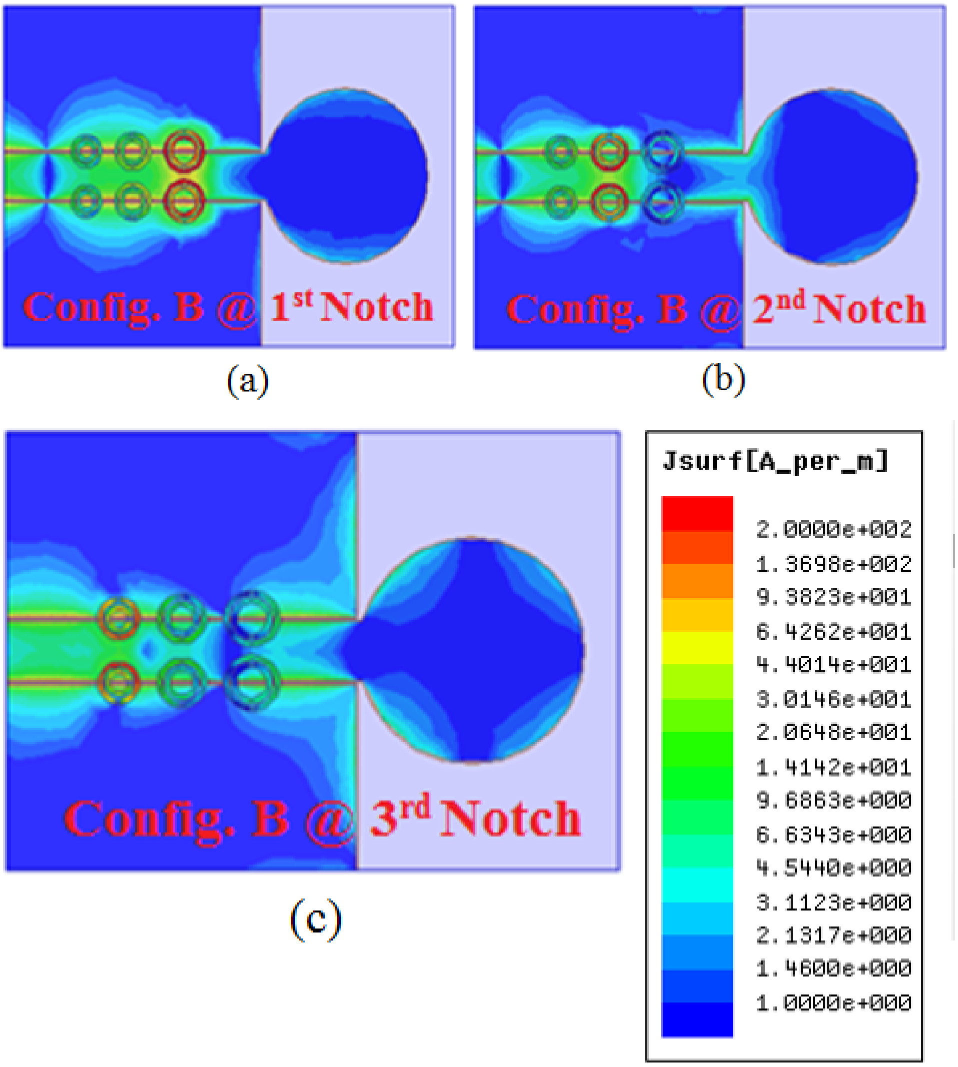

(a) (b)

(c)

Figure 3.6: Simulated surface current distribution of the CPW fed CMPA loaded with circular SRRs with rotated inner rings, with and without copper strips (Configuration B) at notch frequencies 4.87 GHz, 6.21 GHz, and 7.74 GHz

d = 0.4 mm and g = 0.4 mm) and varying only angular orientation $\theta = 0^o, 60^o$ and 90^o for three SRR pairs. This also shows the generality and scalability of the proposed techniques of frequency notching. Figure 3.8 shows the simulated S_{11} and maximum realized gain of the proposed antenna versus frequency. The plot clearly indicates the presence of notch band from 5.75 GHz to 6.4 GHz ($|S_{11}| < 5$ dB) providing a notch bandwidth of 625 MHz. The simulated gain of the antenna falls below -10dB over this notch-band and maintains nearly flat-profile over the other frequency band. As introduced previously, figure 3.9 shows the simulated Poynting vector along the feed line of the antenna. This plot reveals a wider

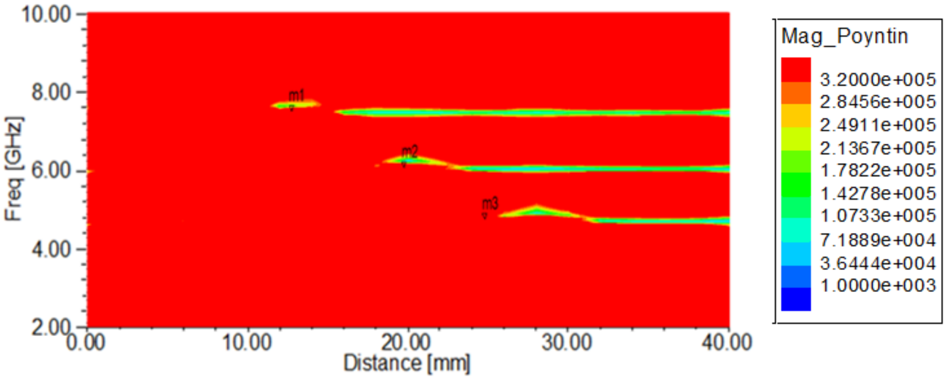

Figure 3.7: Simulated contour plots of poynting vectors of the propagating electromagnetic energy through the longitudinal dimension of one of the slots as a function of frequency for Configuration B (triple notched UWB antenna), indicating three notch frequencies corresponding to SRR's position

rejection band indicated by gradually increasing width of the lighter (greenish and bluish in colour) shade which is due to superposition of narrowly separated individual notches by different SRRs along the CPW line.

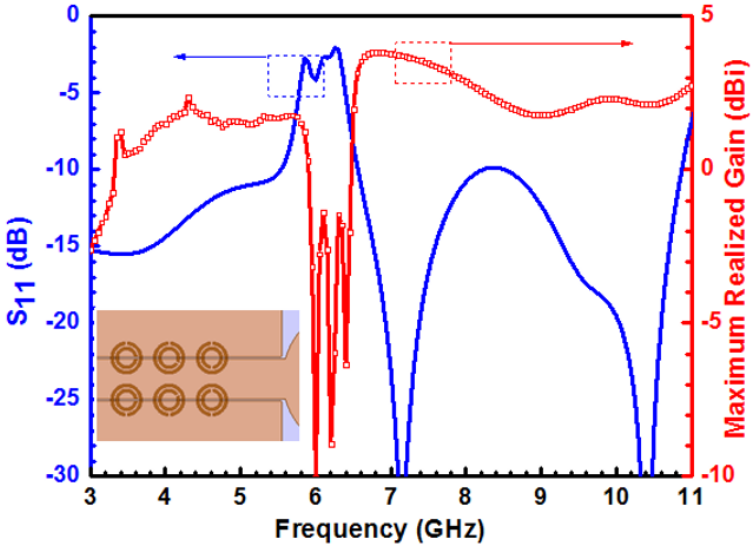

Figure 3.8: Simulated S_{11} and maximum realized gain (x-y plane) characteristics of the proposed CPW fed CMPA with three pairs of SRR printed on the beneath the feedline for wideband notched UWB response

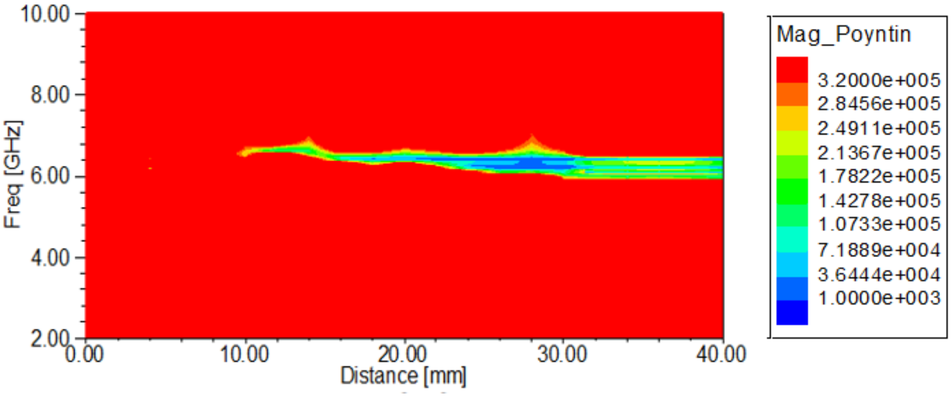

Figure 3.9: Simulated contour plots of Poynting vectors of the propagating electromagnetic energy through the longitudinal dimension of one of the slots as a function of frequency for wideband notched UWB antenna

Narrowband Antennas (Configuration C, D and E)

Combination of SRR and shunt strip loading on a CPW medium constitutes a very narrow passband around SRRs resonance frequency and provides an exactly complementary response to only SRR loading on the CPW. This particular shunt strip can be activated/deactivated by various electronic means and can be used to convert a frequency notched UWB antenna to a narrowband one. Figure 3.2 shows the modification of the configuration B to achieve the narrowband configurations from the same proposed antenna. Three different narrowband configurations, namely configuration C, configuration D and configuration E operating at 5.24 GHz, 6.4 GHz and 7.85 GHz are realized by adding copper strip on the back side of the SRR-pair-1(largest SRR , $\theta = 0^o$), SRR-pair-2 (medium SRR, $\theta = 60^o$) and SRR-pair-3 (smallest SRR, $\theta = 90^o$) respectively. This is realized by gluing copper tape of width $w_s = 0.8$ mm, to short the signal and ground planes of the CPW line with corresponding SRR pairs lying exactly on the opposite side. This complementary nature of the antenna is experimentally verified and summarized below:

Configuration C

In this configuration the copper strip is loaded beneath the largest SRR pair (farthest from the feed port, $r_{ext} = 3.2$ mm and $\theta = 0^o$) resulting in a narrowband antenna response around resonance frequency of SRR. Figure 3.10 shows the simulated and measured plots for S_{11} versus frequency exhibiting a narrowband response around 5.24 GHz for measured plot against 5.11 GHz for simulation. The mismatch between measured and simulated results can be attributed to the imperfection in exact positioning of copper switch, impact of adhesive on the substrate and can be improved by more professional and sophisticated fabrication. It is to be noted that two interim matching points are observed at higher side of this band. This may be due to weak excitation of the second and third SRR pair contributing to a weak impedance matching. The measured normalized co-polarized radiation pattern of this configuration, for two principal planes are presented in Figure 3.11. The figure depicts nearly monopole type radiation pattern having axial null for E-plane and omni-directionality in H-plane.

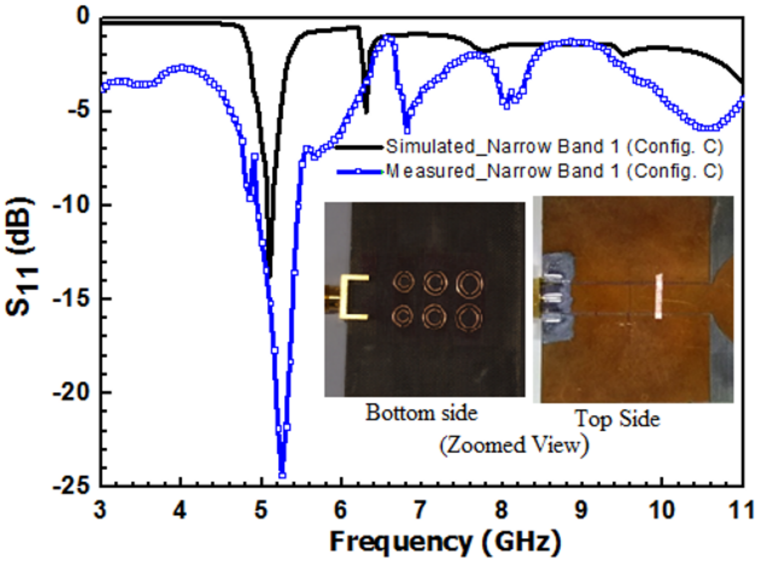

Figure 3.10: Simulated and measured S_{11} characteristics of the configuration C. Plot indicate narrowband performance around resonance frequency of the largest SRR pair coupled with shunt strip. Inset shows the zoomed top and bottom view of the antenna

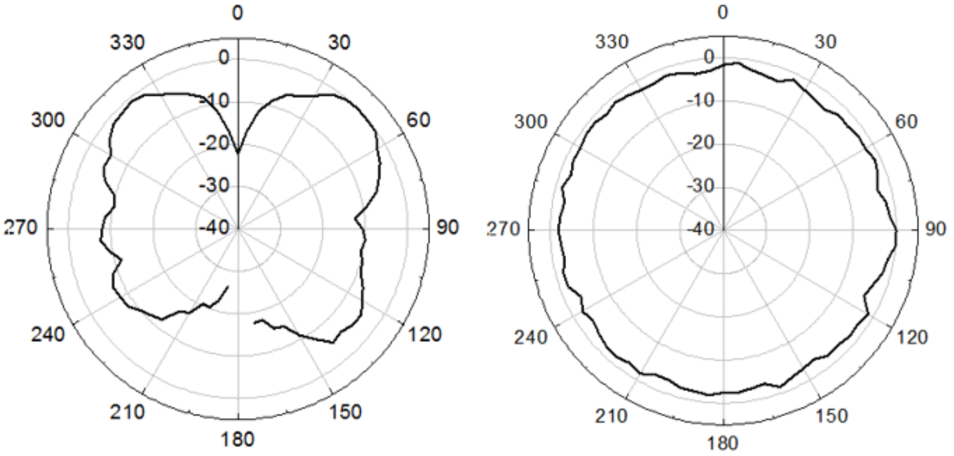

(a)

(b)

Figure 3.11: Measured normalized (a) E (x-y) and (b) H (x-z) plane co-pole radiation pattern of the narrowband antenna of configuration C.

Configuration D

This configuration is realized by loading the copper strip beneath medium sized SRR pair (intermediate SRR pair, $r_{ext} = 2.8mm$ and $\theta = 60^o$). This results in a new narrowband response of the antenna around corresponding SRR pair's resonance. Figure 3.12 shows the simulated and measured plots for S_{11} versus frequency exhibiting good correspondence with measured narrowband response

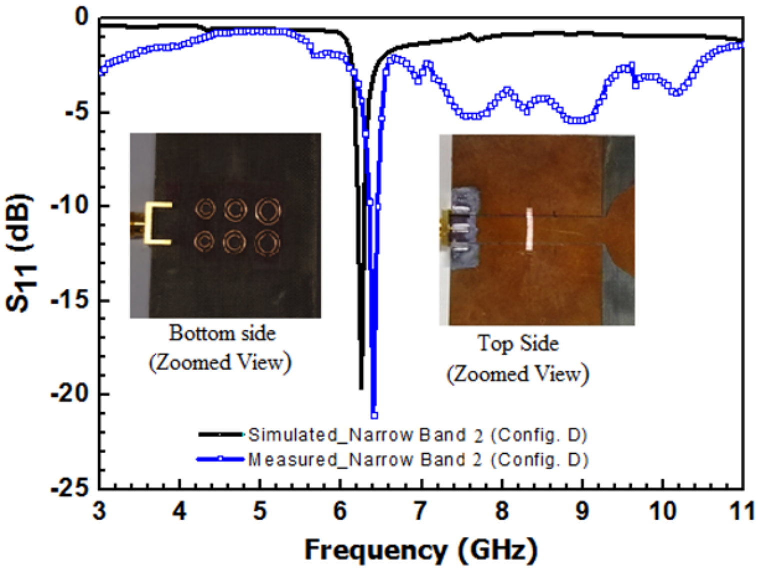

Figure 3.12: Simulated and measured S_{11} characteristics of the configuration D.

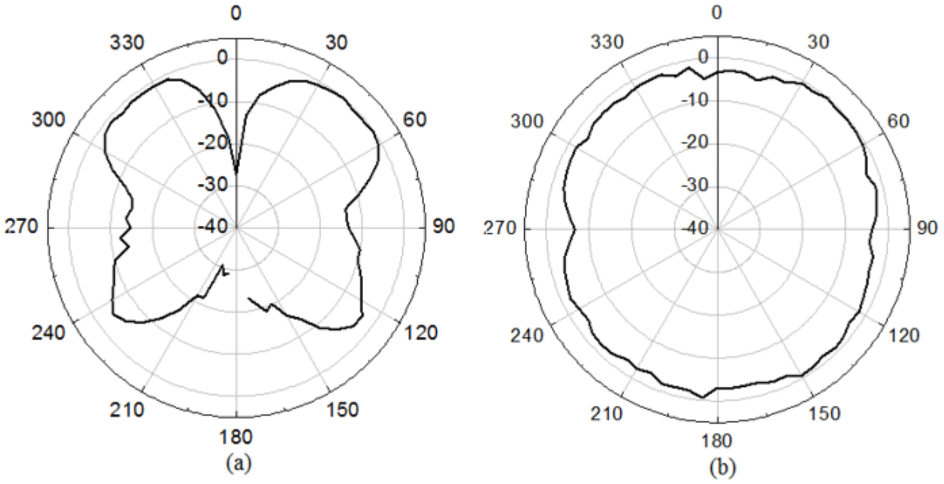

Figure 3.13: Measured normalized (a) E (x-y) and (b) H (x-z) plane co-pole radiation pattern of the narrowband antenna of configuration D.

at 6.4 GHz against 6.24 GHz for simulation. Figure 3.13 shows the measured normalized E and H-plane radiation pattern of the antenna.

Configuration E is similar to previous two narrowband configurations (Configurations C and D) exhibiting similar impedance and radiation characteristics with measured resonance frequency at 8.04 GHz and consistent radiation pattern as

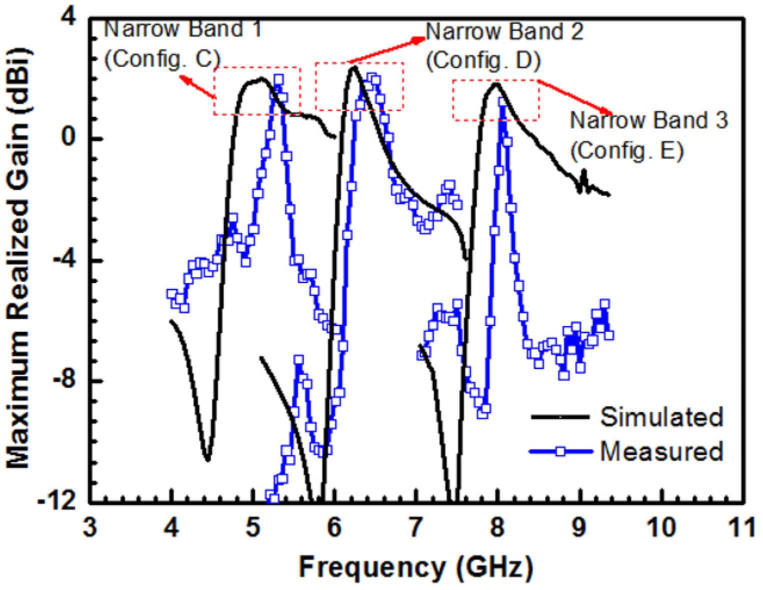

Figure 3.14: Simulated and measured maximum realized gain (x-y plane) characteristics of the proposed narrowband antennas (Configuration C, D and E).

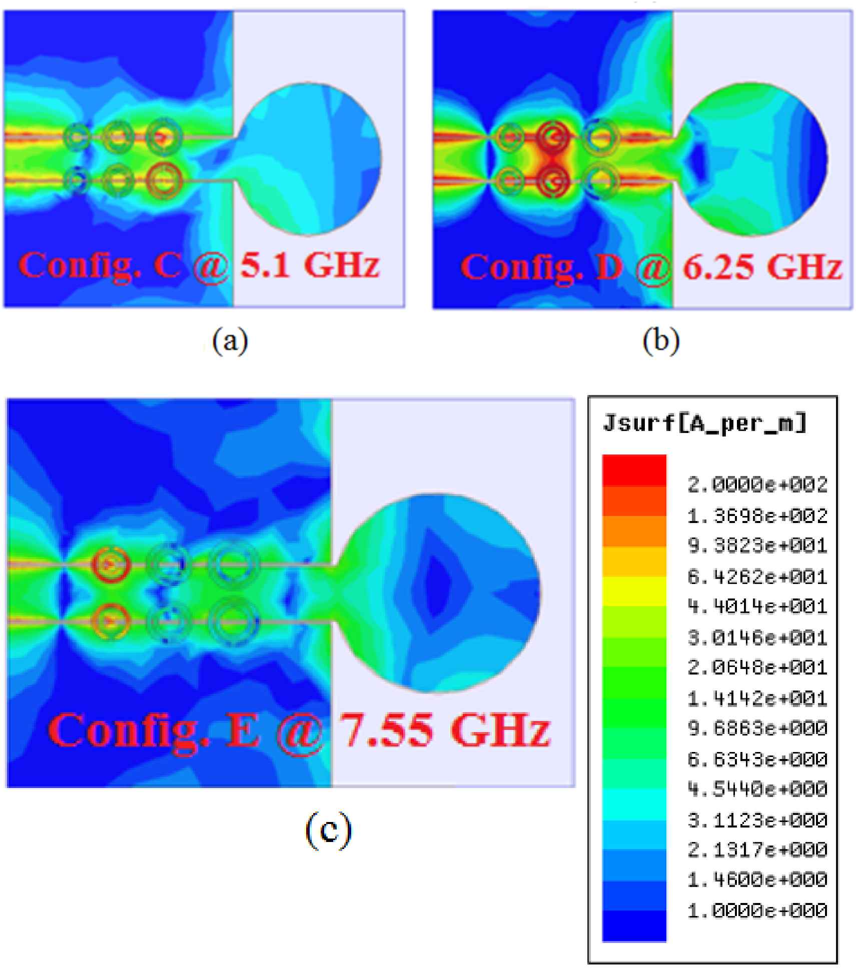

Figure 3.15: Simulated surface current distribution of the CPW fed CMPA loaded with circular SRRs with rotated inner rings, with copper strips (a) Configuration C at 5.1 GHz, (b) Configuration D at 6.25 GHz and (c) Configuration C at 7.87 GHz.

that of previous narrow band configurations. The measured and simulated maximum realized gain versus frequency plots for all three narrowband configurations (Configurations C, D and E) are shown in Figure 3.14. The figure confirms narrowband responses having a peak measured gain of 2.08 dBi, 2.10 dBi and 1.43 dBi at 5.29 GHz, 6.45 GHz and 8.04 GHz with rapidly decreasing gain at either sides of the resonance frequencies.

Figure 3.15 shows the simulated surface current distribution of the proposed narrowband antenna (configuration C, D and E) which clearly indicates the excitation of the antenna at the narrowband frequency. Figure 3.16 shows the simulated poynting vector along the feed line of the antenna. This plot reveals that all the

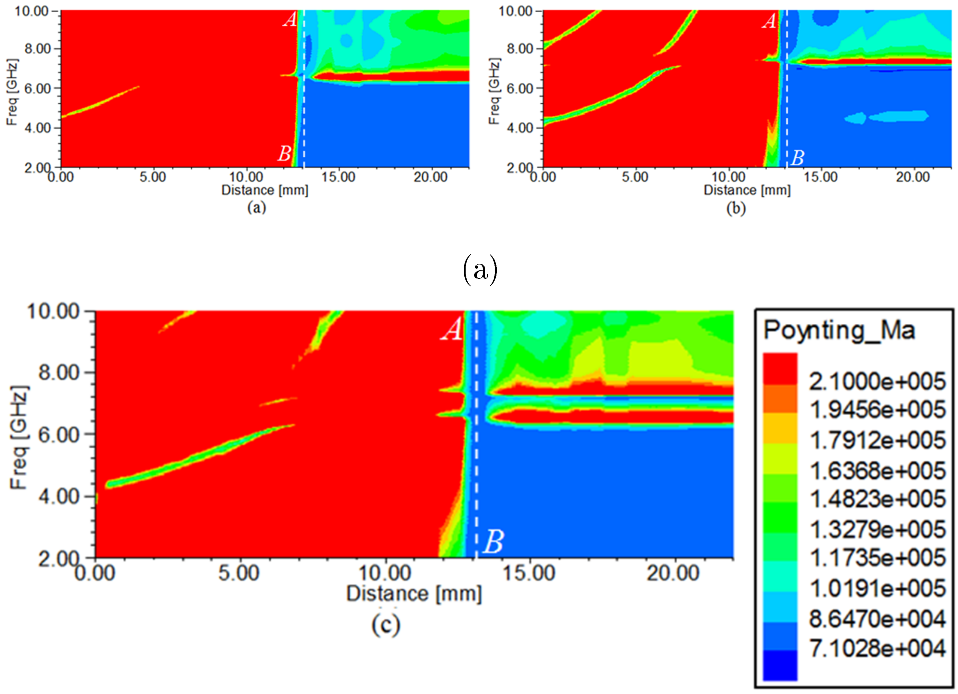

(a)

(b)

Figure 3.16: Simulated contour plots of Poynting vectors of the propagating electromagnetic energy through the longitudinal dimension of one of the slots as a function of frequency for narrow band antenna.

frequencies propagating till the SRR and shunt strip location (indicated by red colour) and beyond that point only one frequency corresponding to the SRR propagates and reaches the antenna (red colour) where it is radiated, others are not propagating. This shows the filtering function performed by the feed section of the antenna comprising of SRR and shunt strip.

The proposed antenna configurations investigated in this work are summarized in the block diagram as shown in figure 3.17, clearly demonstrating four configurations (configurations B, C, D and E) that evolved from the fundamental UWB monopole (configuration A) by simple combinational loading of SRR and copper strips.

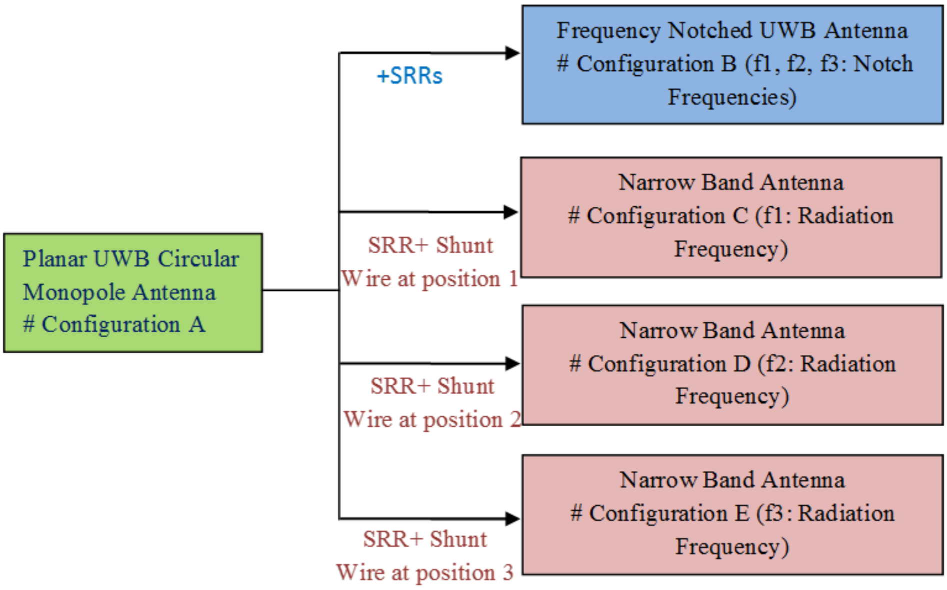

Figure 3.17: Block diagram of the proposed antenna configurations invoking various antenna performances using different combinational loading of SRRs and shunt strip on the feed section of the printed CMPA

3.2.2 Tapered Slot Antenna Based Multi-Functional Antenna

In section 3.2.1, multi-functional antenna response is demonstrated in a circular monopole antenna using combinational loading of the SRRs and/or copper switches in the feed region of the antenna. One of the unique features of this technique, as was mentioned previously, is radiator independent design concept. To be more precise, proposed idea should work on any CPW fed planar UWB antennas. In this section, we validate this claim by using a CPW fed tapered slot antenna (TSA) for exhibiting the proposed multi-functionality. Here, a single printed TSA loaded with SRR and shunt strip on the feed section provides the multiple antenna functionality. The frequency notch in the wideband printed TSA is caused by the SRRs which are magnetically coupled with feeding CPW line and inhibit signal propagation around the SRR's resonance frequency. With the loading of shunt strip, the frequency notched wideband antenna can be reconfigured into a narrowband antenna operating at the notch frequency. Moreover, the notch frequency and the narrowband frequency can be tuned by changing the physical dimension of the SRR geometry without altering the design parameters of the antenna.

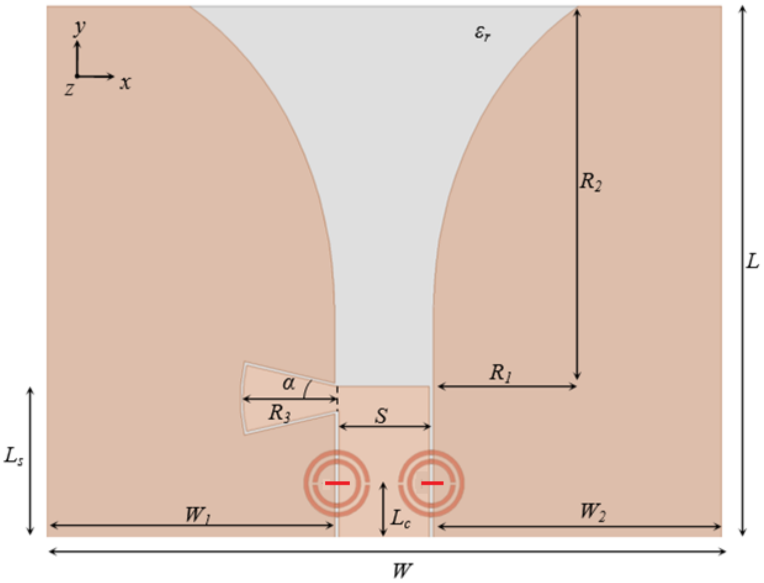

Figure 3.18: Schematic of a CPW fed printed tapered slot antenna loaded with circular SRR. Top view with a pair of SRRs (in darker shade) loaded on the back side, along with shunt strip shown in red colour.

Figure 3.18 shows a schematic of the proposed antenna. The antenna consists of the CPW feed line transformed into a slot line which is tapered exponentially along the length of the slot. To enhance the transition bandwidth covering the UWB band, a radial stub is employed on the CPW signal line extended towards the ground planes [Garg et al. (2013); Simons (2001)]. The radiator utilizes elliptical tapered profile to make a smooth transition. The antenna is fed by a CPW having ground plane widths W_1, W_2 and length L_s, a signal line having width S and length L_s. The transition consists of a radial stub with radius R_3 and angle α. The radiator has an elliptical tapering profile with R_1 and R_2 as its major and minor axis. The antenna is printed on a substrate having dielectric constant ϵ_r and thickness h. A pair of a circular shaped SRR is printed on the backside of the substrate with their center coinciding with the slot gaps to maximize the magnetic coupling. The SRR consists of two concentric rings of external radius r_{ext}, width c, separated by d and having splits of dimension g, placed in diametrically opposite side. A pair of shunt strips are placed on the slots of the CPW with their positions coinciding with the axes passing through the center of the SRRs.

The proposed antenna is modelled on Rogers RT Duriod 5870 substrate having dielectric constant $\epsilon_r = 2.33$, tan $\delta = 0.0012$ and thickness $h = 1.575$ mm. The antenna parameters are given as $L = 35$ mm, $W = 45$ mm, $L_s = 10$ mm $W_1 = W_2 = 38.4$ mm, $S = 6$ mm, $s_g = 0.3$ mm, $R_1 = 9.67$ mm, $R_2 = 25$ mm, $R_3 = 6.1$ mm and $\alpha = 13^o$.The SRR dimensions are given as: $r_{ext} = 2.2$ mm, $c = 0.3$ mm, $d = 0.3$ mm and $g = 0.2$ mm. A pair of shunt strips were placed on the slots between the ground planes and the signal line and aligned to the position of SRRs axes. The antenna is simulated in a finite element based EM solver [ANSYS (2015)]. As discussed in Section 2.5, the transmission line loaded with SRR can be validated with the help of lumped equivalent circuit. The lumped element based equivalent circuit of figure 3.19, corresponding to two cases (without and with shunt strips) are simulated using ADS circuit simulator [Agilent (2015)]. The equivalent circuit parameters for these configurations are: $L_{SRR} = 7.51$ nH, $C_{SRR} = 63.04$ fF, $L_p = 118$ nH (shunt strip loaded case). The circuit parameters for the host CPW medium for unit cell size of $p = 5$ mm are $L = p * L_{pul}$, $C = p * C_{pul}$ where $L_{pul} = 261.16$ nH and $C_{pul} = 63.29$ pF. The coefficient of coupling between the host CPW and SRR pair is $k = 0.25$. The input port is terminated with a 100 Ω matched load while output port impedance is taken as double the input impedance of the TSA without any loading, over the UWB frequency range obtained from electromagnetic simulation.

Figure 3.20 shows the simulated S_{11} of the prototype antenna with and with-

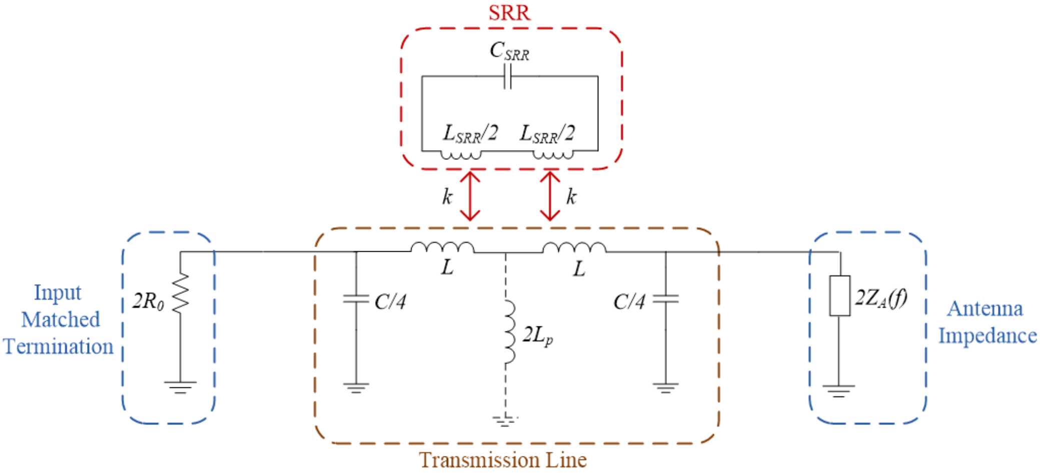

Figure 3.19: Lumped element equivalent model of the proposed CPW fed tapered slot antenna. In Diode OFF condition, L_p is not present, during ON condition it is modelled with shunt L_p

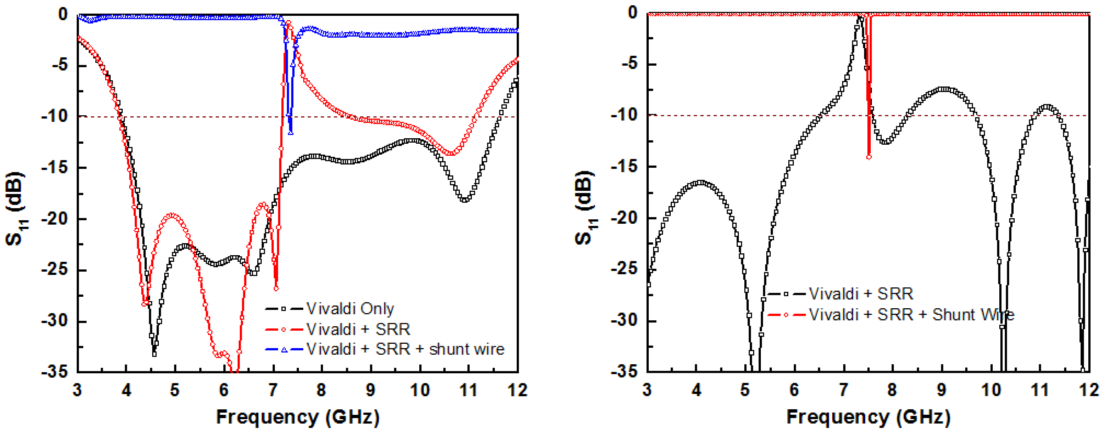

(a) (b)

Figure 3.20: Simulated S_{11} characteristics of the proposed SRR coupled, shunt strip loaded CPW fed tapered slot antenna

out the SRR loading. Without the SRR loading, the antenna exhibits an ultra-wideband characteristic from 4 GHz to 11.7 GHz providing a wideband response. With only SRR loading, the antenna yields an ultra-wideband notched response with notch centered at 7.3 GHz due to the SRR resonance frequency. The notch frequency can be controlled by changing the SRR dimensions. However, with the shunt strip in position, the filtenna yields a narrowband response centered at 7.35 GHz and effectively complements the impedance behavior of the filtenna with only SRR loading. The lumped-element based equivalent circuit simulated S_{11} charac-

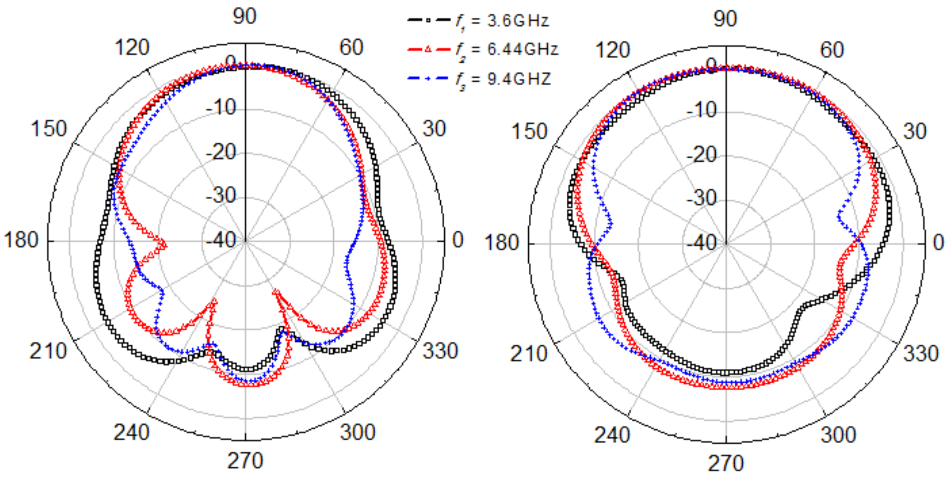

Figure 3.21: Simulated normalized (a) E (x-y) and (b) H (y-z) plane co-pole radiation pattern of the CPW fed TSA at three different frequencies.

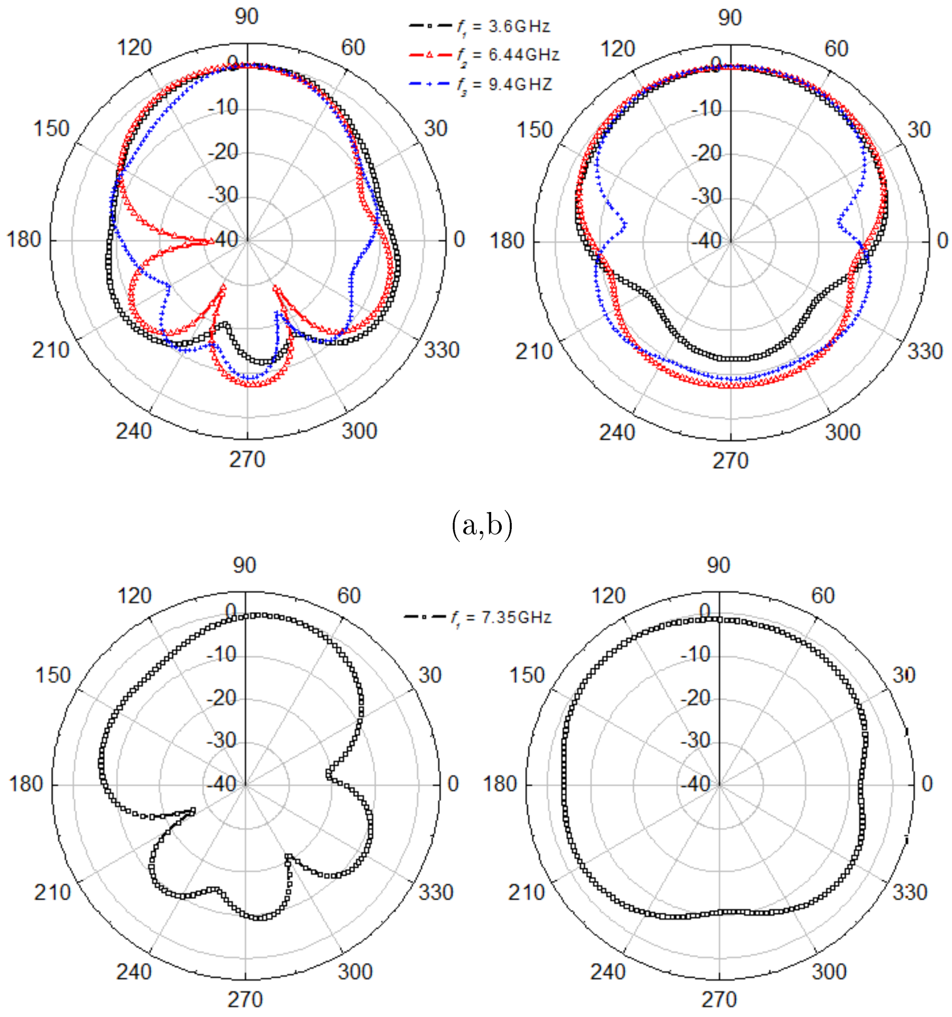

(a,b)

(c,d)

Figure 3.22: Simulated normalized (a), (c) E (x-y) and (b), (d) H (y-z) plane co-pole radiation pattern of the SRR coupled and shunt strip loaded CPW fed TSA. (a), (b) represent only SRR loading and (c), (d) represent both SRR and shunt strip loading.

teristics is shown in figure 3.20(b). With only SRR loaded to feed region (L_p in figure 3.19 disconnected), represented by black curve, a notch is observed at 7.35 GHz. While with SRR loaded to feed along with the shunt wire (L_p connected) represented by red curve, a narrowband response is observed at 7.5 GHz.

The radiation pattern of the CPW fed TSA at three different frequencies is shown in figure 3.21. The pattern exhibits end-fire radiation capability throughout the frequency range. The E-plane(x-y plane) pattern exhibits a narrow HPBW when compared to the H-plane (y-z plane), which is reasonably in accordance with the property of tapered slot antennas. The radiation pattern of the CPW fed SRR loaded TSA is shown in figure 3.22(a) and (b) for same three set of frequencies. This pattern exhibits an end-fire radiation pattern implying minimal impact of the SRRs on the radiation pattern of the antenna over its entire impedance bandwidth excepting the notch frequency. The radiation pattern of the CPW fed SRR and shunt strip loaded TSA is shown in figure 3.22(c) and (d) at the narrowband frequency. This pattern indicates the endfire pattern in both E and H-planes, thereby preserving the radiation pattern of the TSA. The gain versus frequency plot of the antenna configuration with and without SRR loading is plotted in figure 3.23, for two frequencies. At non-notch or radiating frequency, the gain characteristics of both the antennas are similar indicating unperturbed radiation pattern. At notch frequency, the gain of unloaded TSA is positive, gain of SRR loaded TSA is negative and thus leading to gain reduction of around 9dB. The gain versus frequency plot of the antenna configuration is plotted in figure 3.24. For the antenna without any loading the gain is positive throughout the entire frequency range. With SRR loading, the gain drops to -3.8 dBi at the notch frequency while with shunt strip loading the gain is positive in the narrowband region as indicated with blue curve.

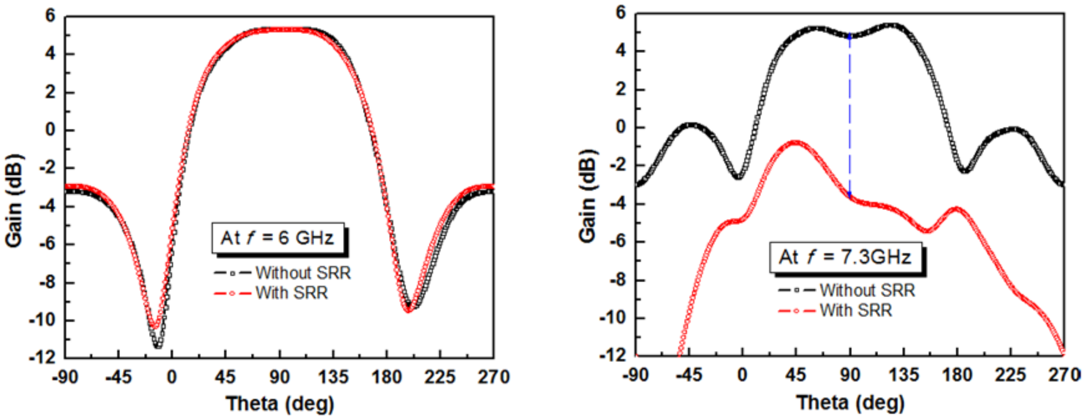

Figure 3.23: Simulated gain characteristics of TSA with and without SRR loading at (a) non-notch frequency (b) at notch frequency.

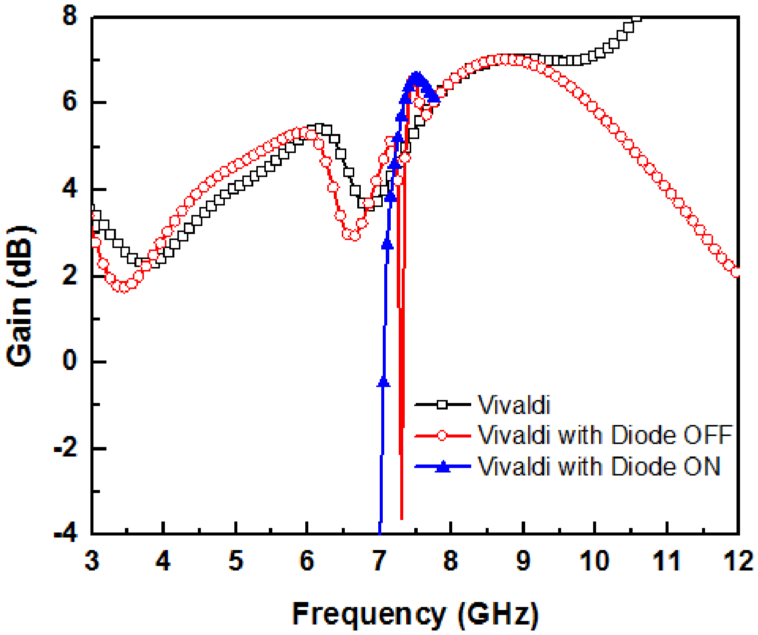

Figure 3.24: Simulated gain characteristics of the proposed SRR coupled and PIN diode loaded CPW fed TSA with diode in OFF and ON state.

3.3 Multilayered Stacked Multi-Functional Antenna

In order to provide the multi-notch applications using the technique discussed in previous section, multiple resonators of various sizes should be incorporated along the feed line of the radiator. Due to varying size of the resonators incorporated along the feed-line, various resonance frequencies are obtained which in turn provide multi-notched performance. Though this technique is very simple and easily adoptable for any type of CPW-fed UWB radiators, it increases the foot-print of the antenna. In certain applications, where over-all dimension is constrained, this design concept might not be suited. To mitigate this limitation of enhanced feed-length of the resultant structure, we introduce multilayered design, where a superstrate of suitable dimension is loaded above the substrate in the feed region of the antenna. Due to this, in this scheme, the CPW feed line is sandwiched between the conventional substrate and newly introduced superstrate. This configuration provides two different layers for placing the SRRs and thereby effectively reduces the feed length to almost half of the earlier configuration where only one layer (below substrate) was available for SRR placement. This idea is exploited in current work as detailed below.

3.3.1 Antenna Design and Configuration

The multilayered multi-configuration antenna is evolved from an annular ring monopole antenna (ARMA) fed by a CPW based transmission line printed on a dielectric substrate, offering the opposite side of the printed copper to accommodate passive components/active devices for various applications. Basic operation principle of an ARMA is same as that of printed circular monopole. The ARMA is suitably improvised with various kind of SRR and/or switches loading to obtain multiple antenna configurations.The multiple configurations of the proposed antenna are systematically illustrated in figure 3.25 and 3.26. Basic CPW fed ARMA, named as configuration A, shown in figure 3.26(a), is loaded with various combinations of SRRs of varying size and/or copper strips to derive six new antenna configurations (configurations B, C, D, E, F and G) providing multiple antenna functionality. These configurations are clearly illustrated in figure 3.26(b)-(g).

Basic UWB performance is provided by the configuration A, which acts as the fundamental building block to realize other multiple antenna configurations. As shown in figure 3.25 and 3.26(a), configuration A consists of an annular ring of outer and inner radii R_1, and R_2, respectively, printed on a RT duroid ($\epsilon_{r1} = 2.33$, tan $\delta = 0.0012$) substrate. It is excited by a CPW feed consisting of ground planes having width W_1, W_2, length L_s and signal line having width S and length, L_s. The widths of the slots between the ground planes and signal line, s_g and signal line width S, are chosen to ensure broadband (2-12 GHz) impedance (50 Ω) matching with the commercial connector. The annular ring is placed at a distance t from the feed section to attain UWB characteristics. The detailed dimensions of this configuration are indicated in Table 3.2.

Frequency notched configurations (configurations B, C and D) are derived from previous fundamental configuration A, by loading a pair of SRRs, i) beneath the slot lines of feeding CPW (configuration B) or ii) on the superstrate placed on the feed section of the CPW or iii) by both (i) and (ii) (configuration D), clearly indicated in Fig. 3.26(b)-(d). Figure 3.25(a) shows the geometrical layout of configuration B where a pair of square SRR of outer side dimension, $2 * a_{ext1}$, width, c_1, inter-ring spacing, d_1 and split gaps g_1 are precisely printed with centres

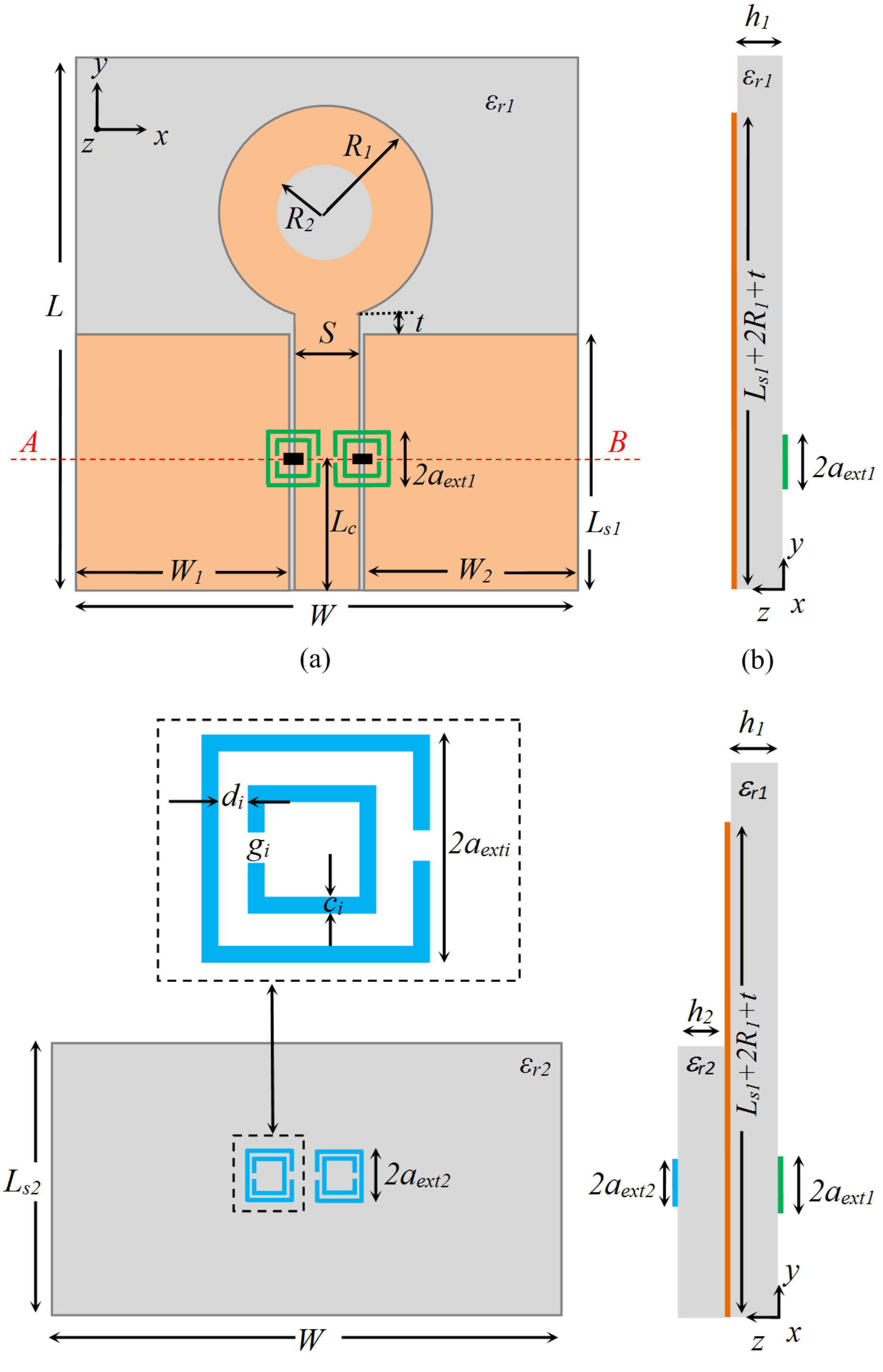

(a) (b) (c) (d)

Figure 3.25: (a) Geometrical Layout of a CPW fed ARMA loaded with SRR (b) cross sectional view of the configuration with printed SRRs and CPW fed monopole antenna on either sides of the substrate (c) superstrate with SRR loading (d) cross sectional view showing the loading of superstrate on antenna. Zoomed version of unit cell of SRR is indicated in dotted box.

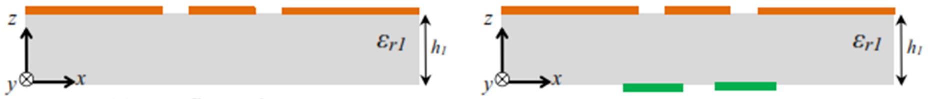

(a) Configuration A (b) Configuration B

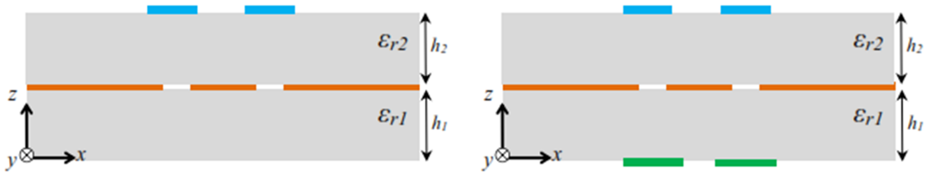

(c) Configuration C (d) Configuration D

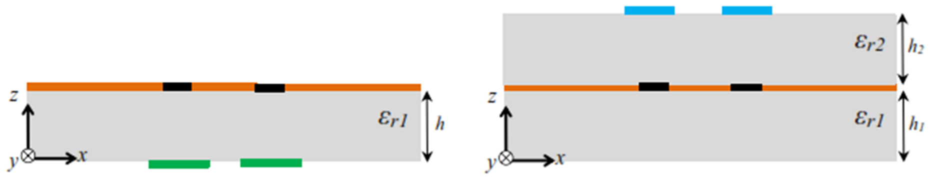

(e) Configuration E (f) Configuration F

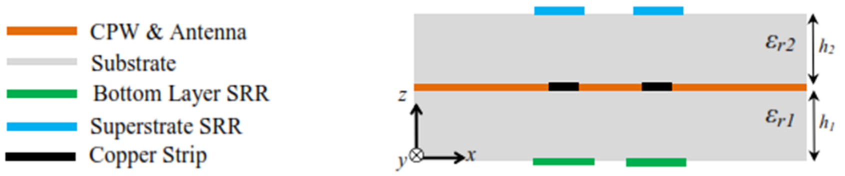

(g) Configuration G

Figure 3.26: Simulated gain characteristics of the proposed SRR coupled and PIN diode loaded CPW fed tapered slot antenna with diode in OFF and ON state.

of SRRs matching with centre of the slot lines of the CPW at a distance L_c from the feed port of the antenna. Configuration C is realized by similar SRR loading on a superstrate of over-all dimensions, as shown in Table 3.2, loaded above feed section of the basic antenna configuration A. The superstrate printed with

Table 3.2: Design paramters of the square SRRs loaded multilayered ARMA printed on a dielectric substrate having $\epsilon_r = 2.33$, tan $\delta = 0.0012$. Superstrate layer material is same as the substrate. (Parametric variables as shown in figure 3.25)

Design Parameters	L	W	R_1	R_2	W_1	L_{s1}	S
Dimensions (in mm)	50	50	12.5	5	22	22	5
Design Parameters	W_2	S_g	t	h_1	L_c	h_2	L_{s2}
Dimensions (in mm)	22	0.5	0.2	1.575	13	1.575	12

SRRs is placed at the appropriate position and fixed with dielectric tape. Since the loaded superstrate has same dielectric constant as that of antennas substrate ($\epsilon_{r2} = \epsilon_{r1} = 2.33$) and it is located in feed region, it has very less impact on the impedance and radiation characteristics of the antenna. The SRRs pair loaded on the superstrate as shown in figure 3.25(c) has dimension a_{ext2}, width, c_2, inter ring spacing, d_2 and split gaps g_2. The SRR dimensions utilized for configuration B, C and D are summarized in Table 3.3. The different dimensions of the SRR pairs for configuration B and C excites different resonance frequencies f_1 and f_2 respectively [Siddiqui et al. (2014)] which results different notch frequencies in the UWB spectrum. Configuration D is a multilayered structure in the feed section of the antenna as it has SRRs printed beneath the substrate as well as on the superstrate.

This multiple SRR pairs with dimensions summarized in Table 3.3, correspond to two different resonances within the UWB spectrum and thereby provides dual notched UWB response with frequency notches at f_1 and f_2. The narrowband configurations (configurations E, F and G) are aimed to obtain complementary antenna functionality compared to frequency notched UWB configurations of B, C and D. Combinational loading of the SRR and copper strips, shorting the CPW signal with ground planes, forms a narrow band pass filter [Siddiqui et al. (2015)] around SRR's resonance frequency which in turn excites the ARMA over corre-

Table 3.3: Design paramters of the square SRRs loaded beneatht the substrate ($\epsilon_r = 2.33$, tan $\delta = 0.0012$) and/or above the superstrate ($\epsilon_r = 2.33$, tan $\delta = 0.0012$) (Parametric variables as shown in figure 3.25)

Design Paramters	**Dimensions (mm)**	
	Pair 1 (i = 1) (beneath substrate)	**Pair 2 (i = 2) (on the superstrate)**
a_{exti}	2.5	2.1
c_i	0.5	0.5
d_i	0.6	0.3
g_i	0.4	0.5

sponding passband frequency. This transforms the previous frequency notched UWB antennas (configuration B, C and D) into narrowband antennas (configuration E, F and G, demonstrated in figure 3.26(e)-(g)) providing a complementary impedance profile. This particular complementary antenna response evolves from a previously reported article [Siddiqui et al. (2015)] and has been exploited to achieve multiple narrow band antenna functionalities at f_1, f_2 and (f_1, f_2). The narrow band operation is highly sensitive to the position of copper strips and provides best excitation when centre of the strips is aligned with centre of the SRRs of the other side. This is clearly indicated in figure 3.25(a) with centre of the

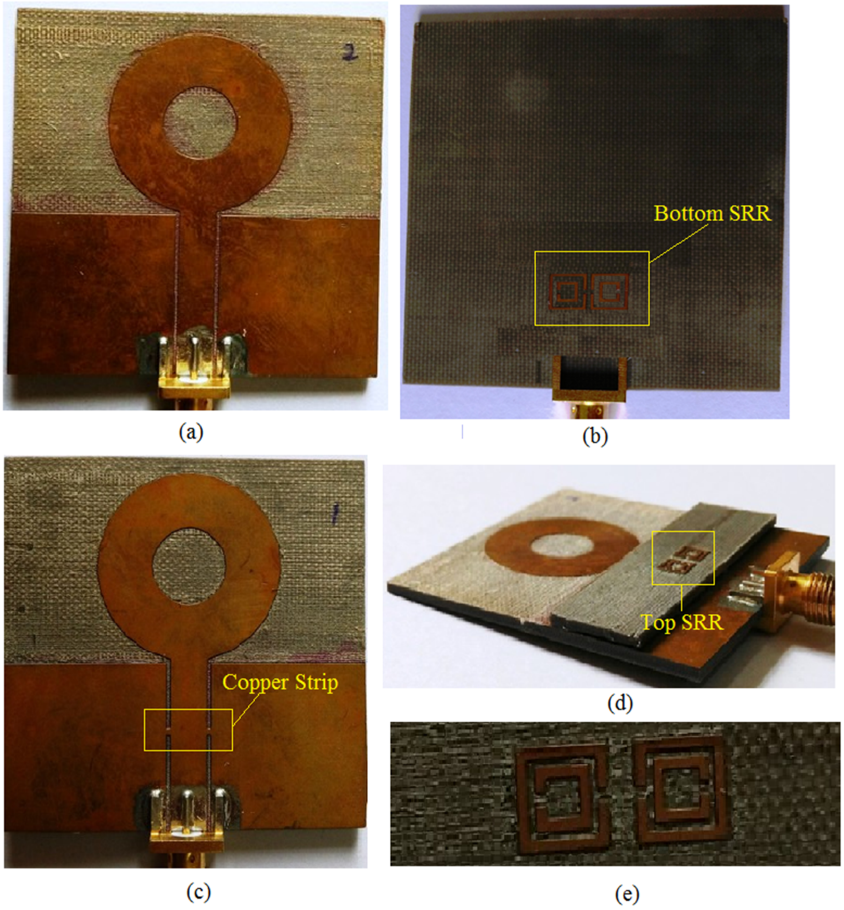

Figure 3.27: Fabricated prototype of the CPW fed annular ring monopole antenna loaded with square SRR (a) Top View (Configuration A to D) (b) Bottom View (Configuration B, D, E, and G). (c) Top view (Configuration E to G) obtained by loading copper strip on the CPW signal line (d) Isometric view showing the superstrate loading for configuration C, D, F, and G (e) Zoomed view of the printed SRR

shunt strips located at a distance of L_c from the feed port of the antenna.

The fabricated prototype consisting of slotted circular monopole antenna without SRR loading, with SRR loading and shunt strip loading is shown in figure 3.27(a), (b) and(c). The placement of the superstrate on the antenna is shown in figure 3.27 (d) and 3.27 (e) showing the SRR printed on the superstrate. Three prototype antennas, i) only ARMA without any loading, ii) ARMA with a pair of SRR printed on the backside of the CPW feed section and iii) ARMA with a pair of SRR printed on the backside of the CPW feed section and copper strips shorting the signal line of the CPW with the ground planes, are designed and simulated using a commercial electromagnetic simulator [ANSYS (2015)]. These antennas along with a superstrate layer with a pair of SRRs printed on it, is loaded above the feed section of the CPW signal line and constitutes various antenna configurations with multiple antenna functionality. Each of these combinations provides unique reflection coefficient response measured using an Agilent PNA-X N5224A network analyzer. For all the antenna prototypes radiation pattern measurement was carried out in a fully calibrated near field anechoic chamber as shown in figure 3.28. A broadband pre-amplifier (Agilent 83051 A) coupled broadband horn was used as the transmitting antenna while the SRR/copper-strips loaded ARMA with and without superstrate loading was in receive mode for various configurations.

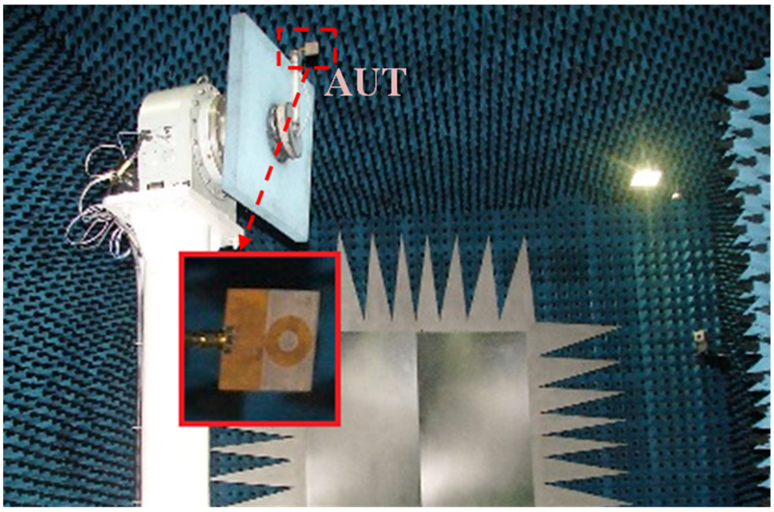

Figure 3.28: Radiation pattern measurement setup for fabricated CPW fed ARMA for various configurations in the anechoic chamber with cables and transmitting antenna.

3.3.2 Simulation and Measurement Results

The measured and simulated plots for the S_{11} versus frequency of the proposed ARMA, Configuration A, is shown in figure 3.29(a). Figure 3.29(b) compares the measured maximum realized gain in the x-y plane against that of simulated. As revealed from the figure 3.29, the simple CPW fed ARMA operates over the entire UWB spectrum (3.1 to 10.6 GHz) with resonance dip around 3.6 GHz (corresponding to the quarter wavelength resonance of the disc diameter) with

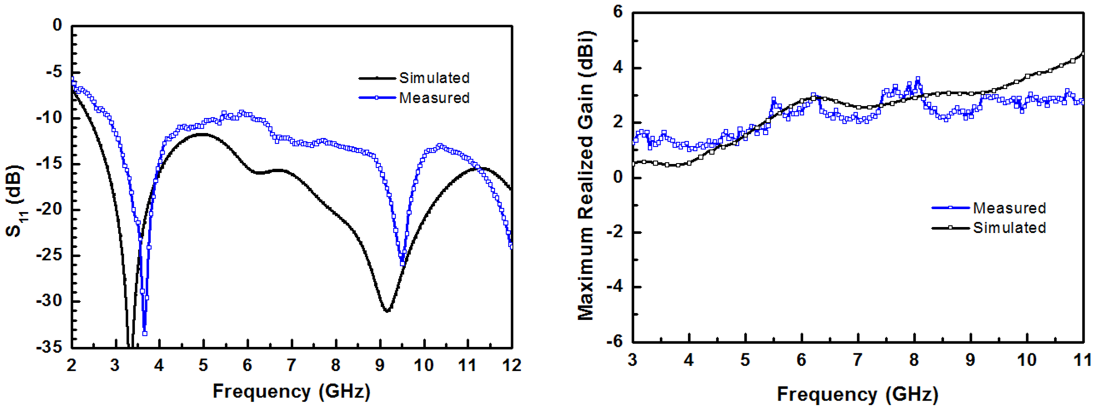

(a) (b)

Figure 3.29: Simulated and measured S_{11} and maximum realized gain characteristics of the proposed CPW fed ARMA for UWB response (configuration A).

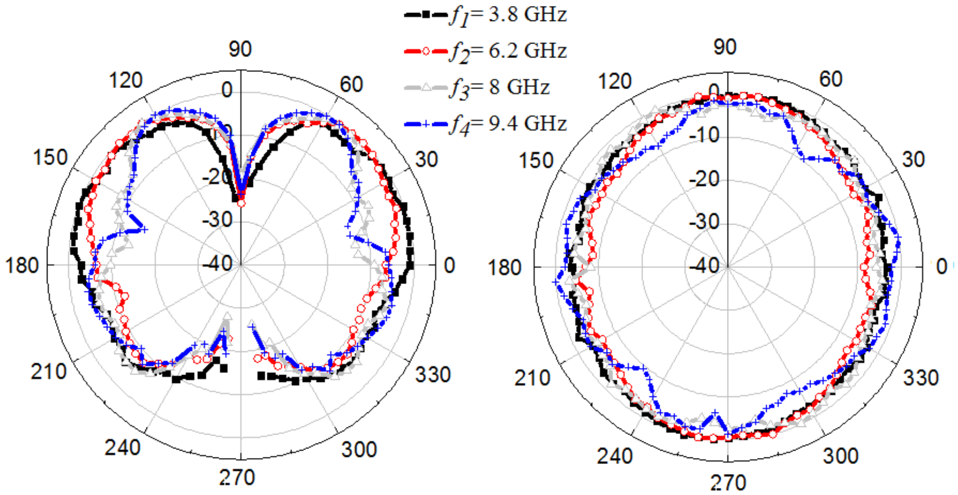

Figure 3.30: Measured normalized (a) E (x-y) and (b) H (x-z) plane co-pole radiation pattern of the CPW fed ARMA (configuration A).

consistent flat gain profile over the band. The measured radiation pattern as shown in figure 3.30 exhibits monopole type omni-directionality with axial null (along y axis) in E-plane and circularly symmetric H-plane (x-z plane) with acceptable co to cross polar separation over the entire bandwidth.

Figure 3.31 plots the simulated and measured S_{11} versus frequency of the pro-

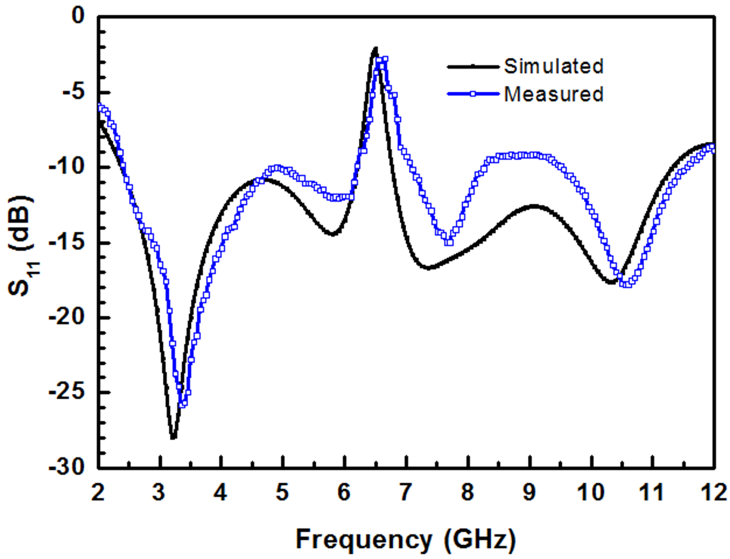

Figure 3.31: Simulated and measured S_{11} characteristics of the proposed CPW fed ARMA loaded with square SRR beneath the substrate for single notched UWB response (configuration B)

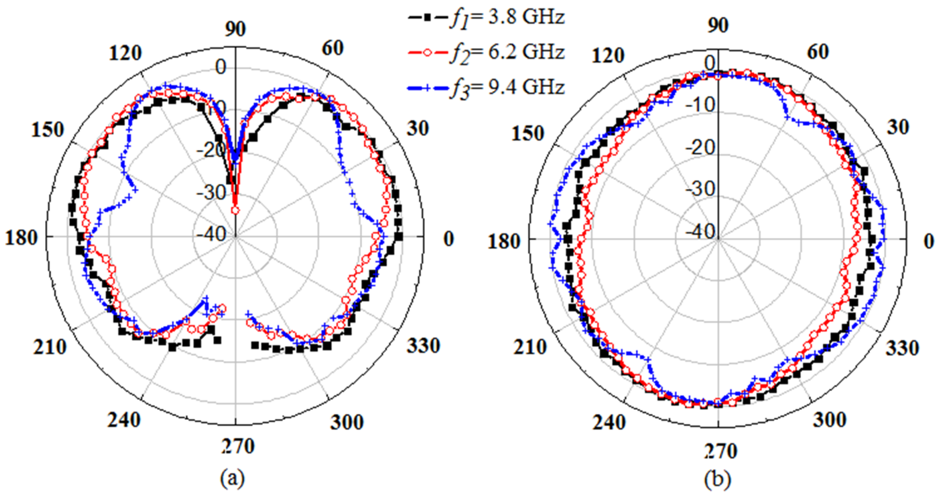

(a)

(b)

Figure 3.32: Measured normalized (a) E (x-y) and (b) H (x-z) plane co-pole radiation pattern of the CPW fed ARMA loaded with square SRR beneath the substrate for single notched UWB response (configuration B).

posed antenna configuration B. As discussed previously, the SRRs loaded beneath the CPW slots and thereby getting magnetically coupled with the propagating electromagnetic signal, inhibit propagation around its resonance frequency. This contributes to the measured frequency notch at 6.61 GHz against 6.51 GHz for simulated notch. Figure 3.32 shows the E and H-planes measured normalized radiation patterns of the proposed antenna configuration B at 3.8 GHz, 6.2 GHz and 9.4 GHz exhibiting monopole type radiation pattern with axial null for E-plane and nearly omni-directional pattern for H-planes. The selected frequencies spans over the entire UWB spectrum, excluding the notch frequency where there is no effective radiation from the antenna.

The measured and simulated maximum realized gain values versus frequency of the proposed SRR loaded antenna of configuration B, plotted in figure 3.33, exhibits drastically reduced gain of -3.65 dBi at 6.61 GHz, with acceptable gain in the range of 1 to 3 dBi over the rest of the UWB spectrum reconfirming the presence of strong notch contributed by the SRRs resonance. Figure 3.34 shows the measured and simulated S_{11} versus frequency response of the antenna configuration C with SRRs loaded separately by printing them on a superstrate placed

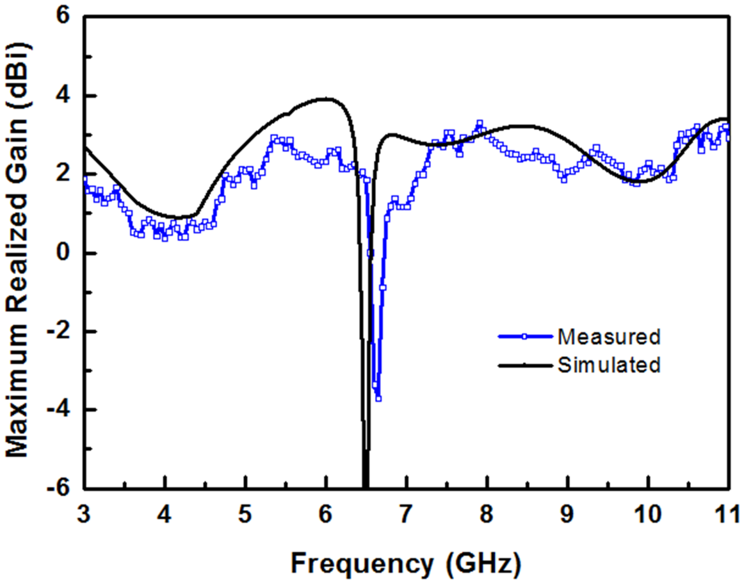

Figure 3.33: Simulated and measured maximum realized gain (x-y plane) characteristics of the proposed CPW fed ARMA loaded with square SRR beneath the substrate for single notched UWB response (configuration B).

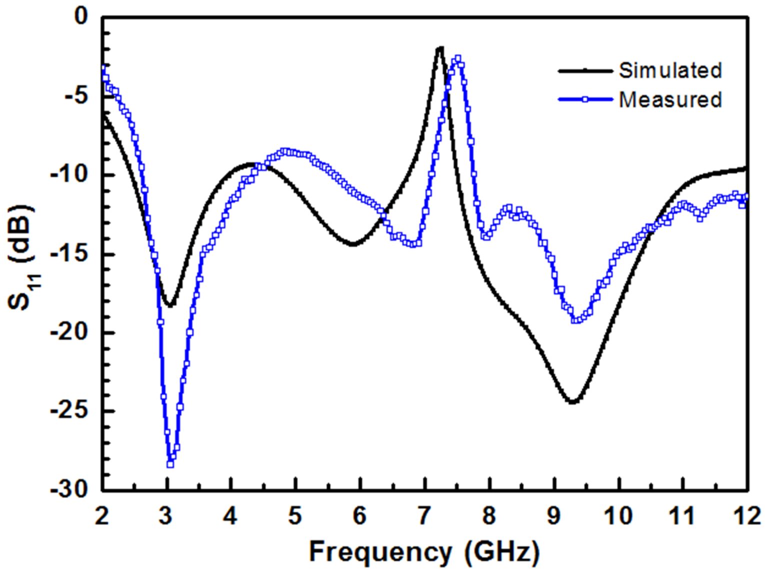

Figure 3.34: Simulated and measured S_{11} characteristics of the proposed CPW fed ARMA loaded with square SRR on the superstrate for single notched UWB response (configuration C)

on the CPW feed region of the ARMA. As revealed in figure 3.31, a measured frequency notch at 7.46 GHz is contributed due to the superstrate loaded SRR. Figure 3.35 shows the E and H-planes measured normalized radiation patterns of the proposed antenna configuration B at 3.8 GHz, 6.2 GHz and 9.4 GHz exhibiting monopole type radiation pattern with axial null for E-plane and nearly omni-directional pattern for H-planes. The selected frequencies spans over the entire UWB spectrum, excluding the notch frequency where there is no effective radiation from the antenna. The notch frequency of this configuration can be easily controlled by judiciously selecting the SRRs geometrical parameter printed on the superstrate. This enables the same antenna to be used for variable notch frequency applications by replacing the superstrate layer with different SRRs dimension. Figure 3.36 shows such mechanical tuning of the notch frequency by varying half-side-length, a_{ext}, of the SRR. It demonstrates smoothly tuned frequency notches in the range of 6.5-8.2 GHz with a_{ext} varying from 1.9 mm to 2.2 mm.

When the basic antenna configuration A is loaded with SRRs beneath the substrate and above the superstrate it results into dual notched UWB configuration D. As revealed in the S_{11} versus frequency plot of figure 3.37, two distinct

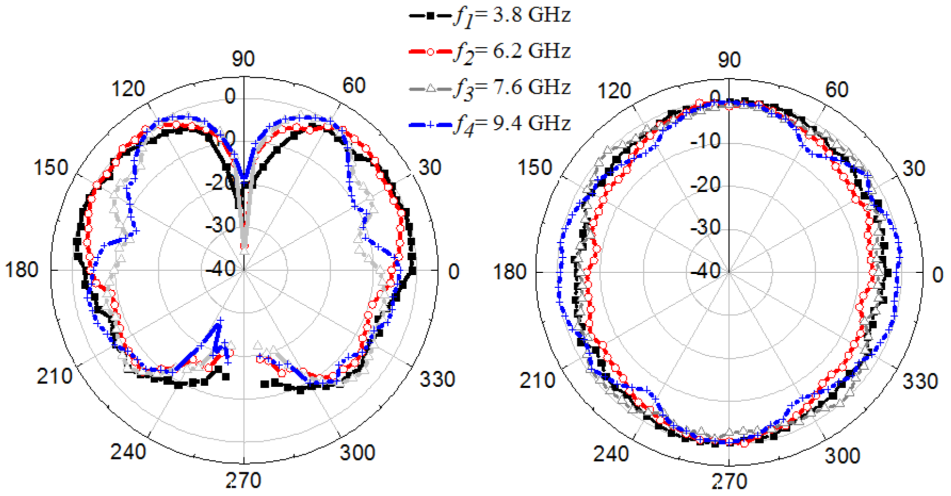

Figure 3.35: Measured normalized (a) E (x-y) and (b) H (x-z) plane co-pole radiation pattern of the CPW fed ARMA loaded with square SRR on the superstrate for single notched UWB response (configuration C).

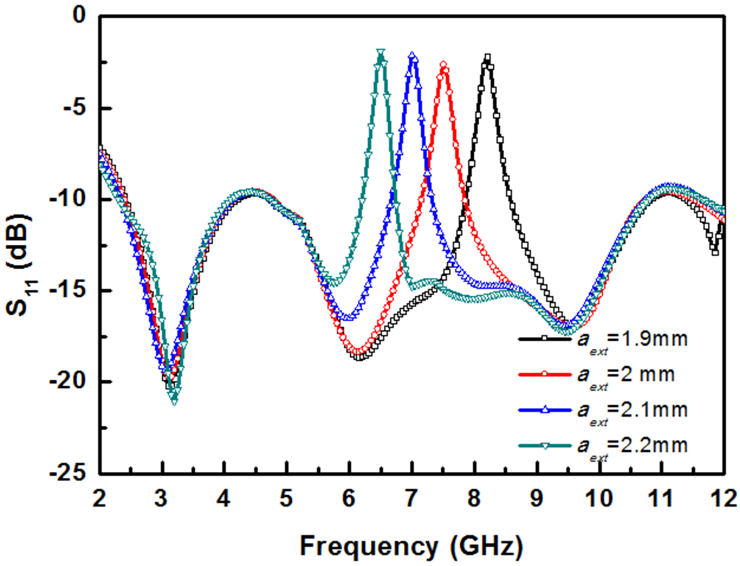

Figure 3.36: Simulated S_{11} characteristics of the proposed CPW fed ARMA loaded with square SRR on the superstrate for varying SRR dimension. c = 0.5 mm, d = 0.3 mm, g = 0.5 mm.

measured notches, at 6.6 GHz and 7.49 GHz against the simulated values of 6.47 GHz and 7.4 GHz are contributed by the each SRR pairs. Figure 3.38 shows the measured E and H-plane radiation pattern of this configuration at 3.8 GHz, 6.2 GHz and 9.4 GHz. The pattern, like previous configurations, corresponds to the

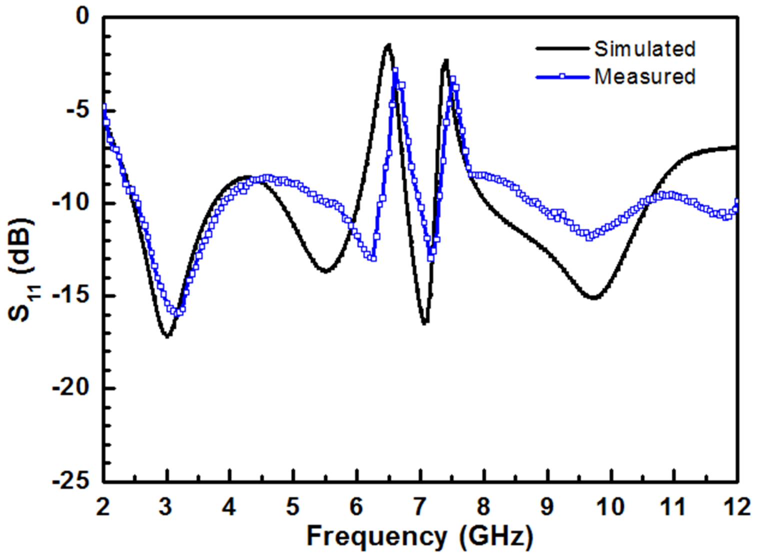

Figure 3.37: Simulated and measured S_{11} characteristics of the proposed CPW fed ARMA loaded with square SRRs beneath the substrate and on the superstrate for dual notched UWB response (configuration D).

monopole type nature even though an additional superstrate layer is loaded on the feed section of the antenna. This unperturbed radiation pattern of the fundamental monopole reconfigured for frequency notch application is due to unaffected radiation aperture of the antenna as the SRRs are loaded in the feed section of the antennas and establishes the superiority of the current technique of frequency notching.

Figure 3.39 shows the maximum realized gain of the multilayered configuration against the frequency. This antenna, like previous configurations (B and C) exhibits an acceptable flat gain over 0 dBi over the entire UWB spectrum with drastically reduced gain of -3.9 dBi and -3.75 dBi at 6.67 GHz and 7.59 GHz reconfirming the presence of the frequency notches indicated in the S_{11} plot. Figure 3.40 shows the simulated contour plots of the poynting vector along the feed length of the antenna against the frequency of operation for each of the antenna configurations B, C and D. Contour plots of figure 3.40 clearly indicates extremely low value of Pointing vector (bluish line in color version) on the right side of the line AB, at 6.4 GHz, 7.42 GHz and (6.49 GHz, 7.4 GHz) for configuration B, C and D respectively where the line AB indicates the centre position of the SRR measured from the feed port of the antenna. It is interesting to note that for each

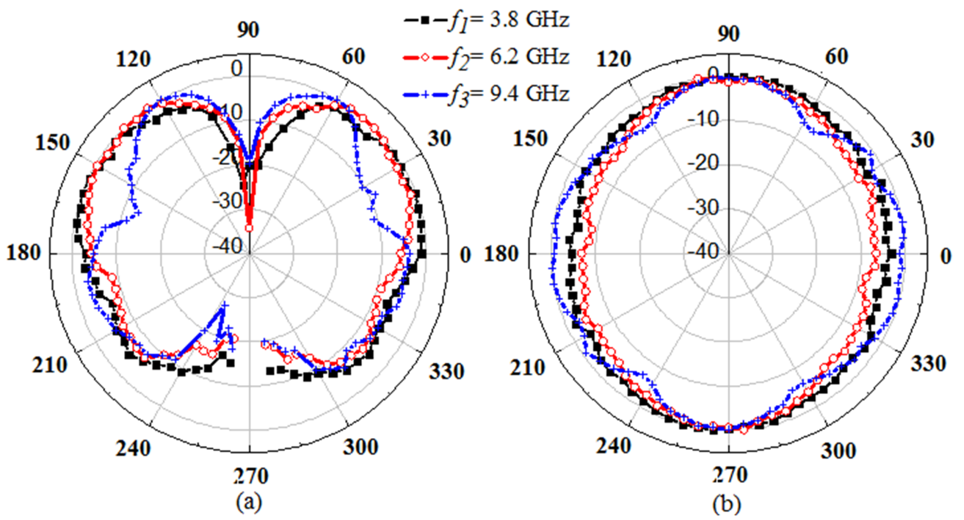

Figure 3.38: Measured normalized (a) E (x-y) and (b) H (x-z) plane co-pole radiation pattern of the dual notched UWB antenna of configuration D.

configuration the frequency notching starts around the same distance of 12 mm from the feed-end which matches with that of $(L_c - a_{exti}/2)$, starting position of SRR along the antenna and ensures the fact that the frequency notches are contributed by the SRRs. The small deviation in the measured frequency notch can

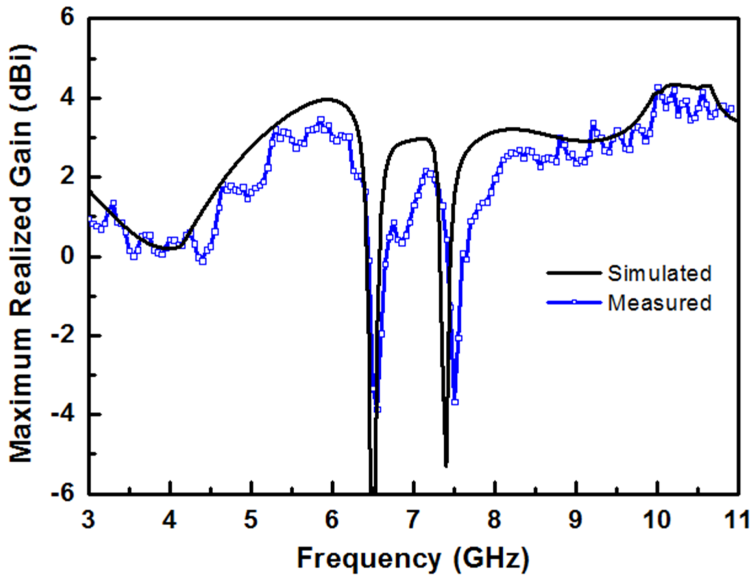

Figure 3.39: Simulated and measured maximum realized gain (x-y plane) characteristics of the proposed CPW fed ARMA loaded with square SRRs beneath the substrate and on the superstrate for dual notched UWB response (configuration D).

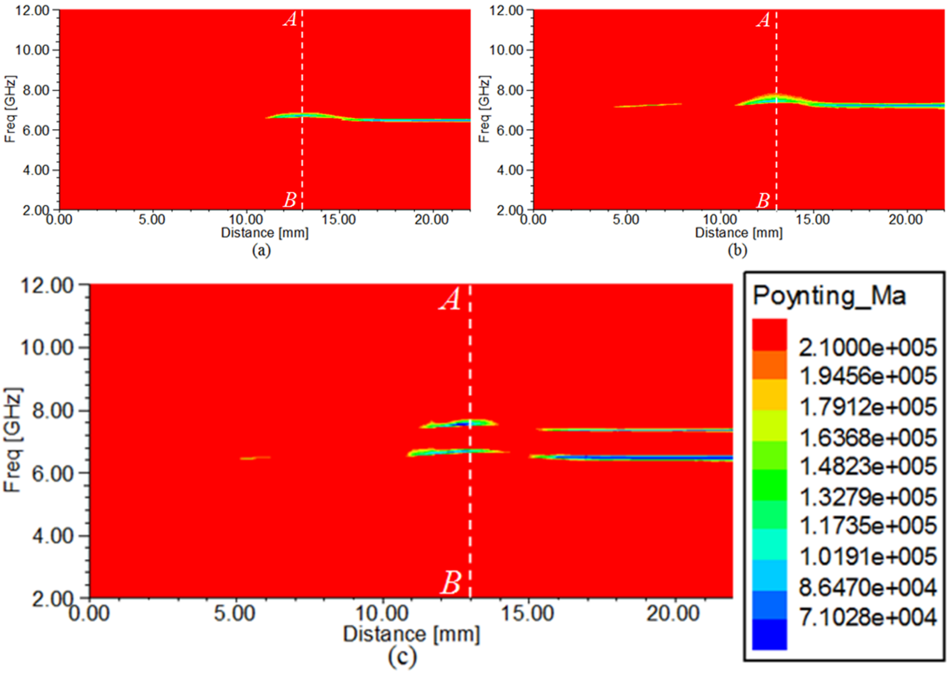

Figure 3.40: Simulated contour plots of poynting vectors of the propagating electromagnetic energy though the longitudinal dimension of one of the slots as a function of frequency (a) - (b) configuration B and C (single notched UWB antenna) indicating one notch frequency corresponding to SRR's position (c) configuration D (dual notched UWB antenna)

be attributed to the fabrication imperfection or tolerance, positional mismatch while loading the superstrate layer (for configuration C and D), effect of small air gap in the multilayered structure and effect of dielectric tape used to hold the superstrate layer on the antenna ground plane (for configuration C and D).

Figure 3.41 shows the simulated and measured plots for S_{11} and maximum realized gain versus frequency for antenna configuration E. It exhibits a narrowband response around 6.83 GHz for measured plot against 6.58 GHz for simulation. The measured maximum realized gain is 2.67 dBi at 6.77 GHz and falls drastically on both side indicating a narrow band response. The measured normalized radiation pattern of this configuration, for two principal planes is presented in figure 3.42. It shows nearly monopole type radiation pattern having axial null for E-plane and omni-directionality in H-plane.

Configuration F, realized by loading superstrate layer with SRR printed on

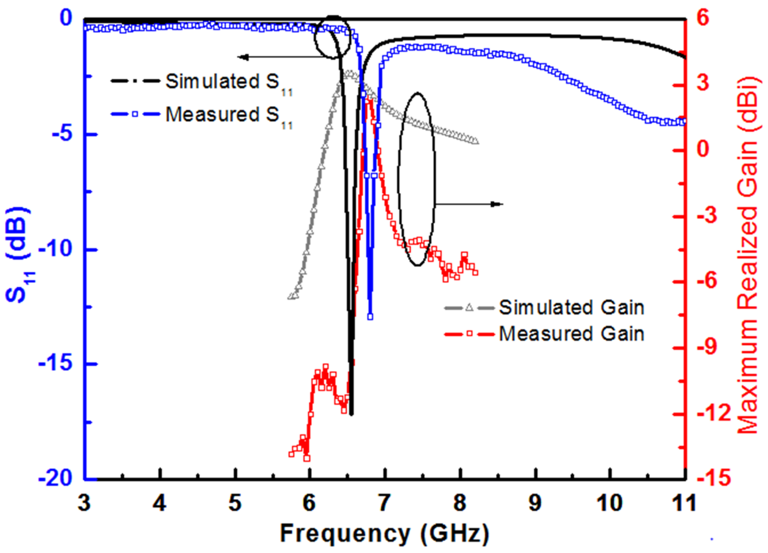

Figure 3.41: Simulated and measured S_{11} and maximum realized gain (x-y plane) of narrowband antenna of configuration E.

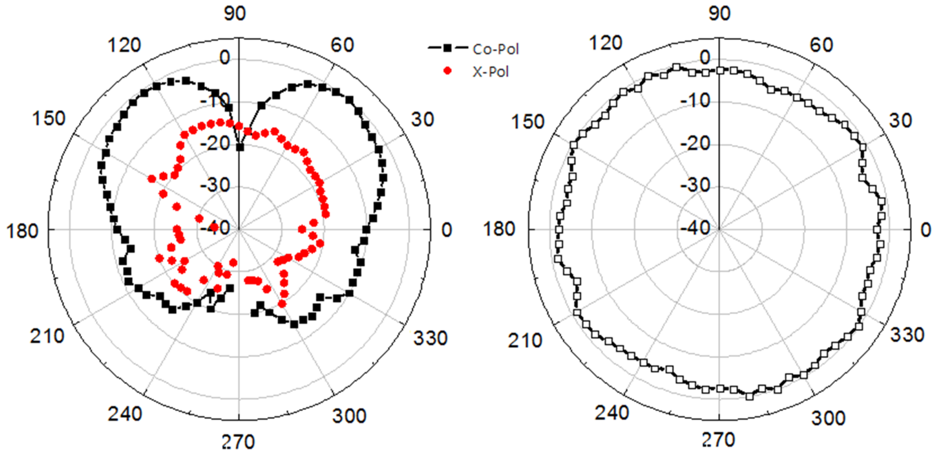

Figure 3.42: Measured normalized (a) E (x-y) plane co and X-pole and (b) H (x-z) plane co-pole radiation pattern of narrowband antenna of configuration E.

the ARMA with shorting copper strips exhibits similar narrow band functionality around corresponding SRRs resonance frequency. Figure 3.43 shows the simulated and measured plots of S_{11} and maximum realized gain versus frequency for this configuration. Impedance and gain profile with a peak gain of 1.76 dBi at 7.62 GHz ensures narrow band operation of this configuration. The measured normalized radiation in two principal planes is also consistent and identical to that of configuration E.

Figure 3.44 shows the plots of S_{11} and maximum realized gain of the antenna

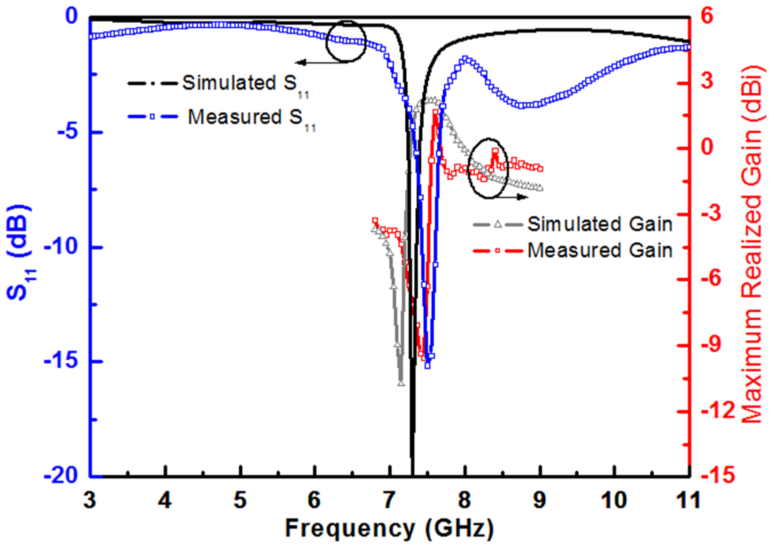

Figure 3.43: Simulated and measured S_{11} and maximum realized gain (x-y plane) of narrowband antenna of configuration F.

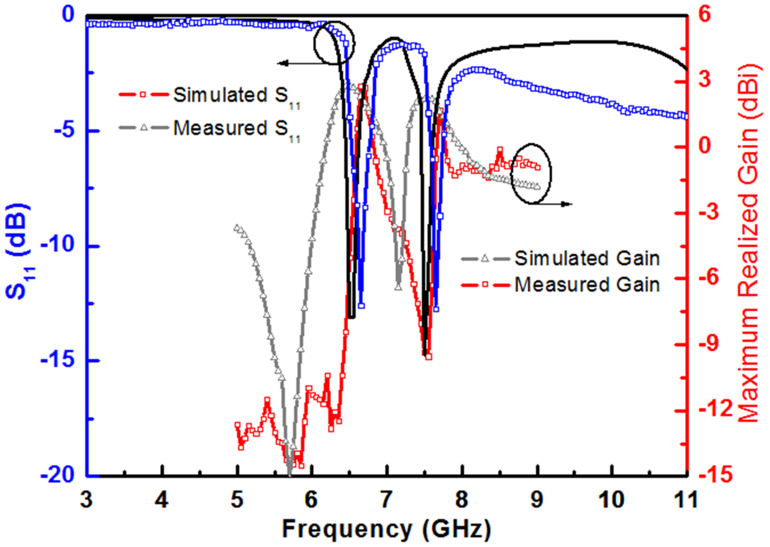

Figure 3.44: Simulated and measured S_{11} and maximum realized gain (x-y plane) of narrowband antenna of configuration G.

configuration G. Due to the SRRs printed both beneath the substrate and on the multi-layered superstrate in the ARMA with shorting copper strips, two different resonances are excited in this configuration which in turn provides narrow band response around each SRR's resonance frequency. The plots of figure 3.44 confirm narrow band functionary at 6.66 GHz and 7.69 GHz with peak measured gain of 3.02 dBi and 1.98 dBi around each SRR pairs resonance frequency. The measured radiation pattern of the antenna shown in figure 3.45, indicates monopole like omni-directional nature. Simulated contour plots of the poynting

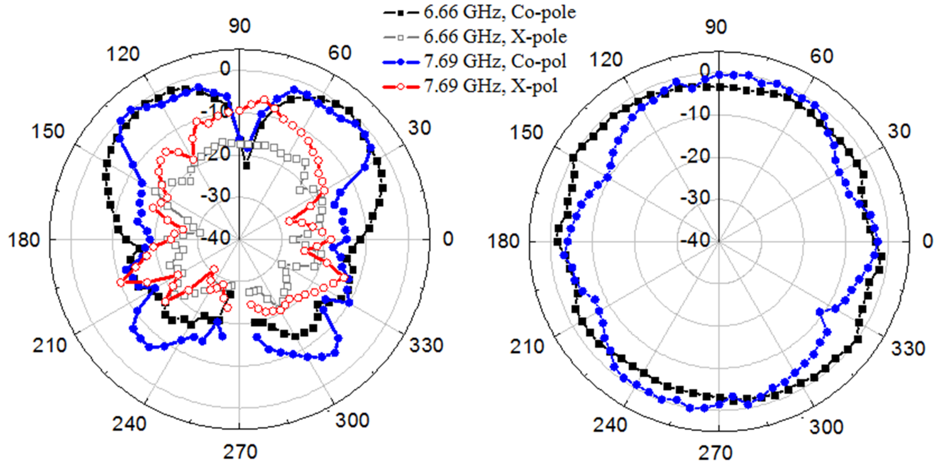

Figure 3.45: Measured normalized (a) E (x-y) plane co and X-pole and (b) H (x-z) plane co-pole radiation pattern of narrowband antenna of configuration G.

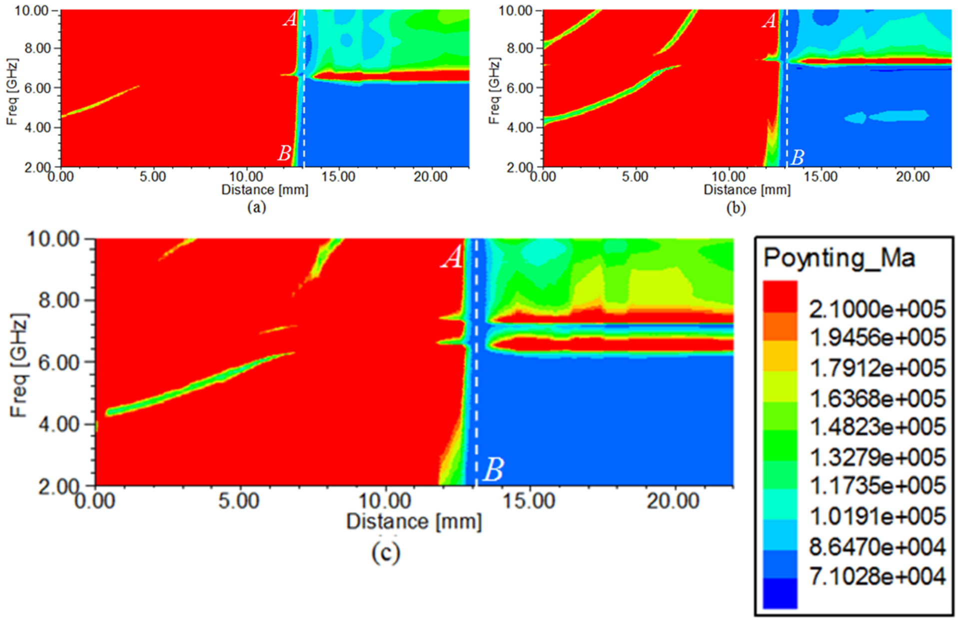

Figure 3.46: Simulated contour plots of poynting vectors of the propagating electromagnetic energy though the longitudinal dimension of one of the slots as a function of frequency (a)-(b)Configuration E, F indicating energy propagation at single frequency. (c) Configuration G indicating energy propagation at dual frequencies.

vector, for configurations E, F and G are shown in figure 3.46 and it indicates exactly complementary response to that of notched UWB configurations of B, C and D respectively, reconfirming the narrowband antenna response. The antenna configurations E, F and G are excited at 6.47 GHz, 7.38 GHz and (6.47, 7.38 GHz) due to narrow band pass response of the SRR and copper strip loaded CPW line. It can be observed from figure 3.46(a)-(c), all indicating narrowband excitation of the antenna (configuration E, F and G) that the distance from the feed port of the antenna to the position of filtering action exactly matches with the position of respective SRR pair and copper strips (on other side) on the CPW.

3.3.3 Lumped Element Based Equivalent Circuit Validation

The complementary response of the proposed antenna configurations can be interpreted from the lumped element equivalent circuit model of the antenna, with SRR loaded in the substrate or superstrate layer or in both layers with and without strips loading. As discussed earlier in section 2.5, SRR can be modeled as L-C resonator tank circuit. Due to the sub-wavelength resonance phenomenon of the SRR, the host CPW medium can also be represented as cascade of lumped element equivalent circuit. The inclusion of copper strips between the signal line and the ground planes (for configuration G) is modeled by introducing additional shunt inductor, L_p. Thus using lumped element equivalent circuit of the SRRs in two layers, host CPW medium and shorting copper strips (for configuration G), we obtain the resultant lumped element equivalent circuit of antenna configuration D and G, as shown in figure 3.47. It should be noted that the equivalent circuit model of configuration D is exactly same as that of figure 3.47 minus the shunt inductors indicating the copper strips (shown in dotted line). Applying symmetry along the longitudinal axis through the centre of the signal line, the CPW is modeled as a series inductor L and shunt capacitor C. The input port is terminated with $2 * R_0 = 100\ \Omega$ while output port of the CPW is terminated with $2 * Z_A(f)$ where, $Z_A(f)$ is the input impedance of the stand-alone ARMA obtained from electromagnetic simulation. The CPW inductance and capacitance are obtained as $L = p * L_{pul}$ and $C = p * C_{pul}$ where L_{pul} and C_{pul} are per unit length inductance and capacitance of the CPW and p is the unit cell size obtained from the SRRs dimension. The SRRs loaded beneath the substrate and on the superstrate are electromagnetically coupled with the host CPW medium with a coupling co-efficient k, calculated as in [Saha et al. (2015)], and are represented by two separate LC circuits. Two different SRR pairs for (configuration D and G) are modeled as two tank circuits: L_{SRR1} and C_{SRR1}, representing the self-inductance and capacitance of the bottom SRR; L_{SRR2} and C_{SRR2}, representing to that of top SRR pair loaded on the superstrate.

The lumped element based equivalent circuit of figure 3.47, corresponding to configurations D and G are simulated using ADS circuit simulator [Agilent (2015)]. The equivalent circuit parameters for these configurations are: $L_{SRR1} = 8.63$ nH, $L_{SRR2} = 6.58$ nH, $C_{SRR1} = 68.91$ fF, $C_{SRR2} = 69.96$ fF, $L_p = 118$ nH (for configuration G). The circuit parameters for the host CPW medium for unit cell size of $p = 5$ mm are $L = p * L_{pul}$, $C = p * C_{pul}$ where $L_{pul} = 261.16$ nH and $C_{pul} = 63.29$ pF. The coefficients of coupling between the host CPW and two SRR pairs are, $k_1 = 0.25$ and $k_2 = 0.2$. Figure 3.48 shows the magnitude of simulated reflection coefficient, S$_{11}$ in dB for configuration D and G. As observed from circuit simulation, configuration D provides two frequency notches at 6.52 GHz and 7.42 GHz while configuration G corresponds to the complementary impedance profile with

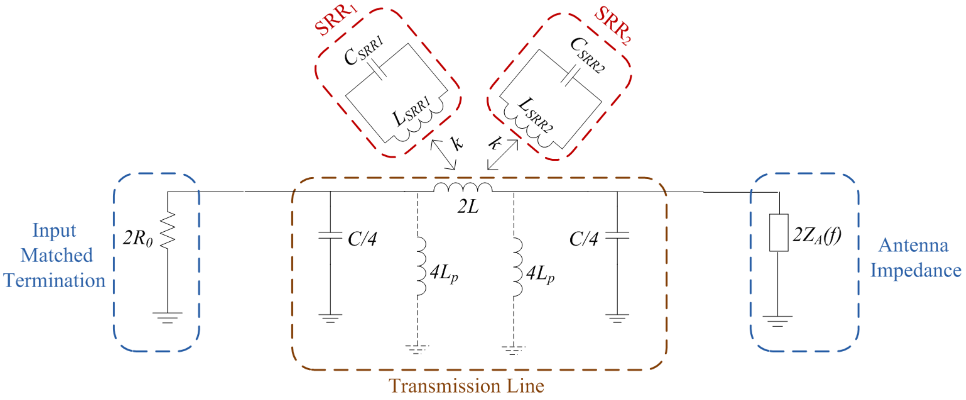

Figure 3.47: Lumped element equivalent model of the proposed multilayered SRR loaded dual notched or dual narrow band CPW fed ARMA for configuration D and G. Due to the symmetry, the magnetic wall concept has been used and the circuit corresponds to one half of the structure. Shunt inductance L_p, representing the inductance of the copper strip between signal line and ground plane connected by dotted lines, are present in configuration G.

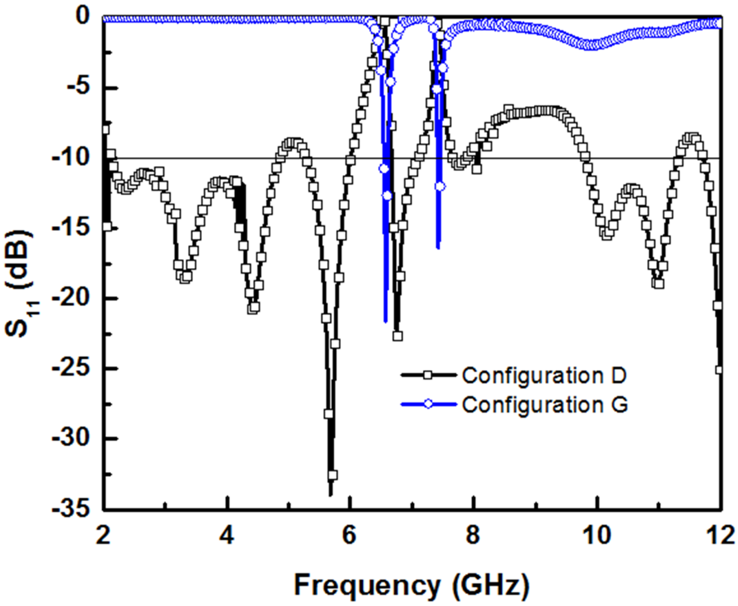

Figure 3.48: S_{11} characteristics of the proposed multifunctional antenna for configurations D and G derived from lumped element equivalent model.

narrowband operation at 6.55 GHz and 7.44 GHz respectively. Similar complementary response can also be observed for configuration B/E and C/F, where only one tank circuit corresponding to either bottom or top SRR is to be considered. Thus, proposed design concept is validated with lumped element based equivalent circuit simulation.

Table 3.4: Functional boolean table of the square SRRs loaded CPW fed slotted circular monopole antenna demonstrating seven antenna configurations

Configuration	**Shunt strip**	**Top SRR**	**Bottom SRR**	**Functionality**
A	0	0	0	UWB
B	0	0	1	Notched UWB (f_1)
C	0	1	0	Notched UWB (f_2)
D	0	1	1	Notched UWB (f_1, f_2)
E	1	0	1	Narrowband (f_1)
F	1	1	0	Narrowband (f_2)
G	1	1	1	Narrowband (f_1, f_2)

The various antenna configurations derived from the same annular ring monopole antenna, can be summarized as in Table 3.4, using Boolean representation. Here ‘0’ indicates absence of the elements and ‘1’ indicating presence of it.

3.4 Conclusion

A new design concept of a multi-functional antenna providing frequency notched UWB operation and multiple narrow band configurations is presented. The design concept has been validated using electromagnetic solver, circuit simulation and practical measurements. The design technique is independent of the radiator and can be extended to other antennas as demonstrated. Superstrate loading on the feed section of the antenna to accommodate one extra pair of SRR also helps in reducing the foot print of the antenna. Notch frequencies can be tailored by proper choice of the SRRs dimension.

CHAPTER 4

Electronically and Mechanically Actuated Multi-Functional Circular Monopole Antenna

4.1 Introduction

The multi-functional antennas response is demonstrated in the chapter 3 employing SRR and/or switches loaded in the feed region of the antenna. This is done on two different families of printed antennas, i) printed monopole antenna and ii) tapered slot antenna. Switches employed in these works are static copper switches which are connected/disconnected between the signal line and two ground planes to mimic its ON/OFF status. Though this method of realizing switches are adequate for proof of concept experiment, real-time applications demand practical switches to be controlled by some actuation signal. This chapter deals with this practical realization of the printed multi-functional antenna using electronic and mechanical means. Electronic reconfigurability is achieved by replacing the copper switches with commercial PIN diodes. The state of the PIN diode (ON/OFF) can be controlled electronically by providing the bias voltage. By employing the PIN diode the functionality of the antenna can be modified from ultra-wideband notched antenna to narrowband antenna. Mechanical reconfigurability is achieved by sliding the superstrate printed with different SRR laterally in the feed section with the help of motor and rack-pinion mechanism. The motor is programmed with Arduino Uno microcontroller. The superstrate is loaded with SRRs of varying sizes and its movement is precisely controlled to excite various resonances sequentially. This in turn contributes to reconfigurability of the frequency notch of the ultra-wideband antenna or the narrowband operating frequency. The details of the above stated functionalities are discussed in length in the following sections.

4.2 Electronically Reconfigurable Multi-Functional Antenna

4.2.1 Antenna Design and Fabrication

Here, a unique frequency reconfigurable capability that transforms a frequency notched wideband antenna into a narrowband antenna where the narrowband frequency complements the notch frequency, is achieved by electronic switching. A single printed monopole antenna loaded with SRRs and PIN diodes on the feed section provides this dual functionality. The frequency notch in the wideband printed monopole antenna is caused by the SRRs which are magnetically coupled with feeding CPW line and inhibit signal propagation around the SRR's resonance frequency [Martin et al. (2003); Siddiqui et al. (2014, 2015)]. With the loading of PIN diodes on CPW and appropriate biasing, the frequency notched wideband antenna can be reconfigured into a narrowband antenna operating at the SRR's resonance. The design is realized using a printed circular monopole antenna having a wide impedance bandwidth. The printed monopole is fed by a CPW transmission line loaded with a pair of SRRs and commercial PIN diodes. It is further demonstrated that the notch frequency and the narrowband frequency can be tuned by changing the physical dimension of the SRR geometry without perturbing the radiator dimensions. Moreover, the inclusion of the SRRs and the PIN diodes on the feed section of the antenna do not have any adverse impact on the radiation performance of the antenna.

Figure 4.1 shows the schematic of the proposed filtenna. A circular monopole having radius R is fed by a CPW consisting of ground planes having width, W_1 and W_2, length, L_s and a signal line of width, S and length, $L_s + t$. The signal line and the ground planes are separated by a symmetric pair of slot gaps, s_g. The filtenna is printed on a substrate having thickness h and dielectric constant ϵ_r. Two square shaped split ring resonators having dimension, a_{ext}, which is half the dimension of the side-length of the SRR, conductor thickness c, separation between rings d and split gaps g_1 and g_2 as shown in figure 4.1(c), are printed on the other side of the substrate with their centers coinciding with the slot lines of

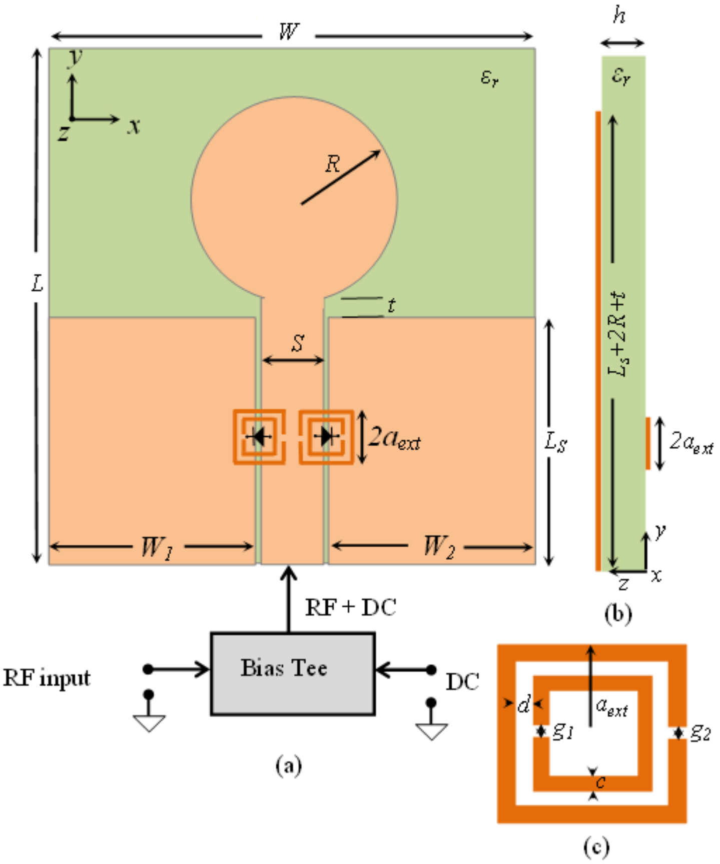

Figure 4.1: Schematic of SRR coupled PIN diode loaded filtenna (a) Top view of CPW fed printed circular monopole connected to external bias tee with a pair of SRRs printed on the back side and a pair of PIN diodes on the CPW slots. (b) Side View showing the printed SRRs separated by h from the PIN diode loaded CPW feed line. (c) Schematic of a unit cell of square SRR, a pair of which is printed on the back side of the CPW feed line and aligned with the PIN diodes.

the CPW feed. A pair of PIN diodes are placed on the slots of the CPW with their positions coinciding with the axes passing through the center of the SRRs. The CPW transmission line is loaded with PIN diodes which on different biasing conditions (reverse and forward) would effectively open and short the signal line with the ground planes. This, in turn provides frequency notched response and its complementary narrow band response.

The prototype was fabricated on Taconic substrate having $\epsilon_r = 2.33$, tan $\delta = 0.0009$ and thickness $h = 1.575$ mm. The circular monopole having radius

$R = 12.5$ mm and fed with a CPW having ground plane length $L_s = 22.5$ mm, width $W = 50$ mm, signal line width $S = 6$ mm, slot gap $s_g = 0.3$ mm and feed gap $t = 0.2$ mm was etched on one side of the substrate. The slot gaps and the signal line width were optimized to yield a line impedance close to 50 Ω. A pair of SRRs having dimensions $a_{ext} = 2.5$ mm, $c = 0.35$ mm, $d = 0.6$ mm and split gaps $g_1 = g_2 = 0.5$ mm, were printed on the other side of the substrate with their axes coinciding with the slot line in the CPW as shown in figure 4.2. A pair of silicon PIN diodes (SMP 1145) were placed on the slots between the ground planes and the signal line and aligned to the position of SRRs axes. As shown in figure 4.2(b), the required DC bias to the diodes are provided using a Mini circuits 15542 bias tee.

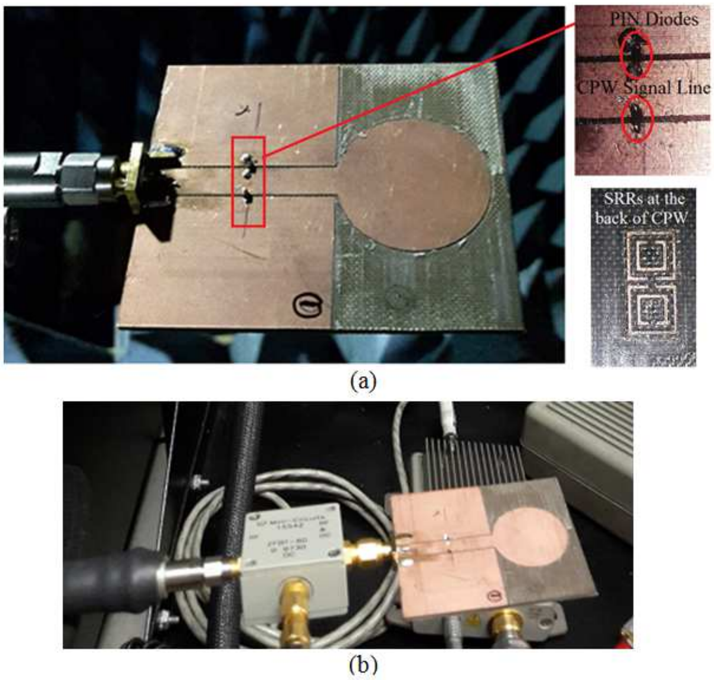

Figure 4.2: (a) Fabricated prototype of the proposed filtenna with a magnified view of the PIN diodes accommodated between the signal line and ground planes of the CPW. SRRs are printed on the opposite side of the CPW (b) Prototype connected to the Mini Circuits bias Tee.

4.2.2 Simulation and Measurement Results

The proposed SRR and PIN diode loaded filtenna is simulated using a commercial electromagnetic simulator [ANSYS (2015)]. In this simulation two different configuration of the filtenna for ON and OFF state of the diodes are considered by replacing the diodes with the corresponding equivalent circuits as shown in figure 4.3. The lumped circuit parameters, obtained from the manufacturer's data sheet, in diode ON condition assigned in the simulation were $L_s = 0.45$ nH and $R_s = 2\Omega$ and in diode OFF condition were $L_s = 0.45$ nH and $R_p = 5$ MΩ and $C_T = 0.14$ fF. The resultant HFSS model with lumped circuit parameters for both the cases are simulated. Figure 4.4 shows the simulated and measured S_{11} plots of the proposed filtenna for OFF status of the diode. The plot indicates wideband characteristic from 2.5 GHz to 11 GHz with a sharp notch at 6.1 GHz and 6.01 GHz for simulated and measured data, respectively. This notch corresponds to the resonance

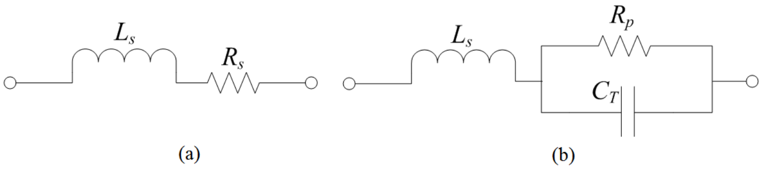

Figure 4.3: Lumped equivalent circuit of the PIN diode in (a) ON and (b) OFF state.

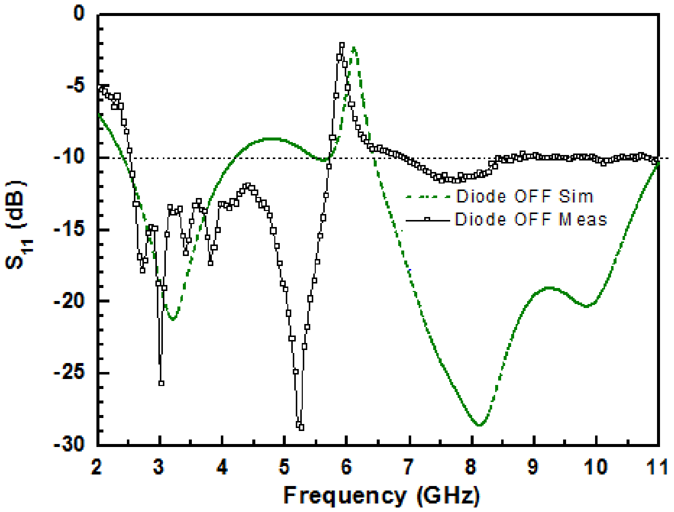

Figure 4.4: Simulated and measured S_{11} of the SRR coupled PIN diode loaded CPW fed printed circular monopole filtenna with diodes in OFF condition.

frequency of the SRR and can be varied by scaling the physical dimension of the SRRs [Siddiqui et al. (2014)].

Figure 4.5 shows the simulated and measured S_{11} of the prototype filtenna with the diode in ON condition. As revealed in the plot, with the diode in ON condition, the filtenna yields a narrowband response centered at 6.12 GHz and 6.02 GHz for simulated and measured data and effectively complements the impedance behaviour of the filtenna in diode OFF condition. Figures 4.4 and 4.5 reveal the complementary nature of the antenna under diode OFF and ON conditions. Filtenna with diode ON condition provides a narrow band response due to the narrow band pass filter formed with the combination of SRRs and PIN diodes on the slots of the CPW. On the other hand, with diode in OFF condition, the band notch filtering of the SRRs contribute to frequency notched UWB response of the antenna.

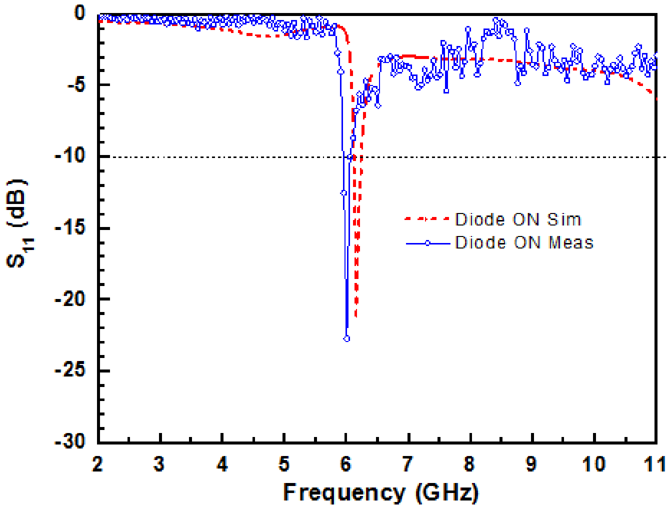

Figure 4.5: Simulated and measured S_{11} of the SRR coupled PIN diode loaded CPW fed printed circular monopole filtenna with diodes in ON condition.

The biasing of the diodes is conducted through 5V D.C. supply connected to the bias tee. The current flowing through the diodes in forward bias condition provides the DC-short between signal and ground planes of the CPW which in turn reconfigures the notched wideband antenna into a narrowband antenna. Figure 4.6 shows the measured maximum realized peak gain plotted against the frequency of the prototype filtenna in diode OFF and ON conditions. In diode OFF condition, the gain drops sharply at the notch frequency of 6.01 GHz pro-

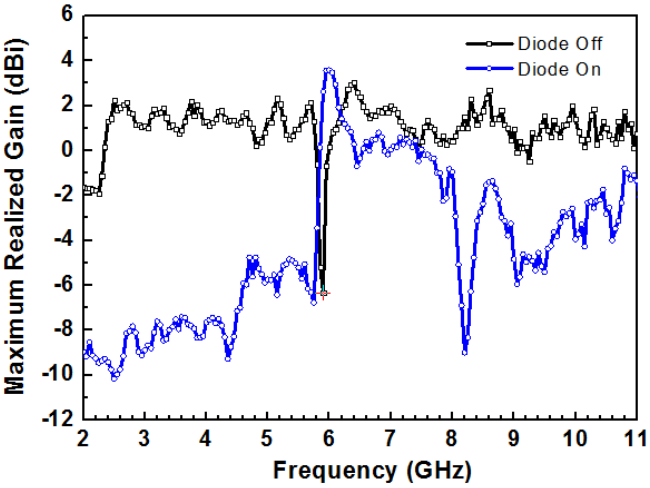

Figure 4.6: Measured realized peak gain of the SRR coupled PIN diode loaded CPW fed printed circular monopole antenna with diodes OFF and ON conditions.

hibiting radiation whereas for the rest of the frequencies the gain remains above 0 dBi. A complementary gain profile is yielded when the diode is switched ON and the gain rises sharply to radiate at 6.02 GHz and drops off at either side of the radiating frequency. The measured maximum gain value in diode ON condition at the narrowband frequency 6.02 GHz was obtained as 3.59 dBi.

The measured normalized radiation patterns in two principal planes, the x-y-plane (E-plane) and x-z-plane (H-plane), for the prototype in diodes OFF condition are shown in figure 4.7(a) and (b), respectively, for 3.8 GHz, 8 GHz and 9.4 GHz. The E-plane and H-plane at 6.02 GHz for diode ON condition are shown in figure 4.7(c) and (d). The radiation patterns indicate axial null along y-axis ensuring monopole type radiation for the x-y-plane with high cross polar discrimination. The H-plane radiation yields an omni-directional pattern for the x-z-plane. The simulated efficiency was obtained at 92% and 76% for diode OFF and diode ON conditions, respectively.

The physical insight of the complementary nature of the antenna response can be explained by observing the magnitude of the Poynting vector in diode ON and diode OFF conditions as illustrated in figure 4.8. As shown in figure 4.8(a), with the diode in OFF condition, the SRR prohibits propagation of electromagnetic energy at its resonance frequency yielding a notched UWB response. With the diode in ON condition, a complementary nature of the propagation is triggered

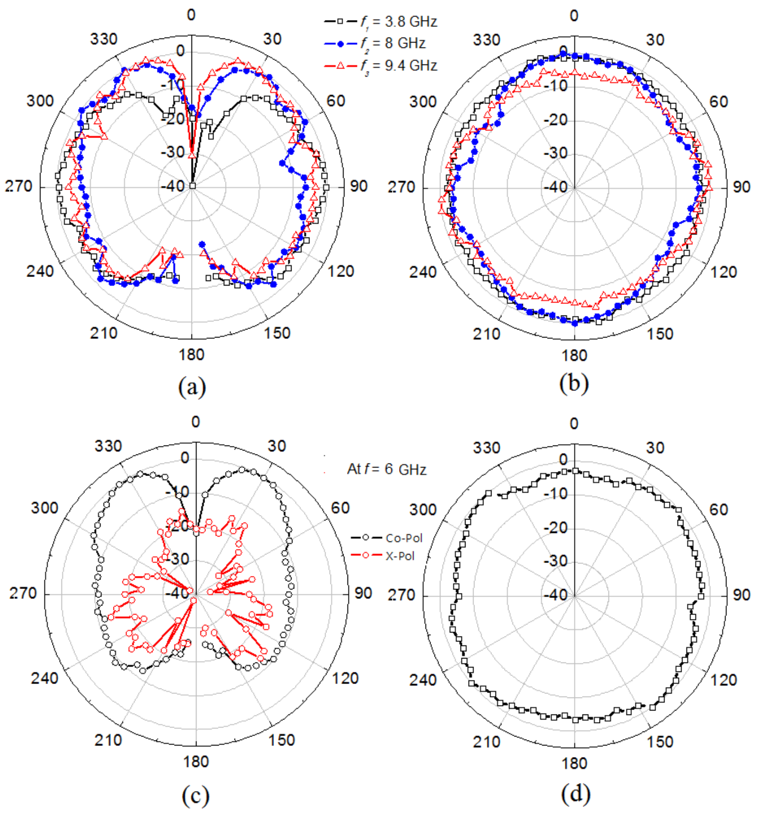

(a) (b)

(c) (d)

Figure 4.7: Measured normalized E and H-plane radiation patterns of the fabricated filtenna. (a) and (c)x-y plane (E-plane) in diode OFF and ON conditions. (b) and (d) x-z plane (H-plane) in diodes OFF and ON condition.

where electromagnetic energy over only a narrow frequency, at approximately the SRRs resonance frequency is propagated. The rest of the energy is reflected back to the input port as depicted in figure 4.8(b).

Figure 4.9 shows the simulated reflection coefficient of the proposed antenna for different a_{ext} dimensions in diode ON and diode OFF conditions. Three different a_{ext} dimensions of 2.3 mm, 2.5 mm and 2.7 mm yielded notch frequencies in diode OFF condition at 5.45 GHz, 6.1 GHz and 6.65 GHz while with diode in ON condition narrowband response centered at 5.5 GHz, 6.15 GHz and 6.7 GHz is obtained. Figure 4.9 has an inset which shows the zoomed-in view of the notch and narrowband frequencies from 5 GHz to 7 GHz to increase the legibility. The wide variation of the notch and narrowband frequency using the proposed concept by changing the SRR parameter and without altering the basic radiator dimension is evident from the figure. Similar variation can also be achieved by changing

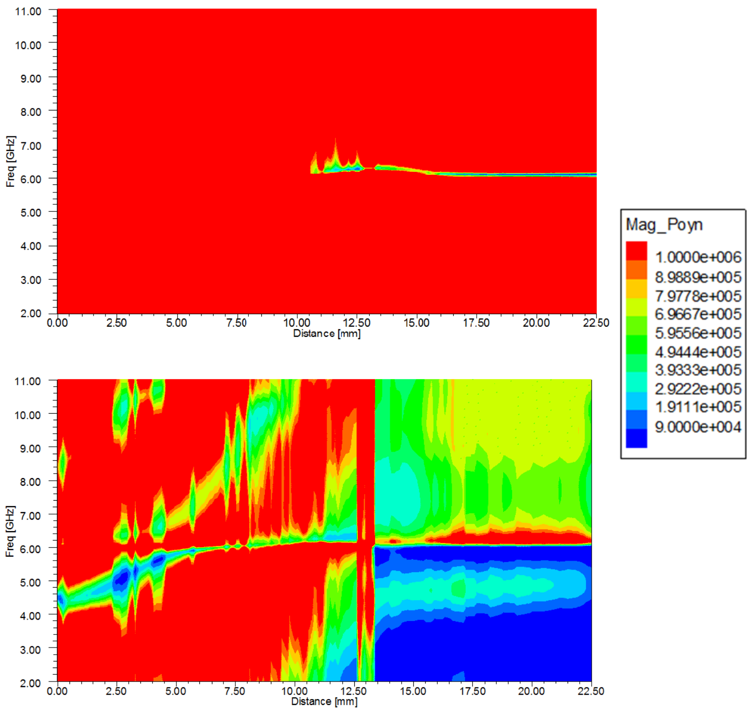

Figure 4.8: Simulated contour plots of the magnitude of the Poynting vectors through one of the CPW slots as a function of frequency. (a) with diodes OFF condition and (b) with diodes ON condition. (Plots are in uniform scale).

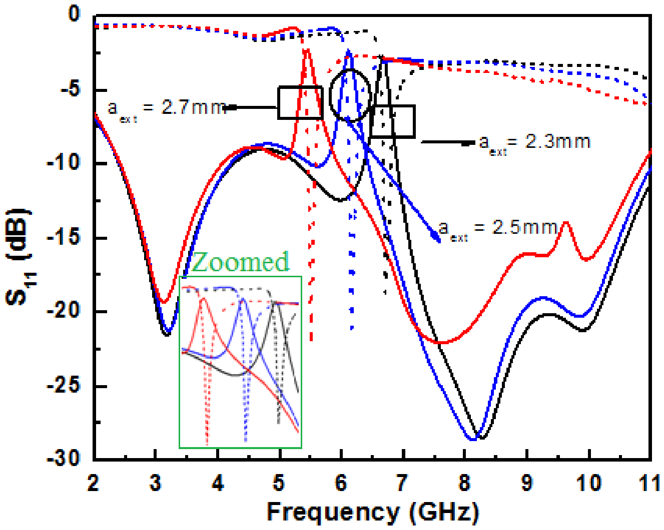

Figure 4.9: Simulated S_{11} of the SRR coupled PIN diode loaded CPW fed printed circular monopole filtenna with diodes OFF and ON conditions for various a_{ext} values. Solid curves are for diode OFF case and dotted curves are for diode ON case.

the other parameters of the SRRs like c, d and g. The corresponding simulated maximum realized gain as a function of frequency of SRRs with varying a_{ext} is shown in figure 4.10. The dip and peak in gain parameters in diode OFF and ON conditions are evident from the plots.

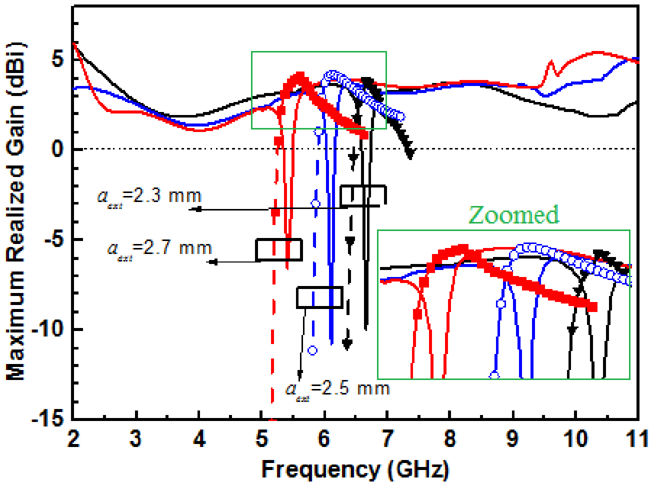

Figure 4.10: Simulated realized peak gain of the SRR coupled PIN diode loaded CPW fed printed circular monopole filtenna with diodes OFF and ON conditions for various a_{ext} values. Solid curves are for diode OFF case and dotted curves are for diode ON case.

4.3 Mechanically Reconfigurable Multi-Functional Antenna

4.3.1 Antenna Design and Fabrication

In chapter 3, various antenna functionalities were demonstrated by loading a superstrate in the feed region of the antenna on which an additional pair of SRRs were printed. This SRR and/or another pair of static SRRs printed beneath the substrate and a switch connected between the signal and ground line were utilized in achieving the multi-functional antenna response. However, the notches/narrow band response of the same antenna can be tuned by a combination of mechanical and electronic means. Mechanical movement of superstrate printed with three pairs of SRR of different dimensions in the feed region of the radiator can provide the desired tunablity of the antenna. The basic radiator is a popularly known CMPA and is fed by CPW. Further, as discussed in previous section, loading the shunt strip in the feed region of the antenna provides frequency notched UWB and narrowband impedance characteristics. Two complementary frequency reconfigurable functionality, i) tunable notched UWB antenna and, ii) tunable narrowband antenna, is demonstrated in this section. Mechanical movement of the superstrate is realized using an indigenously designed rack and pinion arrangement and actuated through a servo motor controlled by an Arduino Uno microcontroller. Alignment of the particular SRR pair's center with that of the center of the slot lines of the CPW, excites SRR resonance which in turn provides the frequency notch in the UWB antenna. Thus, based on various positions of the superstrate, achieved through suitably programming of the Arduino Uno microcontroller, the proposed antenna can provide a tunable notch function.

The same antenna, when loaded with a pair of switches in the CPW slots and similar mechanical movement of the SRR loaded superstrate is performed, it results into a reconfigurable narrowband antenna under ON condition of the switch. Thus, based on mechanical movement of the superstrate layer and status of the switches (ON/OFF), proposed antenna can provide a dual reconfigurable characteristics. In addition, design concept of the frequency notched/narrowband operation can be extended to other planar UWB antennas. Since in this work reconfiguring block is in the feed region, their placement, bias lines etc. has minimal impact on the radiation characteristics of the antenna. Proposed antenna is a potential candidate as communicating antenna for cognitive radio applications, where the notched UWB function can be used when the primary user is utilizing the spectrum and narrowband antenna in the complementary situation. An illustration of the antenna functionality and reconfigurability is shown in the flow chart of figure 4.11.

The overall antenna design consists of a CPW fed circular monopole and reconfigurable elements in the form of PIN diodes and a moveable superstrate loaded with SRRs of different dimensions in its feed region whose position is mechanically controllable using a servo motor controlled by Arduino Uno microcontroller. The antenna can provide two complementary characteristics, namely, reconfigurable frequency notched UWB operation and reconfigurable narrowband opera-

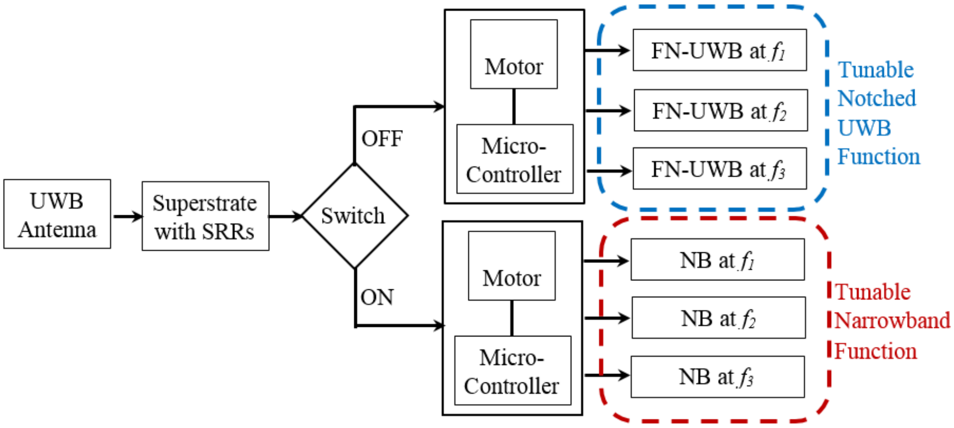

Figure 4.11: Flowchart representation of the antenna configurations achievable through the proposed antenna.

tion. The functional reconfigurability (Notched UWB/Narrowband) is obtained by employing two switches in ON/OFF mode in the feed regions while frequency reconfigurability in the corresponding state is provided by mechanical movement of the superstrate on which SRR of varying dimensions are printed. The mechanical

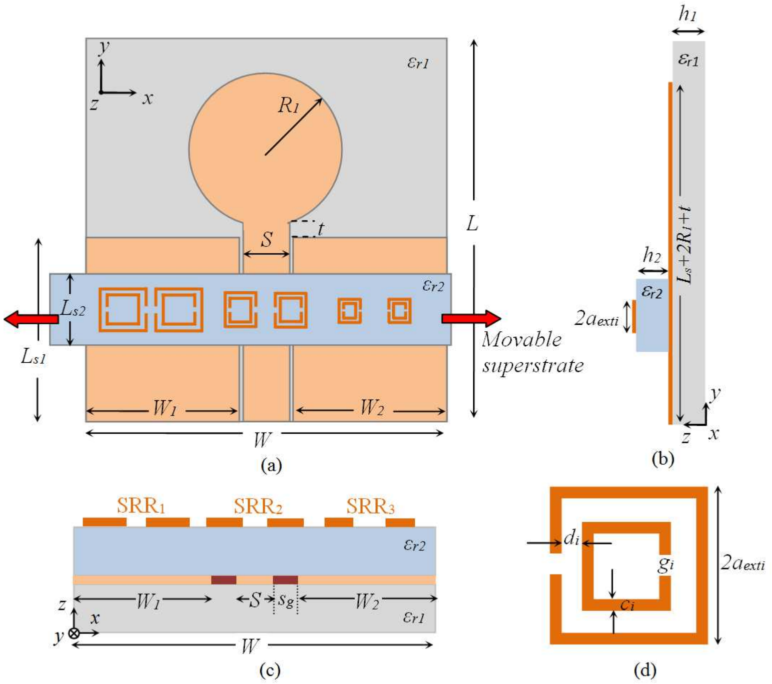

Figure 4.12: Geometrical layout of the proposed antenna (a) top view along with the movable superstrate printed with SRR, (b) side view of the antenna, (c) cross-sectional view with copper strips (red wine colour) placed in the slots for narrowband operation and (d) unit cell of the SRR.

movement of the superstrate is precisely controlled with the indigenously designed rack-pinion arrangement and commercial servo motor programmed by an Arduino Uno microcontroller. Figure 4.12 shows the geometrical layout of the antenna. It consists of a CPW fed CMPA with and without the switches to achieve the basic complementary functionalities. The radiating circular monopole has a radius R_1, placed at a distance of t from the CPW feed for proper impedance matching. CPW feed comprises signal line of width S and ground planes of width $W_1 = W_2$ and lengths L_{S1}. The antenna has length L and width W, and is printed on a substrate of dielectric constant ϵ_{r1} and thickness h_1. The square SRR consists of two concentric rings with exterior sidearm length $2a_{exti}$, width, c_i, inter-ring spacing, d_i and split gaps, g_i placed on opposite sides of the rings. Figure 4.12(a) and (b) shows the top and side view of the proposed antennas while figure 4.12(c) shows the cross-sectional view of the antenna. Geometrical layout of a standalone SRR is shown in figure 4.12(d). Three different sized SRRs are printed on a substrate of dielectric constant ϵ_{r2}, thickness h_2 with dimension of length L_{S2} and width W. The structure is modelled and simulated in a commercial EM solver [ANSYS (2015)]. Figure 4.13 shows the fabricated prototypes of the antenna, superstrate printed with SRRs and the rack and pinion all designed and realized by in-house fabrication facility.

The antenna design parameters are summarized in Table 4.1. The antenna and the superstrate are printed on RT Duriod 5870 ($\epsilon_{r1} = \epsilon_{r2} = 2.33$ and tan $\delta = 0.0012$) of thickness $h_1 = h_2 = 1.575$ mm.

Here, we utilized both ON/OFF switches and the mechanical movement to achieve the dual reconfigurability. The servo motor is utilized to move the superstrate and thereby providing the reconfigurability in the notch location/narrowband operation depending on status of the switches (ON/OFF), respectively. In order to achieve the rectilinear movement of the rectangular superstrate, we opted for the gear support mechanism i.e., rack and pinion arrangements where the rotational motion of the pinion would give rise to rectilinear motion of the rack. The rack and pinion are 3D-printed using the ABS-plastic and are as shown in figure 4.13(c). To provide the mechanical movement, the superstrate is attached to the rack and the pinion is placed on the spindle of the servo motor as shown in figure 4.14(a). The servo motor utilized is Towerpro SG90 commercial servo which can

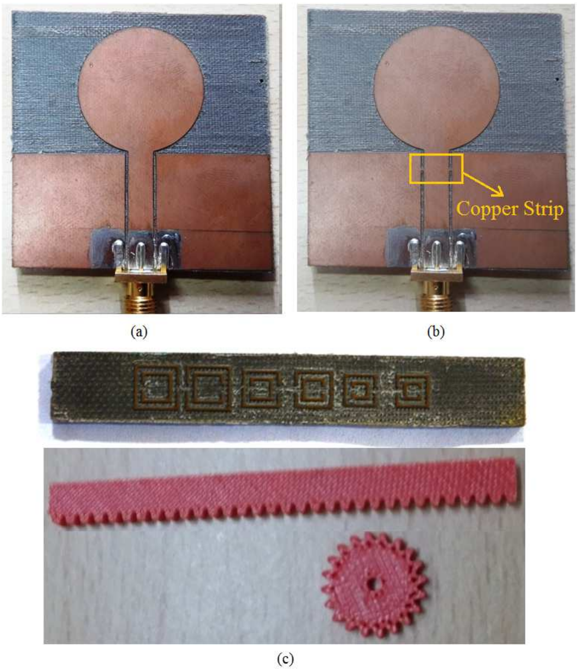

Figure 4.13: Fabricated prototype of (a) circular monopole antenna, (b) circular monopole antenna with copper strips in the slots of the feed region, (c) superstrate of the antenna with three different pair of SRRs printed along with the rack and pinion used for mechanical reconfigurability.

Table 4.1: Design paramters of the fabricated antenna and the superstrate with SRRs. (Paramteric variables as shown in figure 4.12)

Antenna Design Parameters		L	W	L_{s1}	L_{s2}
		50	50	22	12.5
		W_1	W_2	S	s_g
		22	22	5	0.5
		t	L_{s2}	h_1	h_2
(All dimensions are in mm)		0.2	10	1.575	1.575
SRR Parameters (All dimensions are in mm)	#	a_{ext}	c	d	g
	SRR_1	2.25	0.5	0.3	0.5
	SRR_2	1.9	0.5	0.3	0.5
	SRR_3	1.73	0.5	0.3	0.5

provide 180^o rotation and has minimum footprint area. The motor is controlled using Arduino Uno microcontroller which provides the control on the movement

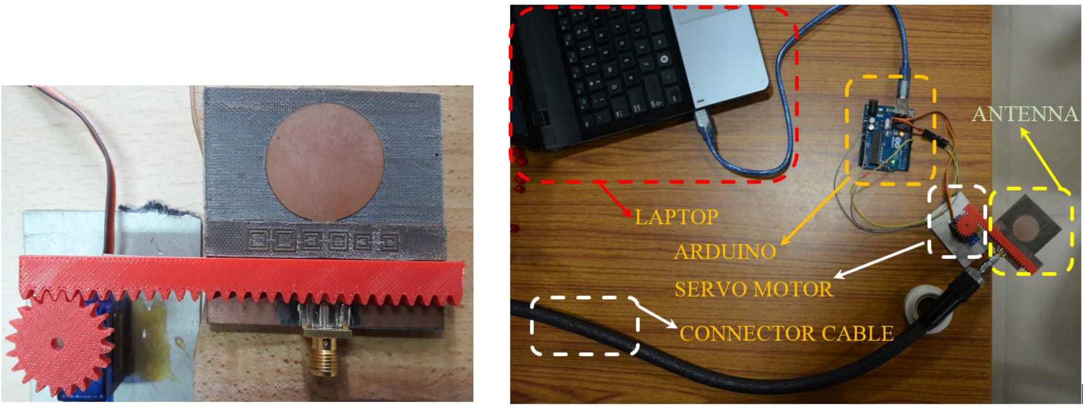

(a) (b)

Figure 4.14: (a) Fabricated prototype of the antenna indicating the superstrate placement, along with rack and pinion mounted on servo motor for reconfigurability, (b) complete measurement setup indicating the microcontroller and personal computer to control the reconfigurability.

of the superstrate. The required 5 V DC supply of the motor, is provided by the microcontroller and the microcontroller is powered through USB cable attached to a personal computer and which provides the control code programmed in Arduino. The overall setup is shown in figure 4.14(b). The software coding to control the servo motor and thereby the rectilinear motion of the superstrate, is done in Arduino. The superstrate position can be controlled by specifying the angle of rotation of the motor (either discrete movement or continuous) so that one SRR pair is aligned with the slots of the feeding section. The Arduino code is given in appendix A and B. Initially SRR_2 is aligned to the slots; when angle is specified superstrate moves to align SRR_3, then back to SRR_2 and then to SRR_1 as the servo motor can move 90^o in either direction.

4.3.2 Simulated and Measurement Results

Initially, to simplify the design process, the PIN diode's OFF and ON state is mimicked using a copper strip, absence of strip representing OFF state and presence as ON state. Absence of copper strip results in frequency notched UWB response whereas, their existence yields a complementary narrowband response. Figure 4.15 shows the measured screenshot of the reflection coefficient (S_{11}) of CMPA loaded

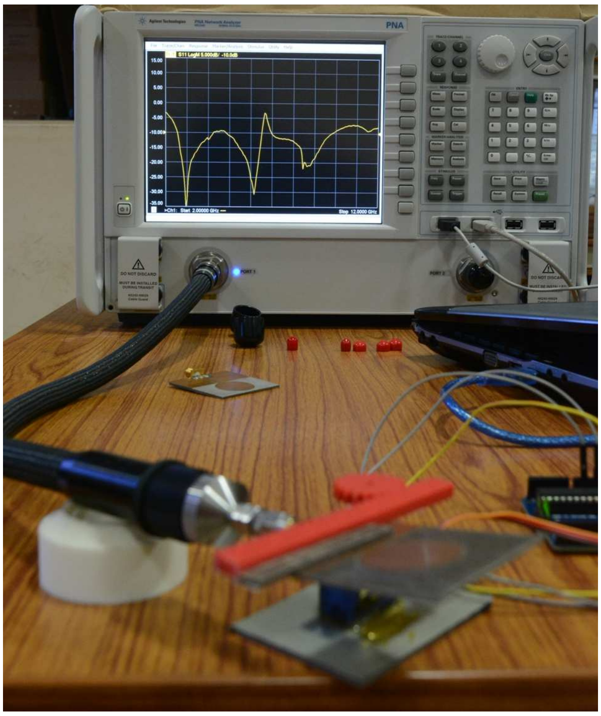

Figure 4.15: Measured S_{11} characteristics of the circular monopole antenna loaded with SRR printed superstrate along the feeding microstrip line for SRR1 pair aligned along the slots. Antenna parameters are as detailed in TABLE 4.1

with superstrate comprising of SRRs with the entire setup. Frequency notched UWB characteristics can be observed in the VNA's display for a single case where the SRR_2 is aligned to the slots of the feed section of antenna. With the aid of the Arduino coding and the servo motor, the superstrate is moved laterally so that different SRRs printed on it can be aligned resulting in three different frequency notched UWB responses. Figure 4.16 shows the simulated and measured S_{11} of CMPA for three different pair of SRRs alignment with respect to the slots of feed section. The CMPA offers a wideband impedance characteristic from 2.6 GHz to 10.8 GHz [Siddiqui et al. (2014)]. The impedance characteristics of CMPA with superstrate are similar to that of CMPA except for the notch, implying that the superstrate loading has minimal impact on its impedance characteristics. Depending on the SRRs alignment the notch frequency is controlled. $SRR_i(i = 1, 2$ and $3)$ yields a notch in UWB response at 6.66 GHz, 8.34 GHz and 9.85 GHz in measurement against 6.5 GHz, 8.34 GHz and 9.55 GHz for simulation, respectively. The notch frequency is function of the geometrical dimensions of the SRR and can be tailored to the desired frequency by adjusting the SRR dimensions without affecting the antenna design. Theoretically, the resonance frequency of the SRR_i ($i = 1$, 2 and 3) is 6.67GHz, 8.69 GHz and 10.16 GHz.

When a pair of copper switches are placed between the slots of the feed section directly below the SRR, the present antenna is transformed into narrowband

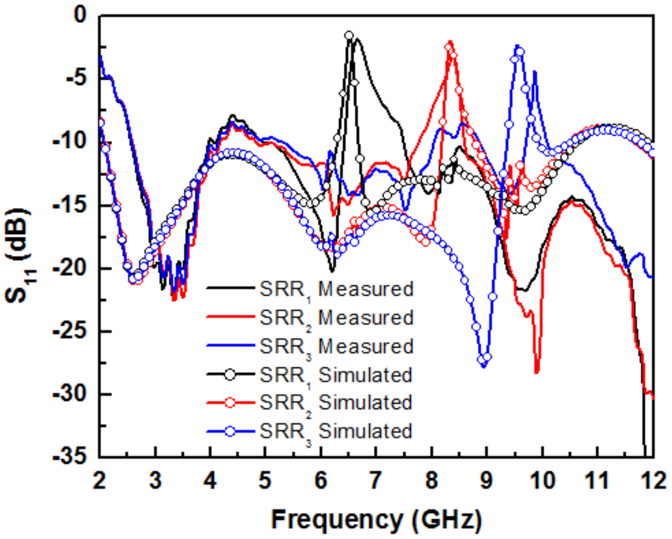

Figure 4.16: Simulated and measured S_{11} characteristics of the circular monopole antenna loaded with SRR printed superstrate along the feeding microstrip line for different SRRs aligned along the slots.

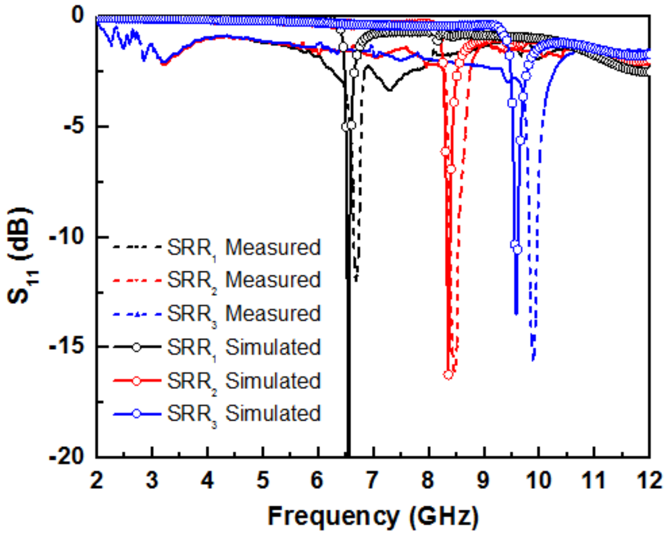

Figure 4.17: Measured S_{11} characteristics of the circular monopole antenna loaded with SRR printed superstrate along the feeding microstrip line for SRR_1 pair aligned along the slots. Antenna parameters are as detailed in TABLE 4.1

antenna with a complementary impedance characteristic. To realize this configuration as shown in figure 4.13(b), copper strips, acting as closed switch (ON), are added between the ground and signal plane of the CPW. An identical process, as described for the reconfigurable notch case, is utilized to move the superstrate to align different SRR pairs. Figure 4.17 shows the simulated and measured reflection coefficient (S_{11}) of this narrowband configuration. Depending on the SRR-pairs alignment with the slot lines, tunable narrowband operations are achieved. For SRR_i (i = 1, 2 and 3) the narrowband response at 6.69 GHz, 8.45 GHz and 9.89 GHz is obtained in measurement against 6.57 GHz, 8.34 GHz and 9.58 GHz for simulation, respectively. It can be observed from figures 4.16 and 4.17 that the obtained tunable notches and tunable narrowband response are complementary to each other.

The measured normalized radiation patterns of the CMPA antenna for frequency notched UWB response in x-y plane and y-z plane for two cases (SRR_1

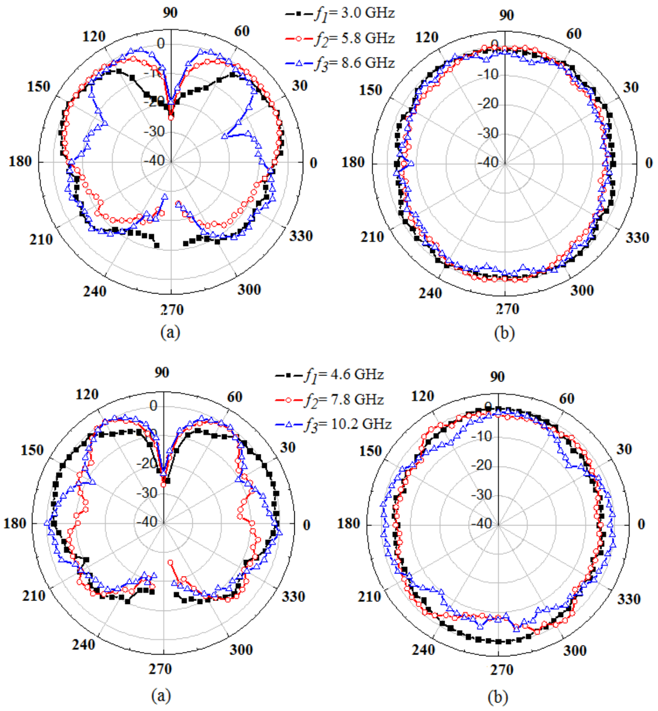

Figure 4.18: Measured (a) E-plane (x-y) (b) H-plane (y-z) radiation patterns for the fabricated circular monopole antenna loaded with SRR printed superstrate for two different SRRs (SRR_1 and SRR_3) aligned along the slots for the frequency notched UWB operation.

and SRR$_3$) are presented in figure 4.18. Figure 4.18(a) and (b) represents the measured normalized E- and H-plane radiation pattern of the CMPA with SRR$_1$ and SRR$_3$ on superstrate aligned to slot at (3 GHz, 5.8 GHz and 8.6 GHz) and (4.6 GHz, 7.8 GHz and 10.2 GHz), respectively. The antenna exhibits directional pattern in E-plane (x-y plane) with axial nulls along y-axis and nearly omni-directional pattern in H-plane (y-z plane). The pattern is consistent over the operating bandwidth, and the co-pol to cross-pol discrimination is about 10-15 dB over its operating bandwidth. Figure 4.19 represents both measured normalized E-Plane and H-plane radiation pattern of the CMPA with narrowband response for SRR$_1$ and SRR$_3$ at 6.69 GHz and 9.89 GHz. The simulated radiation efficiency computed as ratio of gain and directivity is plotted for both the configurations (frequency-notched UWB and narrowband) in figure 4.20. The radiation efficiency is minimum at the notch frequency, confirming the presence of notch and acceptable radiation performance at other frequencies.

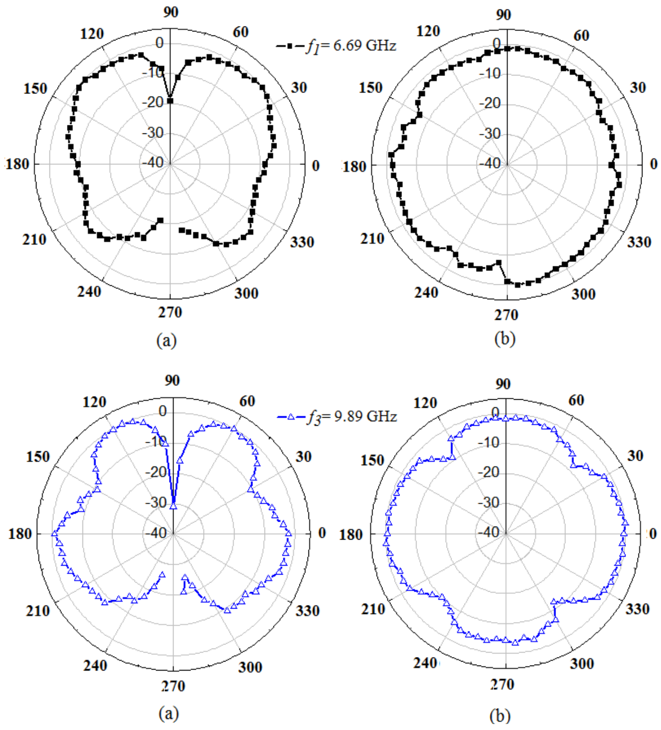

(a) (b)

(a) (b)

Figure 4.19: Measured (a) E-plane (x-y) (b) H-plane (y-z) radiation patterns for the fabricated circular monopole antenna loaded with SRR printed superstrate and copper strip for two different SRRs (SRR_1 and SRR_3) aligned along the slots for the narrowband operation.

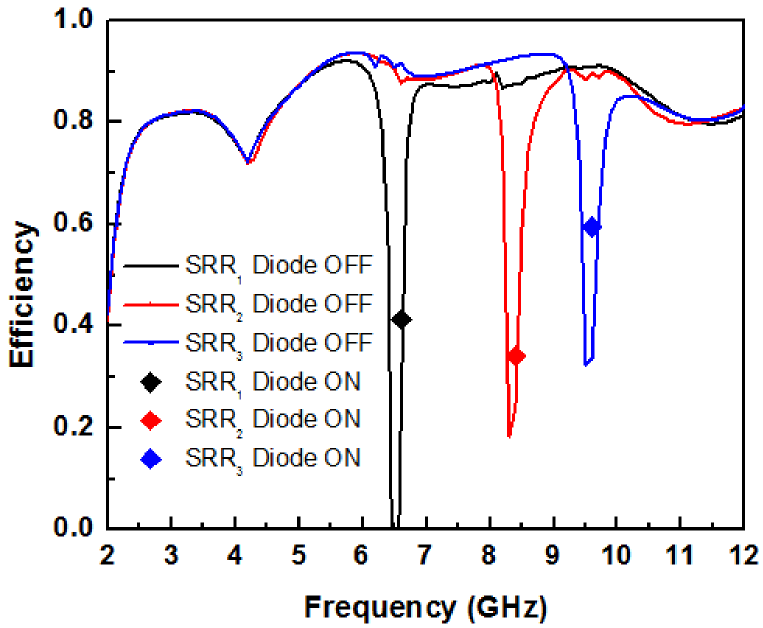

Figure 4.20: Simulated and measured efficiency of the proposed antenna for (a) frequency notched UWB operation (b) narrowband operation with the SRR_1 aligned across the slots of the feed section.

4.3.3 Electronic Switch Actuated Reconfigurability

To demonstrate the antenna functionality change (from notched UWB to narrowband) in a more practical manner, the copper switches are replaced with the PIN diode. To demonstrate the switching response, a silicon PIN diode (SMP1345-040LF) is utilized. As design has to be carried out in both EM and circuit solver, EM co-simulation platform of the CST Microwave studio is employed. The antenna is modelled in the 3D layout and to incorporate the diode for schematic simulation discrete port is placed at diode's location. With this, the 3D layout, look like as in figure 4.21(a), where '1' indicates the excitation port for the antenna and '2', '3' indicate the discrete ports where diodes PIN are connected. Once the 3D layout simulation is executed, the schematic simulation window is employed where the diodes are replaced by their equivalent circuit at terminal 2 and 3. The resultant EM and circuit model is again simulated to achieve final response. The PIN diode in OFF state is represented by a parallel RC circuit in series to inductor with $R_{OFF} = 5\ \mathrm{M}\Omega$, $C = 0.14$ fF and $L = 0.45$ nH and while in ON state it is represented by a series RL circuit with values $R_{ON} = 2\ \Omega$ and $L = 0.45$ nH as

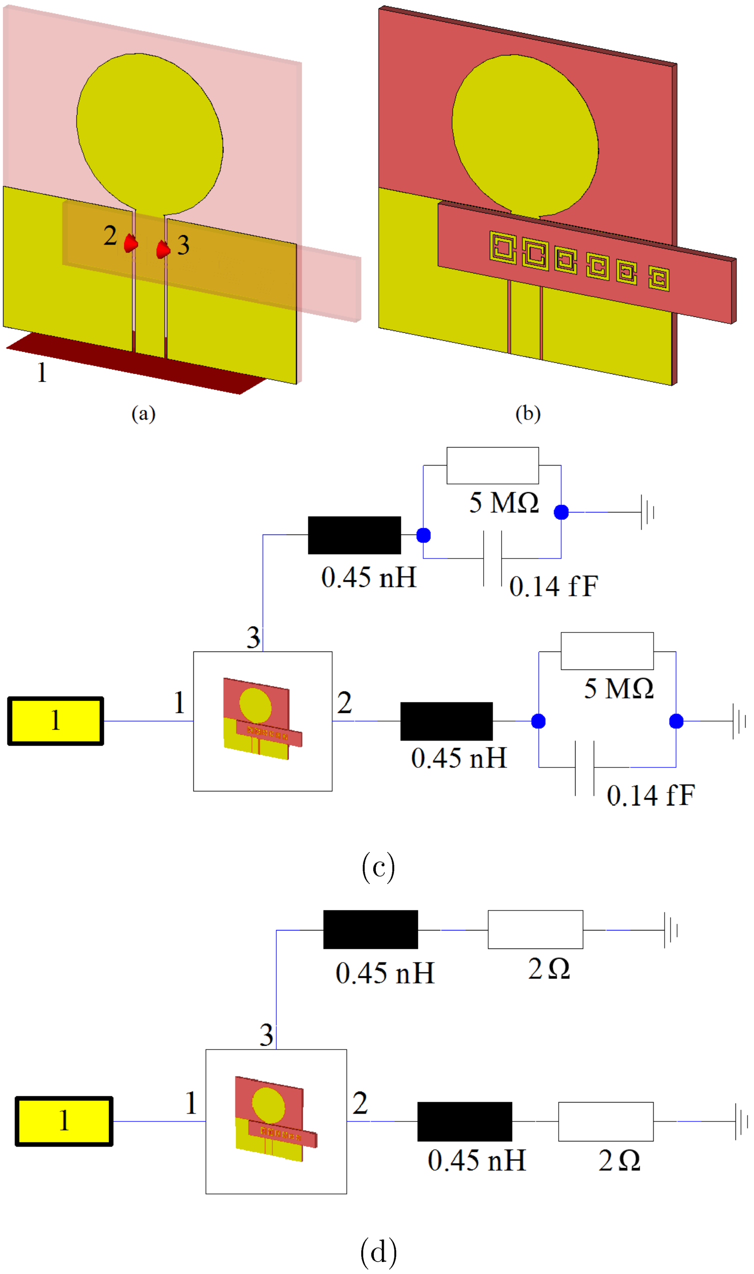

Figure 4.21: Simulation setup for PIN diode simulation in CST (a) port definition waveport (1) and discrete ports (2 and 3) in order to facilitate PIN diode connection in schematic (b) perspective view of the structure (c) and (d) Schematic layout showing PIN lumped element equivalent connected to antenna in OFF and ON state respectively

shown in figure 4.21(c) and (d), respectively. The simulated reflection coefficient for one set of SRR is shown in figure 4.22 for both the diode OFF and ON case and confirms complementary antenna response.

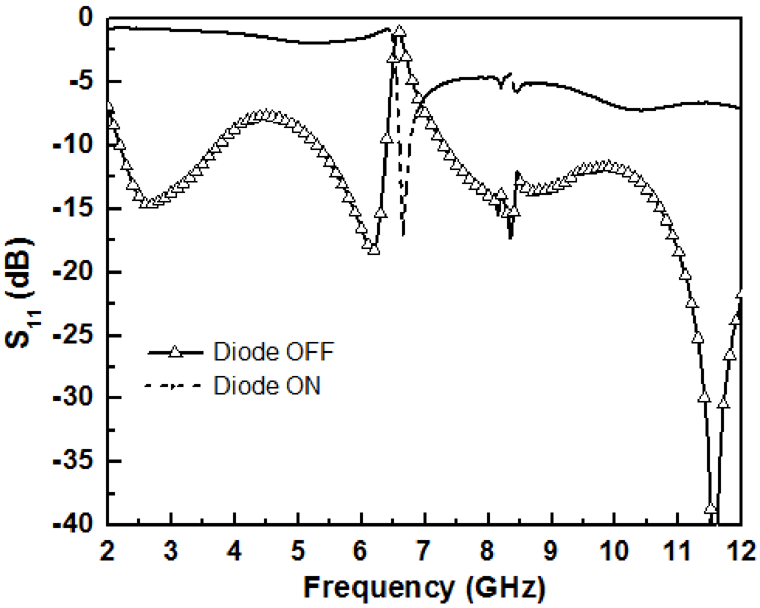

Figure 4.22: Simulated S_{11} characteristics of the circular monopole antenna loaded with SRR printed superstrate along the feeding microstrip line for SRR_1 aligned along the slots with the diode OFF and ON condition.

4.4 Conclusion

A novel, but simple idea to design a multi-functional antenna with frequency notched wideband response and a complementary narrowband response is proposed and realized. The combination of the SRRs with different conditions of diode bias yield the two complementary characteristics. The reconfigurability within the desired characteristics (either frequency notched wideband or narrowband) is realized by movement of the superstrate with the help of motor controlled by Arduino Uno microcontroller. Prototypes were fabricated to validate the concept. Since the notch and narrow band frequency is determined by the SRRs geometry, several multi-dimensional SRRs can be used for multiple frequency notched or multiple narrowband applications.

CHAPTER 5

Bandwidth Controllable Cylindrical Ring Dielectric Resonator Antenna

5.1 Introduction

The previous chapters of the thesis dealt with either the functional reconfigurable and/or the shifting the notch or the narrowband response in a printed circular monopole antenna. In this chapter, a mechanism to control the bandwidth of an antenna is demonstrated. Since dielectric resonator antennas of special shapes when excited by proper feeding mechanism, exhibits maximum bandwidth, a new technique to control its bandwidth is investigated. Such integrated bandwidth controllable technique, without using an external filter have potential applications in scenarios where the bandwidth controllability is desired to control the required signal-to-noise ratio of the over-all receiving system or to completely block the interference from a known station/source. The dielectric resonator antenna (DRA), originating from simple dielectric resonators (DRs) [Long et al. (1983)], has been attracting the attention of antenna researchers over the last two decades for its several appealing features and advantages. Various research groups have contributed immensely in diverse aspects of DRA research, including i) the study of various DRA shapes and geometries leading to enhanced operational bandwidth [Petosa and Ittipiboon (2010); So et al. (2011)], ii) new excitation techniques identifying new modes with different impedance and radiation properties [Guha et al. (2012, 2014a)], iii) designs for lower cross-polarized radiation [Ryu and Kishk (2011)], circular polarization [Huang et al. (1999); Zou et al. (2012)], and polarization-diversity applications [Zou and Fumeaux (2011)], iv) compact designs for compatibility with wireless systems [Hady et al. (2009); Lan et al. (2003); Huitema et al. (2011); Rao et al. (2005)], and v) design of active, tunable and reconfigurable varieties [Petosa et al. (1995); Li et al. (1996); Leung and So (2005); Petosa (2007); Ng and Leung (2006); Desjardins et al. (2012); Apperley and Okoniewski (2014);

Danesh et al. (2014)]. A significant fraction of DRA works reported to date also focus on bandwidth-enhancement techniques [Lapierre et al. (2005); Guha et al. (2009, 2014b); Ittipiboon et al. (1996); Mongia et al. (1994); Leung et al. (2003); Kishk (2003); Kishk et al. (2002); Hsiao et al. (2002a); Buerkle et al. (2005); Esselle and Bird (2005); Hsiao et al. (2002b); Chang and Kiang (2007); Mitra et al. (2009); Ghosh and Chakrabarty (2008)]. These techniques include modifying the DR geometries [Guha et al. (2009, 2014b)], lowering the effective Q factor by various techniques [Ittipiboon et al. (1996); Mongia et al. (1994); Leung et al. (2003)], augmenting the DR element with additional parasitic elements [Kishk (2003); Kishk et al. (2002); Hsiao et al. (2002a)] and by modifying the feeding mechanism [Buerkle et al. (2005); Esselle and Bird (2005)], exploiting additional resonances contributed by parasitic metallic elements loaded on top of the DR [Hsiao et al. (2002b)]. Rectangular DR with partially coated metallic walls and metal strip loading has been demonstrated to yield broadband response in [Mitra et al. (2009); Ghosh and Chakrabarty (2008)], respectively. Although the majority of DRA research of late has been focused on bandwidth enhancement, it is equally desirable to control the bandwidth to suit specific applications, particularly where collected noise power, and therefore SNR, must be managed. The use of external filters to achieve bandwidth control increases the design complexity of the antenna and built-in mechanisms for bandwidth control are, therefore, of significant interest.

In this section, a broad range of tuning the upper cut-off frequency with a tunable percentage bandwidth is demonstrated for a CRDR excited by a quarter-wave monopole using two different configurations: 1) loading the top of the CRDR with an annular metallic cap of varying inner radius, as shown in figure 5.1(a), and 2) loading the CRDR's outer surface with a cylindrical metallic sleeve of varying height shorted with the ground plane as shown in figure 5.1(b). The choice to tune the upper side of the radiation bandwidth of the unloaded antenna (monopole + CRDR) is due to the fact that lower cut-off frequency of such a hybrid antenna is determined by the monopole's fundamental resonance and as such, is not controllable by mechanical/electrical tuning. The CRDR antenna in unloaded condition is excited in the $TM_{01\delta}$ mode by the central conductor of a commercial 50-Ω probe acting as a quarter-wavelength monopole. Several new modes in such

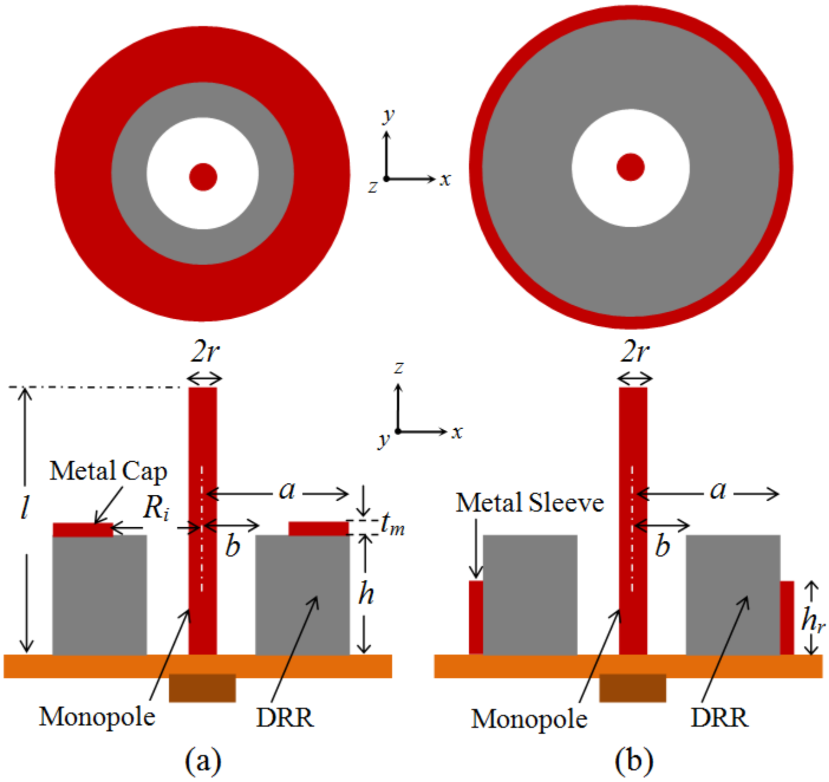

Figure 5.1: Top and cross-sectional view of (a) metallic-cap and (b) metallic-sleeve loaded monopole-excited CRDR antenna on a ground plane.

hybrid antennas have been reported in [Guha et al. (2014a)]; however, we have selected the $TM_{01\delta}$ mode for excitation, to demonstrate the proposed bandwidth controllability. The proposed antenna is derived from a hybrid combination of a CRDR excited by a quarter-wavelength-long vertical electric monopole exhibiting a very wide bandwidth [Guha et al. (2014b)]. A quarter-wavelength monopole of length l mounted on a ground plane excites the CRDR of inner and outer radii b and a, respectively, with height h having dielectric constant ϵ_r. This vertical electric monopole excites the $TM_{01\delta}$ mode and provides the expected monopole radiation pattern with a broadside null (with respect to the ground plane).

5.2 Metallic-cap loaded bandwidth controllability

5.2.1 Antenna Design Topology

In the first configuration, as shown in figure 5.1(a), a parasitic annular metallic cap with outer radius a (equal to that of the CRDR), inner radius R_i and thickness t_m is loaded on the top of the CRDR, concentrically with the axis of the monopole and CRDR. Here R_i plays a very significant role in the performance of the antenna and changes the upper cut-off frequency of the antenna without much effect on its radiation characteristics. Detailed investigations of both types of loading of the CRDR antennas show that the bandwidth of the antenna can be controlled from 122% (for the unloaded case) to 81% for metallic-cap loading. This has been experimentally verified with caps of various dimensions, providing excellent frequency tuning without perturbing the radiation pattern and without sacrificing the gain of the antennas.

Figure 5.2(a) and (b) shows the fabricated prototype of the proposed antenna

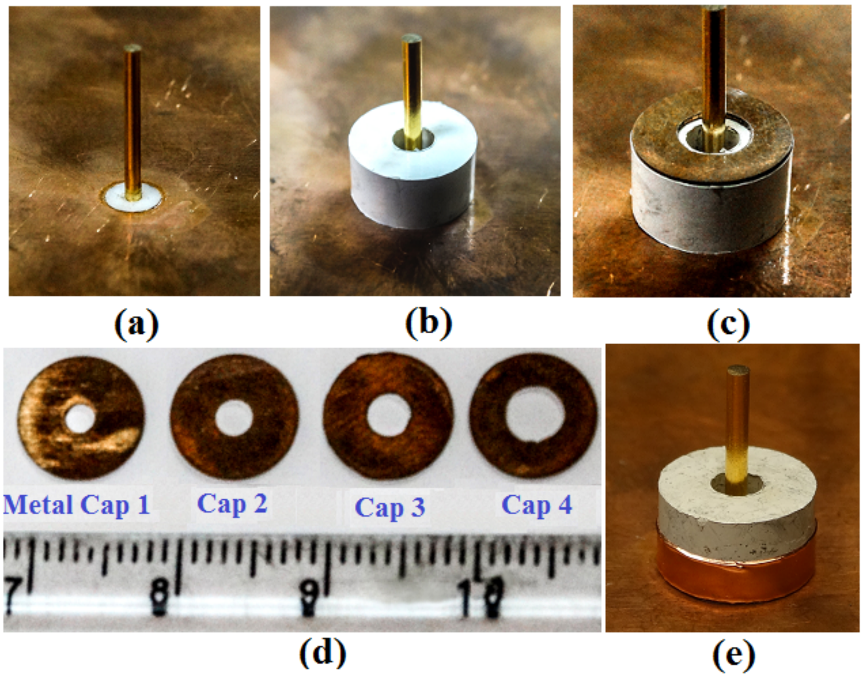

Figure 5.2: Fabricated prototypes of (a) metallic cap loaded CRDR formed by gluing CRDR to a ground plane consisting of vertical monopole (b) metallic caps of various inner radii and (c) sleeve-wrapped CRDR.

with various caps for loading. The CRDR of outer and inner radii $a = 4.4$ mm, $b = 1.5$ mm with height $h = 4.4$ mm consists of a polyethylene (PE) 0.26-volume-fraction barium titanate composite providing a measured dielectric constant of $\epsilon_r = 10.2$, and is affixed to the ground plane using conducting glue. The vertical monopole of length $l = 12$ mm and radius $r = 0.6375$ mm is realized using the pin of a commercial 50-Ω coaxial connector inserted through the ground plane and adjusted to the required length. Four different metallic caps with fixed outer radius $a = 4.4$ mm and thickness $t_m = 1$ mm with varying inner radii $R_i = (1$ mm, 1.25 mm, 1.5 mm, 2 mm), as shown in figure 5.2(b), are fabricated in a mechanical workshop using copper sheeting.

The fabricated prototypes of the metallic-cap and metallic-sleeve loaded CRDR antenna for different R_i are thoroughly investigated both for impedance and radiation characteristics. A square-shaped ground plane of 80 mm × 80 mm was used for the measurements. Both configurations were simulated using a commercial electromagnetic simulator [ANSYS (2015)] and validated with reflection coefficient and radiation pattern measurements using a Keysight PNA-X N5224A network analyzer and a fully calibrated near-field anechoic chamber. The radiation patterns were obtained using a near-field open-ended waveguide probe (OEWG)

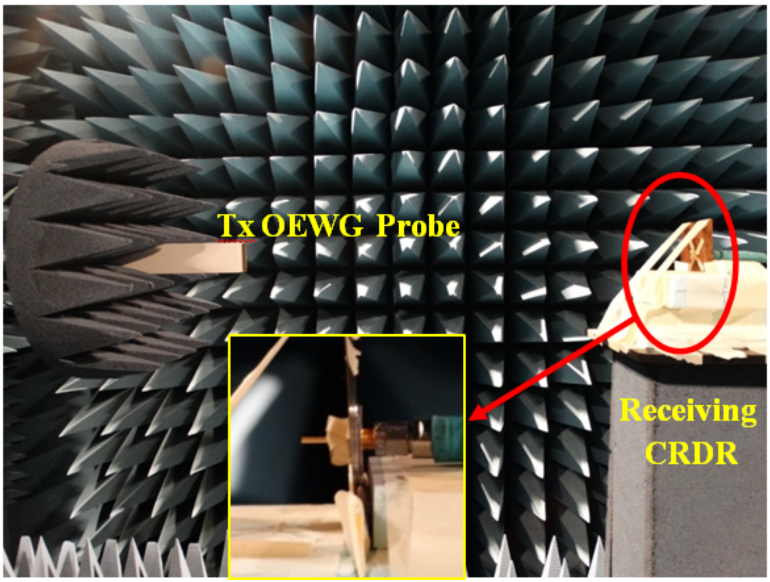

Figure 5.3: Radiation pattern measurement set-up for the fabricated CRDR mounted in the anechoic chamber with cables and transmitting antenna.

oriented in x-z plane which was used as the transmitting antenna while the CRDR antenna was placed in the receive-mode. Figure 5.3 shows the radiation pattern measurement setup. Since this paper focuses on bandwidth controllability and the H-plane (x-y) pattern is omni-directional, the measurements were limited to E-plane co-polarization measurements. To predict the effective bandwidth of the loaded CRDR antenna with respect to the unloaded case, closed form equations using curve-fitting technique are proposed.

5.2.2 Simulation and Measurement Results

The measured and simulated plots for the S_{11} versus frequency without and with metallic-cap loading for $R_i = $ (1 mm, 1.5 mm and 2 mm) are shown in figure 5.4(a)-(d), respectively. As revealed from the figures, the measured and simulated data show a very good general correspondence. For example, the measured and simulated S_{11} for the unloaded CRDR shown in figure 5.4(a) reveals an impedance

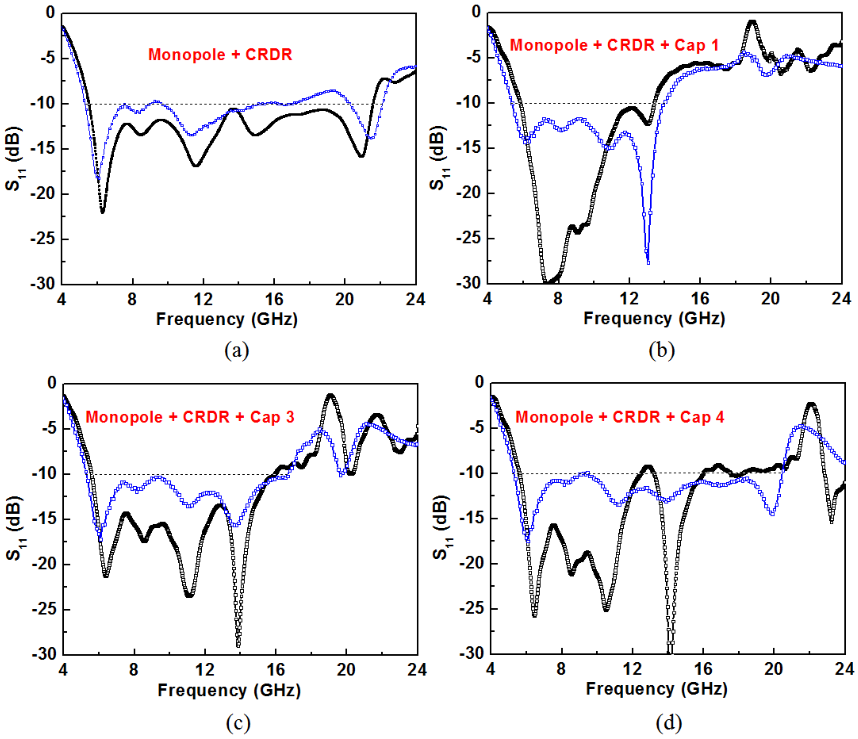

Figure 5.4: (Measured and simulated S_{11} parameters (a) CRDR alone (b)-(d) CRDR with R_i = 1 mm, 1.5 mm and 2 mm respectively. Black and blue line represents simulation and measurement respectively.

bandwidth of approximately 122%, which is in close agreement to the 112% reported in [Lapierre et al. (2005)] for a similar antenna. For metallic-cap-loaded cases [figure 5.4(b)-(d)], the measured impedance bandwidth exhibits reasonably good correspondence with the simulated data. The deviation between measured and simulated results can be attributed to fabrication tolerances, unwanted air gaps due to an imperfectly finished ground plane, and the glue affixing the metallic caps and sleeves to the CRDR and the CRDR to the ground plane. When the CRDR is loaded with a metallic cap the additional resonant LC tank circuit formed between the parasitic metal and ground plane [Hsiao et al. (2002b)] modifies the impedance matching on the higher side of the spectrum of the unloaded antenna which is exploited to achieve the proposed bandwidth controllability. As shown in figure 5.4(b)-(d) and summarized in Table 5.1, the percentage bandwidth of the antenna can be controlled from 88%-118% for the annular metallic-cap loading with different inner radii, R_i. The corresponding simulated controllable bandwidth is 81%-115%. With increasing R_i, the inductance of the metallic-cap and the capacitance with the ground plane decreases, thereby increasing the upper cut-off frequency and percentage bandwidth of the proposed antenna. This qual-

Table 5.1: Summary of the simulated and measured bandwidths for different metallic cap loaded CRDR antenna demonstrating bandwidth controllability. (Paramteric variables as in figure 5.1)

Antenna Type	Tools	f_l	f_u	% BW
Monopole + CRDR	Sim	5.5	22.65	122
	Meas	5.36	22.04	122
With Metallic Cap Loading (on top of the CRDR)				
Monopole + CRDR + Cap 1 (R_i = 1 mm)	Sim	5.66	13.4	81
	Meas	5.36	13.88	88
Monopole + CRDR + Cap 2 (R_i = 1.25 mm)	Sim	5.4	14.8	93
	Meas	5.24	15.32	98
Monopole + CRDR + Cap 3 (R_i = 1.5 mm)	Sim	5.4	15.94	99
	Meas	5.36	17.02	104
Monopole + CRDR + Cap 4 (R_i = 2 mm)	Sim	5.51	20.62	116
	Meas	5.24	20.48	118

itative concept is validated for all studied cases of metallic caps as revealed from the increasing upper-cutoff frequency with increasing R_i reported in Table 5.1.

Figure 5.5 shows the measured and simulated impedance-bandwidth plot of the proposed metallic-cap-loaded CRDR antenna against the cap inner radii (R_i), exhibiting a good correspondence. As revealed from the plot, the bandwidth of the antenna can be smoothly controlled from 17.15 GHz (unloaded case) to 7.74 GHz by varying the inner radius R_i of the metallic cap. It should be noted that since the monopole passes through the center of the cap, R_i can't be reduced below r, providing a limitation on further reduction in bandwidth. Using a curve-fitting technique, the bandwidth of the proposed cap-loaded antenna (BW_{CL}) can be expressed as

$$BW_{CL} = BW_{UL}\left(3.29 - 6.1r_i + 3.15r_i^2\right), for 0.54 \leq r_i \leq 0.77 \qquad (5.1)$$

where, $r_i = (a - r_i)/a$ is the normalized cap width and BW_{UL} is the bandwidth of the unloaded antenna.

To shed more light on this phenomenon of upper cut-off frequency controllability, the electric field inside the dielectric material at different frequencies, determined from the S_{11} plots, is obtained using simulation and compared with

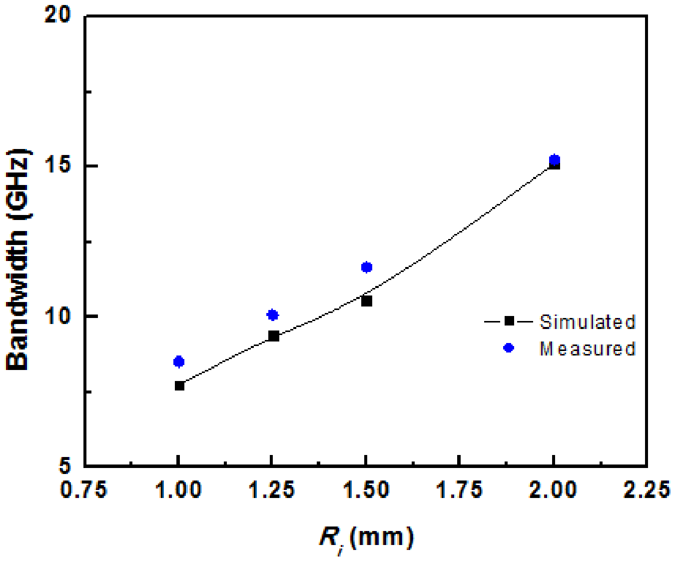

Figure 5.5: Simulated and measured bandwidth versus inner radius for monopole-excited CRDR antenna with metallic-cap loading for various cap inner radii R_i.

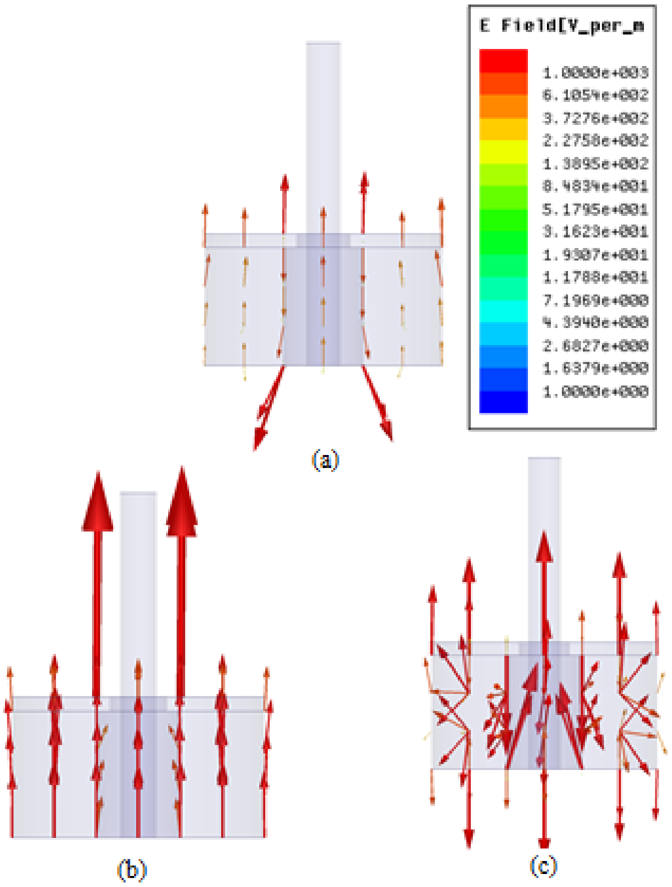

Figure 5.6: Simulated electric field distributions in the proposed bandwidth controllable CRDR antenna with metallic cap ($R_i = 1$ mm) loading at (a) 6.7 GHz (b) 10.5 GHz and (c) 16 GHz

that of the unloaded CRDR antenna. Figure 5.6 shows the simulated electric-field profile at three different frequencies, $f = 6.7$ GHz, 10.5 GHz and 16 GHz, for the metallic-cap-loaded CRDR antenna with $R_i = 1$ mm. It can be observed that at 6.7 GHz and 10.5 GHz the electric-field vector maintains polarization purity corresponding to radiation from the antenna. On the other hand, at 16 GHz, which is above the upper cut-off frequency of the antenna, the electric-field vector loses its polarization purity. This can be attributed to the resonance of the LC tank circuit formed by the metallic cap and the ground plane. Since the radiation of the antenna at lower frequencies is not impacted by this resonance, the LC tank circuit resonance sets an upper cut-off above which the antenna cannot be used. This physical insight has been verified for the CRDR antenna as well as all cases of the metallic-cap-loaded CRDR.

It can be noted that for the metallic-cap loaded configurations (Figure 5.6), the obtained electric-field polarization purity is annihilated at frequencies above the cut-off frequency (at 16 GHz for Cap 1 loading, 18 GHz for Cap 2 loading, 19.5 GHz for Cap 3 loading and 22 GHz for Cap 4 loading) of the respective configuration as seen from the oppositely oriented electric-field vectors when the metallic caps are included. Above its upper cut-off frequency, these orientations are due to the metallic boundary, which causes the oscillations of the received power by the antenna. The electric-field vectors for the case without the metallic caps (i.e., monopole + CRDR alone) at the same frequency maintain a polarization purity (unidirectional electric field vectors) implying radiation from the antenna.

Comprehensive radiation-pattern measurements depicting the E-plane (x-z plane) plots for all five cases of the proposed antenna with metallic cap loading is reported in figure 5.7. For each case, the radiation patterns at three different frequencies over the radiation band of the antenna (selected from the best-matched frequencies as revealed from the S_{11}) are compared. It is to be noted that for all cases the radiation pattern is monopole-type with a broadside null (with respect to ground plane of the antenna) and shows excellent correspondence with the simulated patterns. Figure 5.8 presents the maximum measured gain of the unloaded CRDR and CRDR with metallic caps (for two cases) in x-z plane as function of frequency. The plot reveals similar gains with and without metallic caps for a frequency range up to 14 GHz, in which the CRDR loaded with Cap 1 yields a peak gain of 5.08 dBi at 14.4 GHz with a roll-off beyond that frequency. The peak gain profile for the unloaded CRDR and CRDR with Cap 4 are almost identical over the whole frequency range yielding a peak gain of 6.05 dBi at 14.9 GHz. The gain roll-off for the CRDR with Cap 1 is consistent with the impedance bandwidth of the CRDR antenna, confirming that the metallic-cap loading establishes the bandwidth control functionality and may be optimized by designing the properties of the metallic cap.

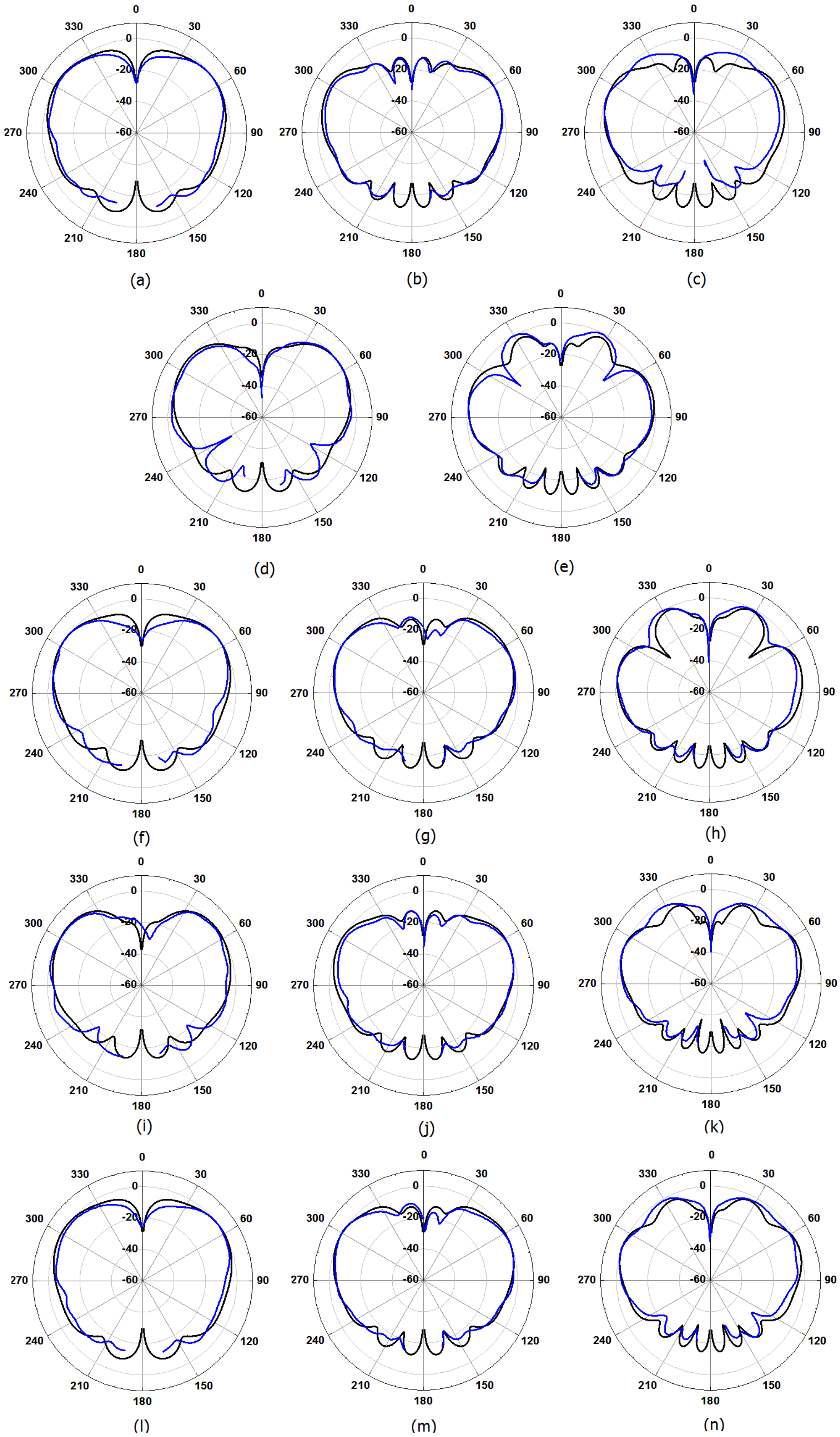

(a) (b) (c) (d) (e) (f) (g) (h) (i) (j) (k) (l) (m) (n)

Figure 5.7: Measured, simulated E-plane radiation patterns for the proposed metallic cap-loaded CRDR antenna for various configurations. (a)-(c) monopole and CRDR, (d)-(e) with Cap 1,(f)-(h) with Cap 2, (i)-(k) with Cap 3, (l)-(n) with Cap 4. Blue and black curves represent measured and simulated results, respectively.

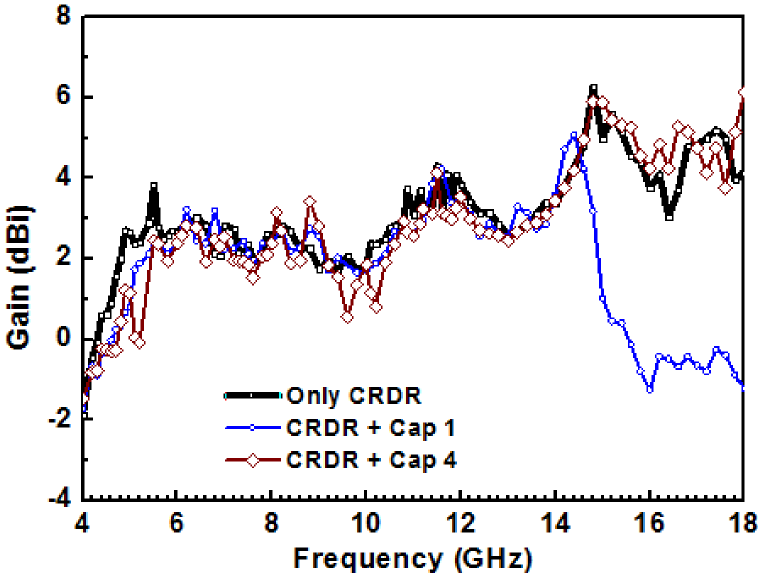

Figure 5.8: Measured peak gain of the monopole-excited CRDR antenna with and without metallic cap loading for various R_i.

5.3 Metallic-Sleeve loaded bandwidth controllability

In the second configuration, shown in figure 5.1(b), the outer surface of the CRDR is wrapped by a metallic sleeve of radius a, width w and height h_r and shorted to antenna ground plane. Simple copper tape with proper width is cut and fixed on the outer boundary of the CRDR to achieve different h_r values. It has been observed that varying h_r while maintaining all other antenna design parameters allows excellent bandwidth controllability. Detailed investigations of both types of loading of the CRDR antennas show that the bandwidth of the antenna can be controlled from 122% (for the unloaded case) to 26% for cylindrical sleeve loading. Six different heights of the metallic sleeve h_r = (0.8 mm, 1.4 mm, 2 mm, 2.4 mm, 2.8 mm and 4.4 mm) were investigated to explore the bandwidth controllability of the metallic-sleeve-loaded CRDR.

The corresponding S_{11} data depicted in figure 5.9, shows excellent bandwidth controllability over a wide spectrum when compared to the conventional monopole-fed CRDR. Figure 5.9(a) plots the magnitude of the reflection coefficient of the six cases of sleeve loading along with that of the unloaded case. It is revealed that for increasing h_r the upper cut-off frequency of the loaded antenna decreases

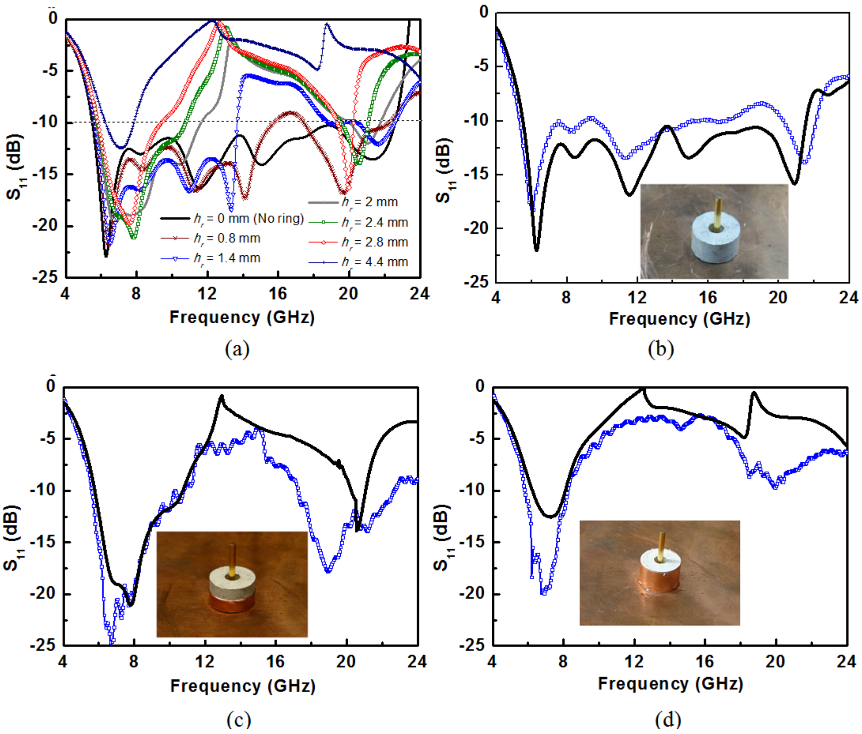

(a) (b)

(c) (d)

Figure 5.9: Measured and simulated S_{11} of monopole excited CRDR antenna with and without metallic sleeve loading for various sleeve heights, h_r (a)simulated for $h_r = 0$, 0.8, 1.4, 2, 2.4, 2.8 and 4.4 mm (b)-(d) simulated and measured for h_r =0, 2.4 and 4.4 mm, respectively. Solid and dotted lines indicate simulation and measurement respectively

drastically from 22.6 GHz to 7.95 GHz whereas the variation of lower cut-off frequency is much less, contributed by a small shift of the quarter-wave monopole resonance due to the loaded configuration. The significant decrease of the upper cut-off frequency and hence percentage bandwidth of the overall antenna is due to the increased inductance of the metallic sleeve and mutual capacitance between ground plane and metallic sleeve for increasing values of h_r. Figures 5.9(b)-(d) compare the measured and simulated S_{11} for $h_r = 0$ mm, 2.4 mm and 4.4 mm, respectively. The overall trend of the measured S_{11} matches that of the simulated plots with some deviation on the higher-frequency side where the effect of fabrication tolerances becomes dominant. Table 5.2 summarizes the achieved percentage bandwidths for various h_r revealing smooth controllability from 122% (for $h_r = 0$ mm) to 26% (for $h_r = 4.4$ mm) and intermediate values of 96% for $h_r = 0.8$ mm, 84% for $h_r = 1.4$ mm, 69% for $h_r = 2$ mm, 61% for $h_r = 2.4$ mm, 48% for $h_r = 2.8$

Table 5.2: Summary of the simulated and measured bandwidths for different metallic sleeve loaded CRDR antenna demonstrating bandwidth controllability. (Paramteric variables as in figure 5.1)

Antenna Type	Tools	f_l	f_u	% BW
Monopole + CRDR	Sim	5.5	22.65	122
	Meas	5.36	22.04	122
With Metallic Sleeve Loading (on outer surface of the CRDR)				
Monopole + CRDR + Sleeve 1 (h_r = 4.4 mm)	Sim	6.1	7.95	26
	Meas	5.8	8.2	34
Monopole + CRDR + Sleeve 2 (h_r = 2.8 mm)	Sim	5.8	9.45	48
Monopole + CRDR + Sleeve 3 (h_r = 2.4 mm)	Sim	5.75	10.75	61
	Meas	5.6	10.7	62
Monopole + CRDR + Sleeve 4 (h_r = 2 mm)	Sim	5.7	11.65	69
Monopole + CRDR + Sleeve 5 (h_r = 1.4 mm)	Sim	5.6	13.7	84
Monopole + CRDR + Sleeve 6 (h_r = 0.8 mm)	Sim	5.6	15.9	96

mm. The measured percentage bandwidth for three cases, $h_r = 0$ mm, $h_r = 2.4$ mm and $h_r = 4.4$ mm are 34%, 62% and 122% against simulated values of 26%, 61% and 122%, respectively.

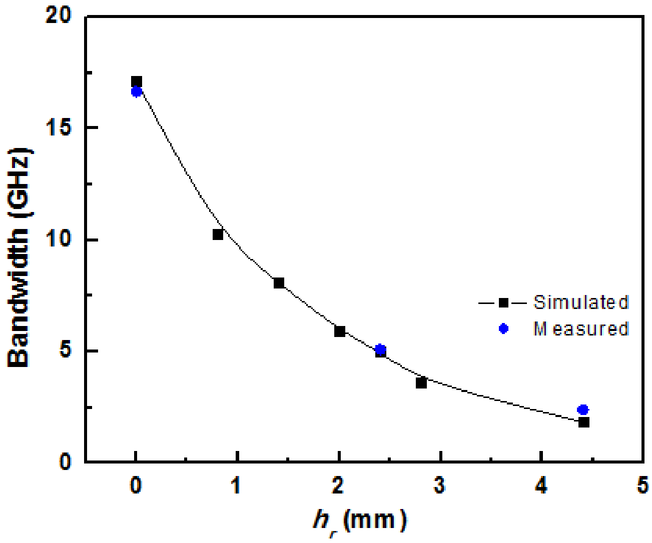

Figure 5.10: Simulated and measured bandwidth versus sleeve height for monopole-excited CRDR antenna with metallic-sleeve loading for various sleeve heights h_r.

Figure 5.10 shows the measured and simulated impedance BW plots of the proposed metallic-sleeve loaded CRDR antenna against sleeve height. As revealed from the plot, the bandwidth of the CRDR monotonically decreases from 17.12 GHz (unloaded case) to 1.86 GHz sleeve loading. The measured and simulated impedance BW demonstrate good correspondence. Using a curve-fitting technique, the bandwidth of the proposed metallic-sleeve-loaded antenna (BW_{SL}) can be expressed as,

$$BW_{SL} = BW_{UL}\left(1 - 3.6h_i + 11h_i^2 - 21h_i^3 + 19h_i^4 - 6.3h_i^5\right) for0 \leq h_i \leq 4.4 \tag{5.2}$$

where, $h_i = h_r/h$ is the normalized sleeve height.

The measured and simulated E-plane radiation patterns for the metallic-sleeve loaded CRDR configuration are shown in figure 5.11. These exhibit monopole-type radiation characteristics identical to those of the previous configurations with peak gains of around 3-5 dBi for three different prototypes as shown in the gain versus frequency plot of figure 5.12, for three different prototypes. Similar to the metallic-cap-loaded CRDR configuration, the gain of the metallic-sleeve-loaded CRDR antenna is identical to that of the unloaded case up to the matching bandwidth and rolls off beyond that.

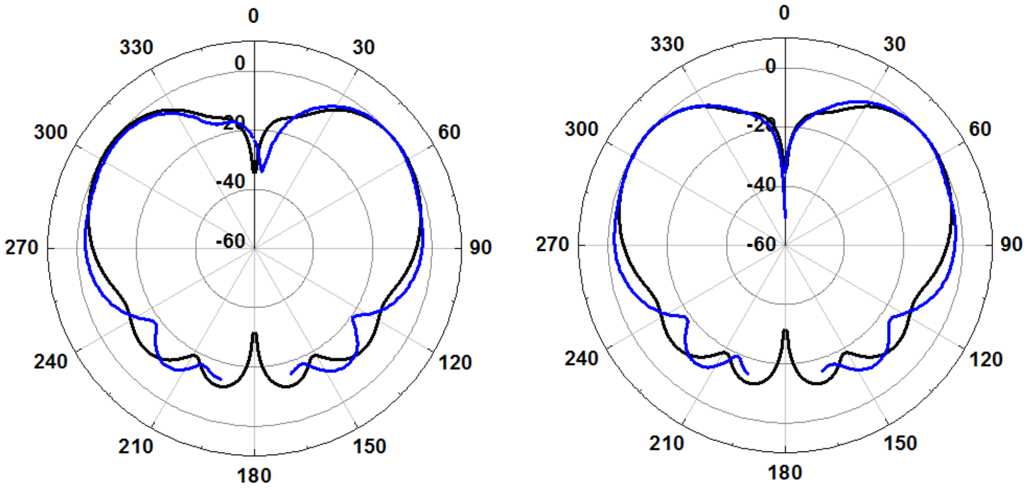

Figure 5.11: Measured and simulated E-plane (x-z) radiation patterns for metallic-sleeve loaded CRDR antenna for (a) for $h_r = 2.4$ mm and (b) $h_r = 4.4$ mm at 6.23 GHz. Solid and dotted line represents simulation and measurement respectively.

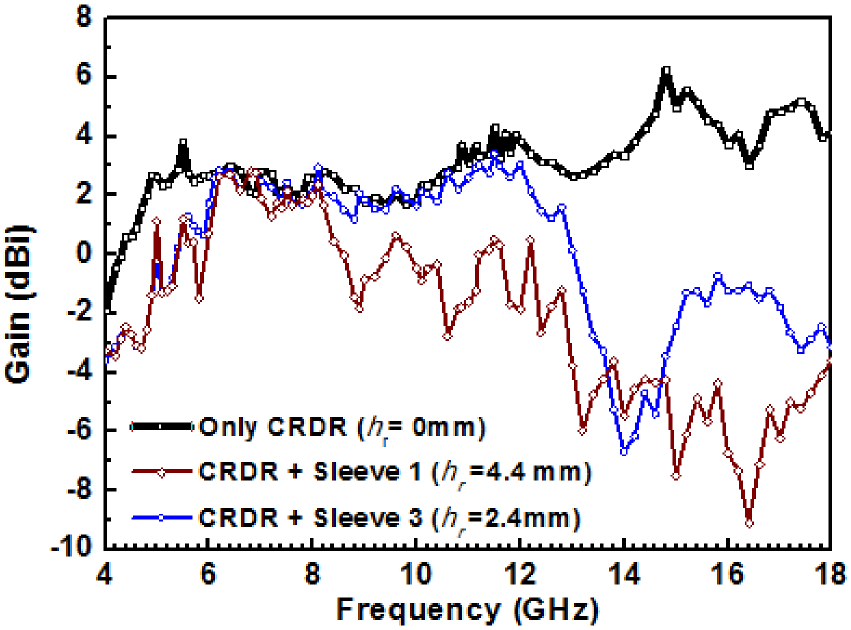

Figure 5.12: Measured peak gain of the monopole-excited CRDR antenna with and without metallic-sleeve loading for various h_r.

To have a more detailed insight into the proposed bandwidth-controllability mechanism, the radiation quality factor, Q_{rad}, of the antenna for the sleeve-loaded CRDR configuration is studied against the frequency of operation. Considering a unit input power of one watt, the conduction loss, Q_c, dielectric loss, Q_d and power radiated, P_{rad} at different frequencies are obtained using simulation to compute Q_{rad}. The overall Q, ignoring surface wave loss which is significantly low for the DRA, is expressed as,

$$Q = \omega \frac{EnergyStored}{Energylosspersecond} = \omega \frac{W_e + W_m}{P_c + P_d + P_{rad}} \tag{5.3}$$

where W_e and W_m are stored electric and magnetic energy respectively while P_c, P_d and P_{rad} indicate conduction, dielectric, and desired radiation loss, respectively. The conduction-loss quality factor (Q_c) and dielectric-loss quality factor (Q_d) are given as,

$$Q_c = \omega \frac{W_e + W_m}{P_c} Q_d = \omega \frac{W_e + W_m}{P_d} \tag{5.4}$$

The radiation quality factor Q_{rad} is expressed as,

$$Q_rad = \omega\frac{W_e + W_m}{P_{rad}} = \frac{Q_c P_c}{P_{rad}} = \frac{Q_d P_d}{P_{rad}} \tag{5.5}$$

To obtain Q_{rad} , P_c (or P_d) is calculated using

$$P_c + P_d = P_{acc} - P_{rad} = \left(1- \mid \Gamma \mid^2\right) P_{in} - P_{rad} = \left(1- \mid \Gamma \mid^2\right) - P_{rad} \tag{5.6}$$

where, $\mid \Gamma \mid$ is the reflection coefficient of the antenna, P_{acc} is the accepted power of the antenna and P_{rad} is the normalized radiated power of the antenna for , $P_{in} = 1$ watt as the input power and directly available from *CST*.
Solving 5.5 and 5.6, we get,

$$Q_{rad} = \frac{Q_c Q_d}{Q_c + Q_d}\left[\frac{1- \mid \Gamma \mid^2}{P_{rad}} - 1\right] \tag{5.7}$$

Figure 5.13 shows the plot of Q_{rad} against frequency for sleeve-loaded CRDRs with $h_r = 1.4$ mm, 2.4 mm and 4.4 mm, respectively. It can be observed from the

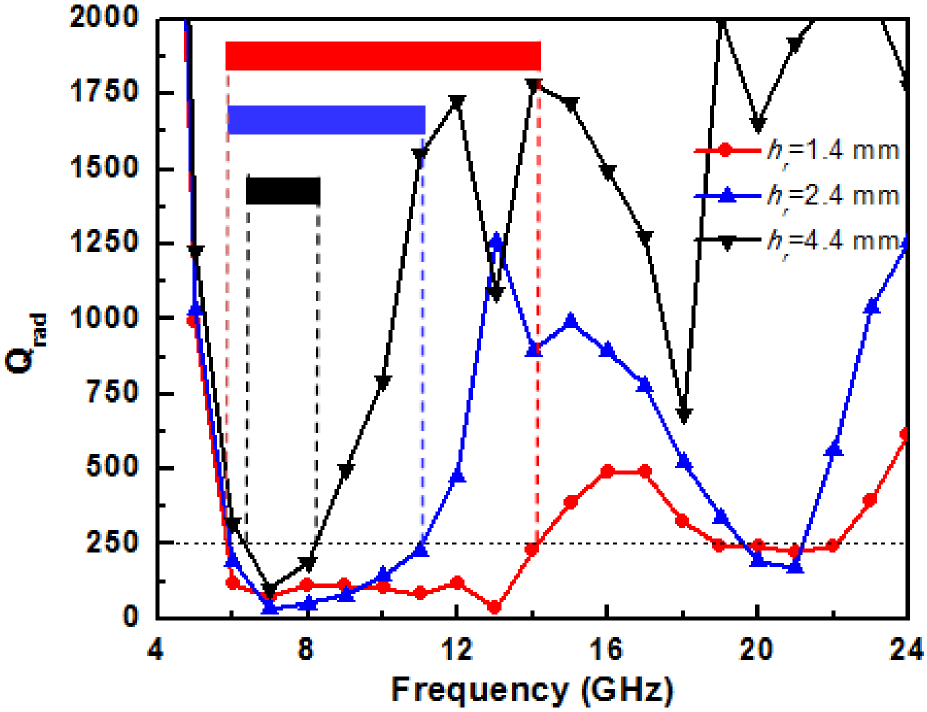

Figure 5.13: Radiation quality factor (Q_{rad}) versus frequency of the proposed monopole-excited CRDR antenna with metallic sleeve loading for various h_r of the sleeve.

plot that above the antenna's lower cut-off frequencies, Q_{rad} remains low until their upper cut-off frequencies and over-shoots the optimum Q value, set at $Q_{rad} = 250$, indicating very low radiated power above this cut-off frequency. This shift of upper cut-off frequency shifts towards the lower side with increasing sleeve height indicates controllability of the bandwidth of the antenna.

5.4 Conclusion

A new technique employing metallic-cap and sleeve loading on a CRDR antenna has been proposed to control its impedance bandwidth. Curve-fitted equations proposed for the bandwidth control technique can be used as a design guideline to achieve a desired impedance bandwidth. The proposed technique is simple to implement from a design and fabrication standpoint, provides a wide frequency range of control, and is achieved without significantly perturbing the radiation characteristics of the antenna.

CHAPTER 6

Conclusion

6.1 Conclusion

In this thesis, the multi-functional printed antennas and bandwidth controllable dielectric resonator antennas has been investigated. Multi-functional antennas are realized with combinatorial loading of SRR and shunt strips in the feed section of the printed antenna. With axial magnetic field excitation of SRR, it inhibits the signal propagation in the vicinity of the resonance frequency of the SRR leading to band stop characteristics. Additionally, loading the SRR loaded transmission line with shunt strip complements the functionality. These characteristics has been exploited to realise the multi-functional antennas. The bandwidth controllable dielectric resonator antenna is realized by mechanically loading the antenna with metallic structures.

In **chapter 2**, the approach of inhibiting the signal propagation in the vicinity of resonance frequency of SRR has been capitalized to realise multiband and wideband bandstop filters. An additional tuning parameter, angular orientation of inner ring θ, compared to conventional SRR is utilized to demonstrate the filters. The theoretical calculation to calculate the resonance frequency of rotational SRR is derived. These designs has been modelled and validated through theoretical calculations, EM simulators, lumped element equivalent model and the measurement. The filters modelled by loading the transmission line with SRR is further utilised to realize ‘filtenna’ which is combination of filter and antenna.

In **chapter 3**, a multi-functional antenna is designed by loading the UWB monopole antenna with SRRs and/or shunt strips on the feed region of the antenna. To demonstrate the design flexibity, the technique of achieving multi-functional characteristics is applied to two different radiators, namely, circular monopole antenna and tapered slot antenna. In modelling the multi-functional antenna with multiple notches the lateral dimension of the antenna increases to accommodate multiple SRR and hence to maintain compactness a superstrate is utilized thereby creating two surfaces available for SRR placement and reducing the lateral dimensions.

The multi-functional antennas demonstrated in Chapter 3 are potential candidates as antennas for cognitive radio applications if the multi-functionality is realized by proper switching. To achieve this dynamic reconfigurability, electrical and mechanical techniques are employed on the antenna. **chapter 4** deals with this practical realization of multi-functionality in detail. The shunt strip is replaced by PIN diode, thereby providing the electronic reconfigurability with the application of proper bias. The mechanical reconfigurability is further demonstrated using motor controlled by microcontroller where the superstrate is moved with respect to the antenna.

In **chapter 5**, the bandwidth of the dielectric resonator antenna is controlled by loading the antenna with metallic structures. The higher cut-off frequency of a popular hybrid dielectric resonator antenna is tuned using two different kinds of parasitic loading on the antenna. Proposed technique is extremely effective in controlling the bandwidth of the antenna over a wide-range.

6.2 Recommendations for Future Scope

1. A more accurate electromagnetic model for calculation of resonance frequency of SRR can be developed. This is highly important as SRRs are inherently high Q-structure which demands high accuracy in resonance frequency calculation.

2. Study on the effect of the resonance frequency when incorporated in any transmission line structure compared to isolated SRR can be a carried out.

3. Extending the current antenna topology for cognitive radio applications by sensing the environment and responding accordingly to the requirements.

4. The concept of tunability of the notch position or the narrowband can be extended to antenna applications, where the tunability can be obtained by means of varactor.
5. The tunability of the notch or the narrowband can be attained with the help of RF-MEMS switches. The design of the antenna and the RF-MEMS switch can be of same substrate to alleviate the integration complexities.
6. Extensive study of the modes in the CRDR can be carried out to control the bandwidth more efficiently.

REFERENCES

1. Abbas, S. M., Ranga, Y., Verma, A. K., and Esselle, K. P. (2014). A simple ultra wideband printed monopole antenna with high band rejection and wide radiation patterns. *IEEE transactions on antennas and propagation*, *62*, 4816 4820.

2. Agilent, A. (2015). Agilent technologies, santa rosa, ca, usa.

3. Alexiou, A., and Haardt, M. (2004). Smart antenna technologies for future wireless systems: trends and challenges. *IEEE communications Magazine*, *42*, 90 97.

4. ANSYS, H. (2015). Ansys corp. software, pittsburgh, pa, usa.

5. Antoniades, M. A., and Eleftheriades, G. V. (2005). A broadband series power divider using zero-degree metamaterial phase-shifting lines. *IEEE Microwave and Wireless Components Letters*, *15*, 808 810.

6. Apperley, T., and Okoniewski, M. (2014). An air-gap-based frequency switching method for the dielectric resonator antenna. *IEEE Antennas and Wireless Propagation Letters*, *13*, 455 458.

7. Arnedo, I., Illescas, J., Flores, M., Lopetegi, T., Laso, M., Falcone, F., Bonache, J., Garcia-Garcia, J., Martin, F., Marcotegui, J. et al. (2007). Forward and backward leaky wave radiation in split-ring-resonator-based metamaterials. *IET microwaves, antennas & propagation*, *1*, 65 68.

8. Augustin, G., and Denidni, T. A. (2012). An integrated ultra wideband/narrow band antenna in uniplanar configuration for cognitive radio systems. *IEEE Transactions on antennas and propagation*, *60*, 5479 5484.

9. Bahl, I. J., and Bhartia, P. (2003). *Microwave solid state circuit design.* John Wiley & Sons.

10. Behdad, N., and Sarabandi, K. (2006). A varactor-tuned dual-band slot antenna. *IEEE Transactions on Antennas and Propagation*, *54*, 401 408.

11. Bernhard, J. T. (2007). Reconfigurable antennas. *Synthesis lectures on antennas*, *2*, 1 66.

12. Bonache, J., Gil, I., Garcia-Garcia, J., and Martin, F. (2006). Novel microstrip bandpass filters based on complementary split-ring resonators. *IEEE Transactions on Microwave Theory and Techniques*, *54*, 265 271.

13. Buerkle, A., Sarabandi, K., and Mosallaei, H. (2005). Compact slot and dielectric resonator antenna with dual-resonance, broadband characteristics. *IEEE Transactions on Antennas and Propagation*, *53*, 1020 1027.

14. Chacko, B. P., Augustin, G., and Denidni, T. A. (2013). A high-gain antenna based on zero-index metamaterial superstrate. In *Antennas and Propagation Society International Symposium (APSURSI), 2013 IEEE* (pp. 122 123). IEEE.

15. Chang, T.-H., and Kiang, J.-F. (2007). Broadband dielectric resonator antenna with metal coating. *IEEE transactions on antennas and propagation*, *55*, 1254 1259.

16. Chiu, L., Yum, T., Xue, Q., and Chan, C. (2004). A low-conversion-loss ring-hybrid mixer using ts-cmrc circuitry. *Microwave and Optical Technology Letters*, *41*, 206 209.

17. Christodoulou, C. G. (2009). Cognitive radio: the new frontier for antenna design. *IEEE Antennas Propag. Soc. Feature Artic*, .

18. Christodoulou, C. G., Tawk, Y., Lane, S. A., and Erwin, S. R. (2012). Reconfigurable antennas for wireless and space applications. *Proceedings of the IEEE*, *100*, 2250 2261.

19. Chu, Q.-X., and Yang, Y.-Y. (2008). A compact ultrawideband antenna with 3.4/5.5 ghz dual band-notched characteristics. *IEEE transactions on antennas and propagation*, *56*, 3637 3644.

20. Constantine, A. B. et al. (2005). Antenna theory: analysis and design. *MICROSTRIP ANTENNAS, third edition, John wiley & sons*, .

21. Costantine, J., Tawk, Y., and Christodoulou, C. G. (2013). Motion-activated reconfigurable and cognitive radio antenna systems. *IEEE Antennas and Wireless Propagation Letters*, *12*, 1114 1117.

22. Costantine, J., Tawk, Y., Woodland, J., Flaum, N., and Christodoulou, C. G. (2014). Reconfigurable antenna system with a movable ground plane for cognitive radio. *IET Microwaves, Antennas & Propagation*, *8*, 858 863.

23. Danesh, S., Rahim, S., Abedian, M., and Yusof, M. (2014). Frequency reconfigurable rectangular ring dielectric resonator antenna. In *Wireless Technology and Applications (ISWTA), 2014 IEEE Symposium on* (pp. 156 159). IEEE.

24. Desjardins, J., McNamara, D., Thirakoune, S., and Petosa, A. (2012). Electronically frequency-reconfigurable rectangular dielectric resonator antennas. *IEEE Transactions on Antennas and Propagation*, *60*, 2997 3002.

25. Ebrahimi, E., Kelly, J. R., and Hall, P. S. (2011). Integrated wide-narrowband antenna for multi-standard radio. *IEEE transactions on antennas and propagation*, *59*, 2628 2635.

26. Erdil, E., Topalli, K., Unlu, M., Civi, O. A., and Akin, T. (2007). Frequency tunable microstrip patch antenna using rf mems technology. *IEEE transactions on antennas and propagation*, *55*, 1193 1196.

27. Erfani, E., Nourinia, J., Ghobadi, C., Niroo-Jazi, M., and Denidni, T. A. (2012). Design and implementation of an integrated uwb/reconfigurable-slot antenna for cognitive radio applications. *IEEE Antennas and Wireless Propagation Letters*, *11*, 77 80.

28. Esselle, K. P., and Bird, T. S. (2005). A hybrid-resonator antenna: Experimental results. *IEEE Transactions on Antennas and Propagation*, *53*, 870 871.

29. Force, F. S. P. T. (2002). Report of the spectrum efficiency working group. *http://www. fcc. gov/sptf/reports. html*, .

30. Garg, R., Bahl, I., and Bozzi, M. (2013). *Microstrip lines and slotlines*. Artech house.

31. Ghosh, S., and Chakrabarty, A. (2008). Ultrawideband performance of dielectric loaded t-shaped monopole transmit and receive antenna/emi sensor. *IEEE Antennas and Wireless Propagation Letters*, *7*, 358 361.

32. Gil, M., Bonache, J., Selga, J., Garcia-Garcia, J., and Martin, F. (2007). High-pass filters implemented by composite right/left handed (crlh) transmission lines based on complementary split rings resonators (csrrs). *PIERS online*, *3*, 251 253.

33. Grover, F. W. (2004). *Inductance calculations: working formulas and tables*. Courier Corporation.

34. Guha, D., Banerjee, A., Kumar, C., and Antar, Y. M. (2012). Higher order mode excitation for high-gain broadside radiation from cylindrical dielectric resonator antennas. *IEEE Transactions on Antennas and Propagation*, *60*, 71 77.

35. Guha, D., Banerjee, A., Kumar, C., Antar, Y. M., and Sebastian, M. (2014a). Design guidelines for the cylindrical dielectric resonator antenna using the recently proposed hem12d mode [antenna designer's notebook]. *IEEE Antennas and Propagation Magazine*, *56*, 148 158.

36. Guha, D., Ganguly, D., George, S., and Antar, Y. M. (2014b). Monopole-type dielectric resonator antenna with improved bandwidth characteristics. In *Antennas and Propagation Society International Symposium (APSURSI), 2014 IEEE* (pp. 1988 1989). IEEE.

37. Guha, D., Gupta, B., and Antar, Y. M. (2009). New pawn-shaped dielectric ring resonator loaded hybrid monopole antenna for improved ultrawide bandwidth. *IEEE antennas and wireless propagation letters*, *8*, 1178 1181.

38. Hady, L. K., Kishk, A. A., and Kajfez, D. (2009). Dual-band compact dra with circular and monopole-like linear polarizations as a concept for gps and wlan applications. *IEEE transactions on antennas and propagation*, *57*, 2591 2598.

39. Hall, P. S., Gardner, P., and Faraone, A. (2012). Antenna requirements for software defined and cognitive radios. *Proceedings of the IEEE*, *100*, 2262 2270.

40. Han, T.-Y., Liao, Y.-J. et al. (2014). A frequency reconfigurable half annular ring slot antenna design. *IEEE Transactions on Antennas and Propagation*, *62*, 3428 3431.

41. Hinsz, L., and Braaten, B. D. (2014). A frequency reconfigurable transmitter antenna with autonomous switching capabilities. *IEEE Transactions on antennas and propagation*, *62*, 3809 3813.

42. Hsiao, F.-R., Wang, C., Wong, K.-L., and Chiou, T.-W. (2002a). Broadband very-high-permittivity dielectric resonator antenna for wlan application. In *Antennas and Propagation Society International Symposium, 2002. IEEE* (pp. 490 493). IEEE volume 4.

43. Hsiao, F.-R., Wang, C., Wong, K.-L., and Chiou, T.-W. (2002b). Broadband very-high-permittivity dielectric resonator antenna for wlan application. In *Antennas and Propagation Society International Symposium, 2002. IEEE* (pp. 490 493). IEEE volume 4.

44. Huang, C.-Y., Wu, J.-Y., and Wong, K.-L. (1999). Cross-slot-coupled microstrip antenna and dielectric resonator antenna for circular polarization. *IEEE Transactions on Antennas and Propagation*, *47*, 605 609.

45. Huff, G. H., and Bernhard, J. T. (2006). Integration of packaged rf mems switches with radiation pattern reconfigurable square spiral microstrip antennas. *IEEE Transactions on Antennas and Propagation*, *54*, 464 469.

46. Huitema, L., Koubeissi, M., Mouhamadou, M., Arnaud, E., Decroze, C., and Monediere, T. (2011). Compact and multiband dielectric resonator antenna with pattern diversity for multistandard mobile handheld devices. *IEEE Transactions on antennas and propagation*, *59*, 4201 4208.

47. Hussain, R., and Sharawi, M. S. (2015). Integrated reconfigurable multiple-input multiple-output antenna system with an ultra-wideband sensing antenna for cognitive radio platforms. *IET Microwaves, Antennas & Propagation*, *9*, 940 947.

48. Ittipiboon, A., Petosa, A., Roscoe, D., and Cuhaci, M. (1996). An investigation of a novel broadband dielectric resonator antenna. In *Antennas and Propagation Society International Symposium, 1996. AP-S. Digest* (pp. 2038 2041). IEEE volume 3.

49. Jiang, D., Xu, Y., Xu, R., and Lin, W. (2012). Compact dual-band-notched uwb planar monopole antenna with modified csrr. *Electronics Letters*, *48*, 1250 1252.

50. won Jung, C., Lee, M.-j., Li, G., and De Flaviis, F. (2006). Reconfigurable scan-beam single-arm spiral antenna integrated with rf-mems switches. *IEEE Transactions on antennas and propagation*, *54*, 455 463.

51. Kishk, A. A. (2003). Wide-band truncated tetrahedron dielectric resonator antenna excited by a coaxial probe. *IEEE Transactions on Antennas and Propagation*, *51*, 2913 2917.

52. Kishk, A. A., Yin, Y., and Glisson, A. W. (2002). Conical dielectric resonator antennas for wide-band applications. *IEEE Transactions on Antennas and Propagation*, *50*, 469 474.

53. Kumar, G., and Ray, K. (2003). *Broadband microstrip antennas*. Artech House.

54. Lan, K., Chaudhuri, S., and Safavi-Naeini, S. (2003). A compact wide-dual-band antenna for bluetooth and wireless lan applications. In *Antennas and Propagation Society International Symposium, 2003. IEEE* (pp. 926 929). IEEE volume 2.

55. Lapierre, M., Antar, Y. M., Ittipiboon, A., and Petosa, A. (2005). Ultra wideband monopole/dielectric resonator antenna. *IEEE Microwave and Wireless Components Letters*, *15*, 7 9.

56. Leung, K., Chow, K., and Luk, K. (2003). Low-profile high-permittivity dielectric resonator antenna excited by a disk-loaded coaxial aperture. *IEEE antennas and wireless propagation letters*, *2*, 212 214.

57. Leung, K., and So, K. (2005). Frequency-tunable designs of the linearly and circularly polarized dielectric resonator antennas using a parasitic slot. *IEEE Transactions on Antennas and Propagation*, *53*, 572 578.

58. Li, Z., Wu, C., and Litva, J. (1996). Adjustable frequency dielectric resonator antenna. *Electronics letters*, *32*, 606 607.

59. Liang, J., Chiau, C. C., Chen, X., and Parini, C. G. (2005). Study of a printed circular disc monopole antenna for uwb systems. *IEEE transactions on antennas and propagation*, *53*, 3500 3504.

60. Lim, S., Caloz, C., and Itoh, T. (2004). Electronically scanned composite right/left handed microstrip leaky-wave antenna. *IEEE Microwave and Wireless Components Letters*, *14*, 277 279.

61. Lin, C.-C., Jin, P., and Ziolkowski, R. W. (2012). Single, dual and tri-band-notched ultrawideband (uwb) antennas using capacitively loaded loop (cll) resonators. *IEEE Transactions on Antennas and Propagation*, *60*, 102 109.

62. Liu, H.-W., Ku, C.-H., Wang, T.-S., and Yang, C.-F. (2010). Compact monopole antenna with band-notched characteristic for uwb applications. *IEEE Antennas and Wireless Propagation Letters*, *9*, 397 400.

63. Liu, J., Esselle, K. P., Hay, S. G., and Zhong, S. (2011). Achieving ratio bandwidth of 25: 1 from a printed antenna using a tapered semi-ring feed. *IEEE Antennas and Wireless Propagation Letters*, *10*, 1333 1336.

64. Liu, L., Caloz, C., and Itoh, T. (2002). Dominant mode leaky-wave antenna with backfire-to-endfire scanning capability. *Electronics Letters*, *38*, 1414 1416.

65. Liu, L., and Langley, R. (2008). Liquid crystal tunable microstrip patch antenna. *Electronics Letters*, *44*, 1179 1180.

66. Long, S., McAllister, M., and Shen, L. (1983). The resonant cylindrical dielectric cavity antenna. *IEEE Transactions on Antennas and Propagation*, *31*, 406 412.

67. Luo, L., Cui, Z., Xiong, J.-P., Zhang, X.-M., and Jiao, Y.-C. (2008). Compact printed ultra-wideband monopole antenna with dual band-notch characteristic. *Electronics Letters*, *44*, 1106 1107.

68. Marqués, R., Martén, F., Sorolla, M. et al. (2011). *Metamaterials with negative parameters: theory, design, and microwave applications* volume 183. John Wiley & Sons.

69. Martin, F., Falcone, F., Bonache, J., Marques, R., and Sorolla, M. (2003). Miniaturized coplanar waveguide stop band filters based on multiple tuned split ring resonators. *IEEE Microwave and Wireless Components Letters*, *13*, 511 513.

70. Mitra, D., Haque, S. M., and Ghosh, B. (2009). Metal loaded miniaturized cpw fed dra. In *Applied Electromagnetics Conference (AEMC), 2009* (pp. 1 3). IEEE.

71. Mongia, R., Ittibipoon, A., and Cuhaci, M. (1994). Low profile dielectric resonator antennas using a very high permittivity material. *Electronics letters*, *30*, 1362 1363.

72. Ng, H. K., and Leung, K. W. (2006). Frequency tuning of the linearly and circularly polarized dielectric resonator antennas using multiple parasitic strips. *IEEE transactions on antennas and propagation*, *54*, 225 230.

73. Nguyen, D. T., Lee, D. H., and Park, H. C. (2012). Very compact printed triple band-notched uwb antenna with quarter-wavelength slots. *IEEE Antennas and Wireless Propagation Letters*, *11*, 411–414.

74. Ojaroudi, N., Ojaroudi, M., and Ghadimi, N. (2013). Dual band-notched small monopole antenna with novel w-shaped conductor backed-plane and novel t-shaped slot for uwb applications. *IET Microwaves, Antennas & Propagation*, *7*, 8–14.

75. Panagamuwa, C. J., Chauraya, A., and Vardaxoglou, J. (2006). Frequency and beam reconfigurable antenna using photoconducting switches. *IEEE Transactions on Antennas and Propagation*, *54*, 449–454.

76. Pendry, J. B., Holden, A. J., Robbins, D. J., and Stewart, W. (1999). Magnetism from conductors and enhanced nonlinear phenomena. *IEEE transactions on microwave theory and techniques*, *47*, 2075–2084.

77. Peroulis, D., Sarabandi, K., and Katehi, L. P. (2005). Design of reconfigurable slot antennas. *IEEE Transactions on Antennas and Propagation*, *53*, 645–654.

78. Petosa, A. (2007). *Dielectric resonator antenna handbook*. Artech House Publishers.

79. Petosa, A., and Ittipiboon, A. (2010). Dielectric resonator antennas: A historical review and the current state of the art. *IEEE Antennas and Propagation magazine*, *52*, 91–116.

80. Petosa, A., Mongia, R., Ittipiboon, A., and Wight, J. (1995). Switchable lp/cp ferrite disk resonator antenna. *Electronics Letters*, *31*, 148–149.

81. Pourush, R., Tyagi, G., Srivastava, G., and Pourush, P. (2006). Radiation performance of switchable ferrite microstrip array antenna. *IEEE Antennas and Wireless Propagation Letters*, *5*, 195–198.

82. Rao, Q., Denidni, T. A., and Sebak, A. R. (2005). A hybrid resonator antenna suitable for wireless communication applications at 1.9 and 2.45 ghz. *IEEE Antennas and Wireless Propagation Letters*, *4*, 341–343.

83. Row, J.-S., Liu, W.-L., and Chen, T.-R. (2012). Circular polarization and polarization reconfigurable designs for annular slot antennas. *IEEE Transactions on Antennas and Propagation*, *60*, 5998 6002.

84. Ryu, K. S., and Kishk, A. A. (2011). Uwb dielectric resonator antenna having consistent omnidirectional pattern and low cross-polarization characteristics. *IEEE Transactions on Antennas and Propagation*, *59*, 1403 1408.

85. Saadoun, M. M., and Engheta, N. (1992). A reciprocal phase shifter using novel pseudochiral or ω medium. *Microwave and optical technology letters*, *5*, 184 188.

86. Saha, C., and Siddiqui, J. Y. (2011). A comparative analyis for split ring resonators of different geometrical shapes. In *Applied Electromagnetics Conference (AEMC), 2011 IEEE* (pp. 1 4). IEEE.

87. Saha, C., and Siddiqui, J. Y. (2012). Theoretical model for estimation of resonance frequency of rotational circular split-ring resonators. *Electromagnetics*, *32*, 345 355.

88. Saha, C., Siddiqui, J. Y., Shaik, L. A., and Antar, Y. M. (2015). Rotational circular split ring resonator array loaded cpw for dual notch and wide bandstop applications. *Microwave and Optical Technology Letters*, *57*, 1204 1209.

89. Sathi, V., Ehteshami, N., and Nourinia, J. (2012). Optically tuned frequency-reconfigurable microstrip antenna. *IEEE Antennas and Wireless Propagation Letters*, *11*, 1018 1020.

90. Schantz, H. (2005). The art and science of uwb antennas. *Artech House*, .

91. Schelkunoff, S. A., and Friis, H. T. (1952). *Antennas: theory and practice* volume 639. Wiley New York.

92. Shelley, S., Costantine, J., Christodoulou, C. G., Anagnostou, D. E., and Lyke, J. C. (2010). Fpga-controlled switch-reconfigured antenna. *IEEE Antennas and Wireless Propagation Letters*, *9*, 355 358.

93. Siddiqui, J. Y., Saha, C., and Antar, Y. M. (2014). Compact srr loaded uwb circular monopole antenna with frequency notch characteristics. *IEEE Transactions on Antennas and Propagation*, *62*, 4015 4020.

94. Siddiqui, J. Y., Saha, C., and Antar, Y. M. (2015). A novel ultrawideband (uwb) printed antenna with a dual complementary characteristic. *IEEE Antennas and Wireless Propagation Letters*, *14*, 974 977.

95. Simons, R. N. (2001). *Microstrip lines and slotlines*. John Wiley & Sons.

96. Smith, D. R., Padilla, W. J., Vier, D., Nemat-Nasser, S. C., and Schultz, S. (2000). Composite medium with simultaneously negative permeability and permittivity. *Physical review letters*, *84*, 4184.

97. So, K. K., Wong, H., Ng, K. B., and Luk, K. M. (2011). Dielectric resonator antenna for millimeter wave applications. In *Antenna Technology (iWAT), 2011 International Workshop on* (pp. 324 327). IEEE.

98. Sung, Y. (2013). Triple band-notched uwb planar monopole antenna using a modified h-shaped resonator. *IEEE Transactions on Antennas and Propagation*, *61*, 953 957.

99. Tang, M.-C., Wang, H., Deng, T., and Ziolkowski, R. W. (2016). Compact planar ultrawideband antennas with continuously tunable, independent band-notched filters. *IEEE Transactions on Antennas and Propagation*, *64*, 3292 3301.

100. Tang, M.-C., Wen, Z., Wang, H., Li, M., and Ziolkowski, R. W. (2017). Compact, frequency-reconfigurable filtenna with sharply defined wideband and continuously tunable narrowband states. *IEEE Transactions on Antennas and Propagation*, *65*, 5026 5034.

101. Tawk, Y., and Christodoulou, C. (2009). A new reconfigurable antenna design for cognitive radio. *IEEE Antennas and wireless propagation letters*, *8*, 1378 1381.

102. Tawk, Y., Costantine, J., Avery, K., and Christodoulou, C. (2011). Implementation of a cognitive radio front-end using rotatable controlled reconfigurable antennas. *IEEE Transactions on Antennas and Propagation*, *59*, 1773 1778.

103. Tawk, Y., Costantine, J., and Christodoulou, C. (2012a). A varactor-based reconfigurable filtenna. *IEEE Antennas and wireless propagation letters*, *11*, 716 719.

104. Tawk, Y., Costantine, J., and Christodoulou, C. (2014a). Cognitive-radio and antenna functionalities: A tutorial [wireless corner]. *IEEE Antennas and Propagation Magazine*, *56*, 231 243.

105. Tawk, Y., Costantine, J., and Christodoulou, C. (2016). *Antenna design for cognitive radio*. Artech House.

106. Tawk, Y., Costantine, J., and Christodoulou, C. G. (2014b). Reconfigurable filtennas and mimo in cognitive radio applications. *IEEE Transactions on Antennas and Propagation*, *62*, 1074 1083.

107. Tawk, Y., Costantine, J., Hemmady, S., Balakrishnan, G., Avery, K., and Christodoulou, C. G. (2012b). Demonstration of a cognitive radio front end using an optically pumped reconfigurable antenna system (opras). *IEEE Transactions on Antennas and Propagation*, *60*, 1075 1083.

108. Terman, F. E. (1943). *Radio engineers' handbook*. McGraw-Hill Book,.

109. Valderas, D. (2011). *Ultrawideband antennas: design and applications*. World Scientific.

110. White, C. R., and Rebeiz, G. M. (2009). Single-and dual-polarized tunable slot-ring antennas. *IEEE Transactions on Antennas and Propagation*, *57*, 19 26.

111. Xue, Q., Shum, K. M., and Chan, C. H. (2001). Novel oscillator incorporating a compact microstrip resonant cell. *IEEE Microwave and Wireless Components Letters*, *11*, 202 204.

112. Yum, T. Y., Xue, Q., and Chan, C. H. (2004). Amplifier linearization using compact microstrip resonant cell-theory and experiment. *IEEE transactions on microwave theory and techniques*, *52*, 927 934.

113. Zhang, H., Zhou, R., Wu, Z., Xin, H., and Ziolkowski, R. W. (2010). Designs of ultra wideband (uwb) printed elliptical monopole antennas with slots. *Microwave and Optical Technology Letters*, *52*, 466 471.

114. Zhang, Y., Hong, W., Yu, C., Kuai, Z.-Q., Don, Y.-D., and Zhou, J.-Y. (2008). Planar ultrawideband antennas with multiple notched bands based on etched slots on the patch and/or split ring resonators on the feed line. *IEEE Transactions on Antennas and Propagation*, *56*, 3063 3068.

115. Zou, L., Abbott, D., and Fumeaux, C. (2012). Omnidirectional cylindrical dielectric resonator antenna with dual polarization. *IEEE Antennas and Wireless Propagation Letters*, *11*, 515 518.

116. Zou, L., and Fumeaux, C. (2011). A cross-shaped dielectric resonator antenna for multifunction and polarization diversity applications. *IEEE Antennas and Wireless Propagation Letters*, *10*, 742 745.

APPENDIX A

Discrete Motion of Servo Motor

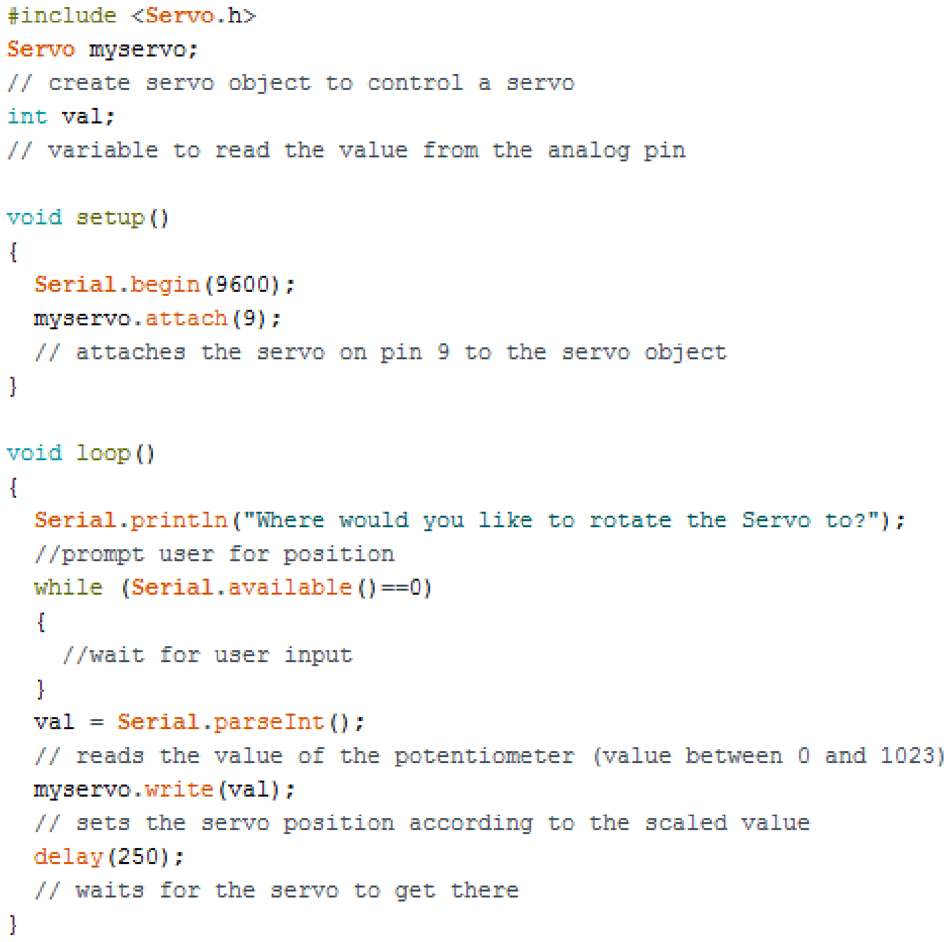

```
#include <Servo.h>
Servo myservo;
// create servo object to control a servo
int val;
// variable to read the value from the analog pin

void setup()
{
  Serial.begin(9600);
  myservo.attach(9);
  // attaches the servo on pin 9 to the servo object
}

void loop()
{
  Serial.println("Where would you like to rotate the Servo to?");
  //prompt user for position
  while (Serial.available()==0)
  {
    //wait for user input
  }
  val = Serial.parseInt();
  // reads the value of the potentiometer (value between 0 and 1023)
  myservo.write(val);
  // sets the servo position according to the scaled value
  delay(250);
  // waits for the servo to get there
}
```

APPENDIX B

Continuous Motion of Servo Motor

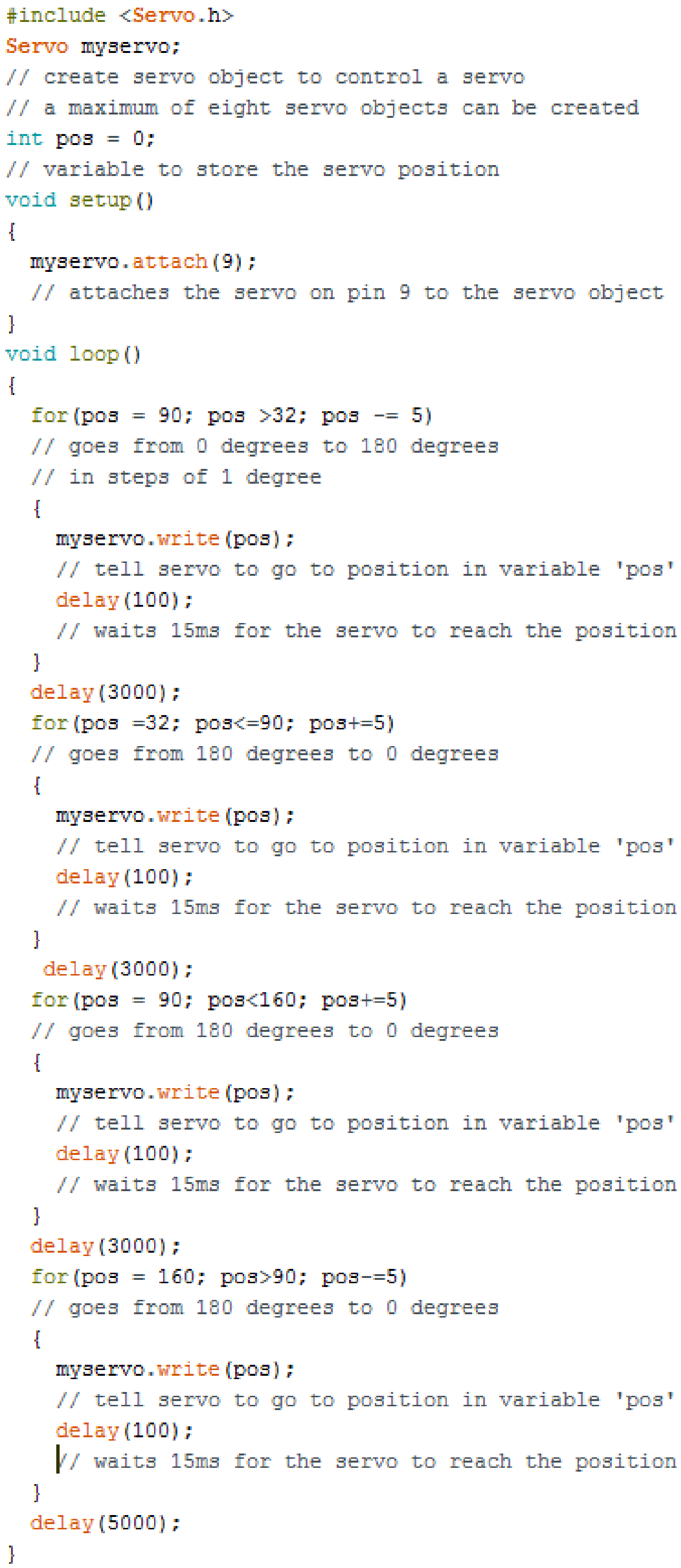

```
#include <Servo.h>
Servo myservo;
// create servo object to control a servo
// a maximum of eight servo objects can be created
int pos = 0;
// variable to store the servo position
void setup()
{
  myservo.attach(9);
  // attaches the servo on pin 9 to the servo object
}
void loop()
{
  for(pos = 90; pos >32; pos -= 5)
  // goes from 0 degrees to 180 degrees
  // in steps of 1 degree
  {
    myservo.write(pos);
    // tell servo to go to position in variable 'pos'
    delay(100);
    // waits 15ms for the servo to reach the position
  }
  delay(3000);
  for(pos =32; pos<=90; pos+=5)
  // goes from 180 degrees to 0 degrees
  {
    myservo.write(pos);
    // tell servo to go to position in variable 'pos'
    delay(100);
    // waits 15ms for the servo to reach the position
  }
   delay(3000);
  for(pos = 90; pos<160; pos+=5)
  // goes from 180 degrees to 0 degrees
  {
    myservo.write(pos);
    // tell servo to go to position in variable 'pos'
    delay(100);
    // waits 15ms for the servo to reach the position
  }
  delay(3000);
  for(pos = 160; pos>90; pos-=5)
  // goes from 180 degrees to 0 degrees
  {
    myservo.write(pos);
    // tell servo to go to position in variable 'pos'
    delay(100);
    // waits 15ms for the servo to reach the position
  }
  delay(5000);
}
```

LIST OF PAPERS BASED ON THESIS

Papers in Refereed Journals

1. Chinmoy Saha, **Latheef A. Shaik**, Rajesh Muntha, Y. M. M. Antar, and Jawad Y. Siddiqui, “A Dual Reconfigurable Printed Antenna: Design Concept and Experimental Realization” *IEEE Antennas and Propagation Magazine*, **to appear, 2018**.

2. **Latheef A. Shaik**, Chinmoy Saha, Y. M. M. Antar, and Jawad Y. Siddiqui, “An Antenna Advance for Cognitive Radio: Introducing a Multilayered Split Ring Resonator-Loaded Printed Ultrawideband Antenna with Multifunctional Characteristics,” *IEEE Antennas and Propagation Magazine*, **60(2):20-33, 2018**.

3. **Latheef A. Shaik**, Chinmoy Saha, Shivam Arora, Sanghamitro Das, Jawad Y. Siddiqui and Ashwin K. Iyer, ”Bandwidth control of cylindrical ring dielectric resonator antennas using metallic cap and sleeve loadings”, *IET Microwaves, Antennas and Propagation*, **11(12):1742-1747, 2017**.

4. **Latheef A. Shaik**, Chinmoy Saha, Jawad Y. Siddiqui and Y. M. M. Antar, ”Ultra-wideband monopole antenna for multiband and wideband frequency notch and narrowband applications”, *IET Microwaves, Antennas and Propagation*, **10(11):1204-1211, 2017**.

5. Chinmoy Saha, Jawad Y. Siddiqui, **Latheef A. Shaik** and Y. M. M. Antar, “Rotational Circular Split Ring Resonator Array Loaded CPW for Dual Notch and Wide Bandstop Applications”, *Microwave and Optical Technology Letters*, **57(5):1204-1209, 2014**

Presentations in Conferences

1. **Latheef A. Shaik**, Chinmoy Saha and Jawad Y. Siddiqui "Coplanar Waveguide fed Tapered Slot Antenna with Multi-Functional Characteristics" *3rd URSI - Regional Conference on Radio Science (URSR-RCRS), URSI Regional Conference on*, 1:3, 01-04 Mar. 2017. (won **the Best Paper** award)
2. **Latheef A. Shaik**, Chinmoy Saha and Jawad Y. Siddiqui "Coplanar Waveguide Fed Tapered Slot Antenna with Frequency Notched Characteristics," *15th biennial Symposium on Antennas and Propagation (APSYM2016), International symposium on Antennas and propagation proceedings*,1:2, 15-17 Dec. 2016.
3. **Latheef A. Shaik**, Shivam Arora, Chinmoy Saha and Jawad Y. Siddiqui "Bandwidth Reconfigurable Cylindrical Dielectric Ring Resonator Antenna with Metallic Loading," *IEEE Applied Electromagnetics Conference (AEMC), In proceedings*, 2015.
4. Chinmoy Saha, **Latheef A. Shaik**, and Jawad Y. Siddiqui and Y. M. M. Antar "UWB Printed Monopole Antenna with Controllable Multi Notch Function using Rotational Circular SRRs," *IEEE International Symposium on Antennas and Propagation & USNC/URSI National Radio Science Meeting, In proceedings*, 2015.
5. Chinmoy Saha, **Latheef A. Shaik**, and Jawad Y. Siddiqui and Y. M. M. Antar "An Ultra Wideband (UWB) Printed Slotted Monopole Antenna with Multi-functional Characteristics," *IEEE International Symposium on Antennas and Propagation & USNC/URSI National Radio Science Meeting, In proceedings*, 2015.